ANALYSIS AND DESIGN OF TRANSONIC CASCADES WITH SPLITTER VANES

by

H.H. Youngren

GTL Report #203 March 1991

GAS TURBINE LABORATORY
MASSACHUSETTS INSTITUTE OF TECHNOLOGY
CAMBRIDGE, MASSACHUSETTS

ANALYSIS AND DESIGN OF TRANSONIC CASCADES WITH SPLITTER VANES

by

H.H. Youngren

GTL Report #203 March 1991

This research was supported by the Air Force Office of Scientific Research, Grant AFOSR-89-0373, with Captain Henry E. Helin as Program Manager and Dr. Arthur J. Wennerstrom as Technical Monitor.

Analysis and Design of Transonic Cascades with Splitter Vanes

by

Harold Hayes Youngren

A new computational method, MISES, is developed for turbomachinery design and analysis applications. The method is based on the fully coupled viscous/inviscid method, ISES, and is applicable to blade-to-blade analysis of axial fan and compressor stator or rotors with optional splitter vanes. Quasi-three dimensional effects for stream surface radius, streamtube thickness and wheel rotation may be included. The flow is modeled with the steady Euler equations and the integral boundary layer equations. A robust Newton-Raphson method is used to solve the coupled non-linear system of equations, requiring only several minutes for solution on a typical workstation. Design options are implemented for either single surface or camber redesign.

The method is exercised by comparison with transonic cascade tests to validate the quasi-three-dimensional formulation. The results show excellent correlation to measured pressure distributions and loss levels. The multiple blade capability is demonstrated by comparison to test data for a supersonic cascade with splitter vane. New splitter vane configurations for improving the performance of the supersonic cascade are explored, resulting in large increases in turning and reduced loss.

Acknowledgements

This all started when I returned to MIT in 1987 to work on the Daedalus project *and* to get a degree or two on the side... The former effort came off pretty much on schedule, give or take a crashed airplane or so. The latter effort ended up taking somewhat longer than I had anticipated...

I would first and foremost like to thank Mark Drela, thesis supervisor and long time friend and airplane hacker, Newton whiz-extraordinaire, for all the help and fun along the way. His support on many fronts has made things easier. Also thanks to Mike Giles, co-whiz and friend, for ideas and help with his UNSFLO program.

I would also like to acknowledge the patience and persistence of Professors Witmer and Markey for helping me back into the academic world of MIT after a long hiatus at Lockheed. Thanks.

The gang at the CFDL has been a source of support, entertainment and good company. Thanks to you all, especially Sandy and Gerd my erstwhile climbing partners, Dana, Dave^2, Phil^2, Kousuke, Tom(the cartoonist), Peter, Andre, Helene, Missy, Ling and Bob Haimes. The special award for office-mate-beyond-the-call-of-duty goes to Eric Gaidos who tolerated my endless hackery on his computer terminal with an out of this world attitude...

Thanks especially to my family – Susan, Peter, Beth and my mother who have all come to think that this madness would never end. Finally, I would like to thank Cheryl, who has been patient and understanding beyond all reckoning with this compulsion to leave California (God's country) and return to Bean Town. Its time to go back.

This research was supported by the Air Force Office of Scientific Research Grant AFSOR-89-0373, with Captain Henry E. Helin as Program Manager and Dr. Arthur J. Wennerstrom as Technical Advisor.

Contents

List of Figures

List of Tables

Nomenclature

a	speed of sound
$\vec{A}_1, \vec{A}_2$	quasi-normal face area vectors
A_n	normal area
AVDR	axial velocity density ratio $\frac{\rho_2 q_2}{\rho_1 q_1}$
b	streamtube width
$\vec{B}^+, \vec{B}^-$	streamwise face area vectors
c	chord
c_{inl}	inlet characteristic variable
C_p	pressure coefficient $\frac{p-p_1}{\frac{1}{2}\rho_1 q_1^2}$
c_p, c_v	specific heats
D_{mov}, D_{rot}	global movement modes for intermediate blades
$\vec{F}$	force vector
g_l	geometric mode
h	enthalpy
H	BL shape factor
I	rothalpy
i_{off}	streamwise offset on $j = 1$ streamline for offset grid
i, j	streamwise and quasi-normal indices
$\hat{i}, \hat{j}$	unit vectors
I, J	maximum grid indices
M	Mach number
m', θ	local streamwise and circumferential coordinates
$\dot{m}$	total mass flow
$\dot{m}_j$	mass flow in streamtube j
$\tilde{n}$	geometric mode amplitude
n	streamline normal coordinate
Δn	gap between streamline and wall
$\vec{N}$	quasi-normal area vector

p	pressure, pressure on quasi-normal face
$\vec{\mathbf{q}}$	velocity vector
q	speed
r	radius
R_n	Reynolds number
$\hat{s}$	streamwise direction vector
s	boundary layer arc-length, components of streamwise vector
s_{inl}, s_{out}	inlet and outlet slopes
$\vec{S}$	streamwise area vector
T	temperature
u	speed in boundary layer
ΔV	cell volume
x	x direction, also m' coordinate
y	y direction, also circumferential coordinate
z	axial coordinate
β	flow angle
δ	change
δ^*	boundary layer displacement thickness
γ	ratio of specific heats c_p/c_v
λ, μ	first and second-order dissipation coefficients
ν	Prandtl-Meyer function
ω	non-dimensionalized loss parameter
Ω	rotational velocity
Π^+, Π^-	pressures on streamline faces
ρ	density
τ	shear
θ	BL momentum thickness
ξ	stagger angle

Superscripts:

$(\bar{})$	averaged quantity
$(\tilde{})$	dimensional quantity
$(\vec{})$	vector
$(\hat{})$	unit vector
$(\ )^{+}$	'upper' streamline
$(\ )^{-}$	'lower' streamline

Subscripts:

$(\ )_0$	stagnation quantities
$(\ )_1$	inlet quantities, conservation cell node index
$(\ )_2$	exit quantities, conservation cell node index
$(\ )_3$	mixed-out quantities, conservation cell node index
$(\ )_e$	edge (outer)
$(\ )_{\mathbf{i,o}}$	inner, outer stream surface face
$(\ )_{inl}$	inlet quantity
$(\ )_{isen}$	isentropic
$(\ )_{LE,TE}$	leading edge, trailing edge
$(\ )_{m.l.}$	mean line
$(\ )_{ref}$	reference quantity (at $r = 0$)
$(\ )_{spec}$	specified quantity
$(\ )_{x,y}$	x, y components of vector

Chapter 1
Introduction

This thesis will present a new computational method, MISES[1], which extends the fully coupled viscous/inviscid method, ISES, for application to quasi-three-dimensional cascade design. This method is intended for use as a tool for compressor cascade design and analysis and for blade-to-blade design of axial stators and rotors.

The viscous flow is modeled using the steady Euler equations and integral boundary layer equations solved with a Newton-Raphson technique, the approach used in the ISES code of Giles and Drela [1]. This has several advantages for design applications — accuracy, speed and a robust inverse design capability. Primarily, it is the speed that makes this approach attractive for design — a typical case is solved in 3-10 Newton cycles, a matter of minutes on a fast workstation. The accuracy also has a strong influence on the design process — the drag predictions from ISES are sufficiently good that they can be reliably used by a designer to optimize an airfoil at both on-design and off-design conditions, using wind tunnel testing only to *verify* the computational predictions. Although blade-to-blade design for turbomachinery is similar to the isolated airfoil design problem, there are additional difficulties in solving the viscous/inviscid governing equations, which are strongly coupled for transonic cascades. A design method for turbomachinery requires accurate loss prediction for strong shocks and for separated flows.

This work also focuses on the analysis and design of cascades with multiple blades, specifically splitter vanes. These are introduced to reduce loss and increase turning by changing the distribution of blade loading. They also increase blockage and can increase viscous losses. This thesis addresses some of the design issues for multiple

[1] To answer the inevitable question – Multiple blade Interacting Streamtube Euler Solver.

blade cascades, focusing on the optimization of the splitter vane in a highly loaded supersonic cascade.

1.1 Motivation and Background

Improved levels of performance from gas turbine engines have motivated designers to place increasing reliance on computational techniques in the design process. This is especially true as blade loadings in compressors and turbines are increased and higher levels of refinement in design are attained. Unlike typical external aerodynamic design problems, where the design is driven to virtually eliminate strong non-linear flow effects, the interacting compressible and viscous effects in cascades lead to complex flows that frequently involve significant three-dimensionality, flow separation and shock loss.

The current state of the art in computational methods for cascade analysis is three-dimensional Navier-Stokes simulations, normally using the Reynolds-averaged form of the equations with a turbulence model. These methods have the advantage of modeling all of the relevant viscous blockage effects and may be applied to analyze virtually any cascade flow. Navier-Stokes methods are presently too expensive and cumbersome to use for the bulk of the design process, typically requiring 300 to 6000 time steps to approximate steady state, involving hours of time on fast computers.

Although the flow in axial turbomachinery is three-dimensional, a useful and often necessary simplification for design purposes is to approximate the flow through a stage as a set of two-dimensional blade-to-blade problems defined on axisymmetric stream surfaces. Axisymmetric through-flow codes are used early in the preliminary design process to define circumferentially averaged conditions in one or more stages of the machine based on initial estimates of work and loss. These calculations define the flow in terms of axisymmetric stream surfaces. At the next level of design refinement the stream surface radius and spacing can be used to define a set of quasi-3D blade-to-blade design problems for each stage. These allow the designer to select or design blade profiles at several radial stations to define the complete three-dimensional rotor

or stator blade. The blade-to-blade technique works surprisingly well for most design applications, limited in effectiveness largely by the estimates for boundary layer effects on the inner and outer casing walls and by three-dimensional effects not accounted for with the axisymmetric assumptions. In the context of simpler, faster and reasonably accurate preliminary design tools, the more complex three-dimensional methods can be most effectively used as 'numerical wind tunnels' to verify the design.

1.2 Cascades with Splitter Vanes

One of the goals of this work is to develop capability for analysis and design of cascades with intermediate blades, or splitter vanes, that are added to the basic blading to increase turning or reduce flow separation and loss. The case used as a guide for this development was a high turning supersonic compressor stage with splitter vane developed and tested by the Aerospace Research Lab (ARL) in the early to mid 1970's. The high inlet Mach number and strong sidewall contraction (2:1) made this an extremely challenging test case. The blade cross-sections for the ARL two-dimensional cascade are shown in Figure 1.1. The splitter vane for this case was intended to operate in the subsonic portion of the passage downstream of the shock. The basic effect of the splitter vane on blade loading is shown in Figure 1.2, where the main blade loading is relieved by the overlapping vane.

The ARL cascade has been the subject of several previous studies, both experimental and analytical. This cascade started out as part of a high pressure-ratio, high diffusion axial rotor developed for the USAF. Tests had indicated excessive deviation angles that were reduced by the addition of a partial flow splitter. The two-dimensional cascade was tested by Holtman *et al* as a single blade [2] and later with a splitter vane [3]. A rotor using this concept was later designed and tested by Wennerstrom and Frost [4], encountering test problems from stator choking. A later experimental study [5] in 1977 examined optimization of splitter vane location.

An analytical study by Dodge [6] in 1975, using a 2D inviscid potential method,

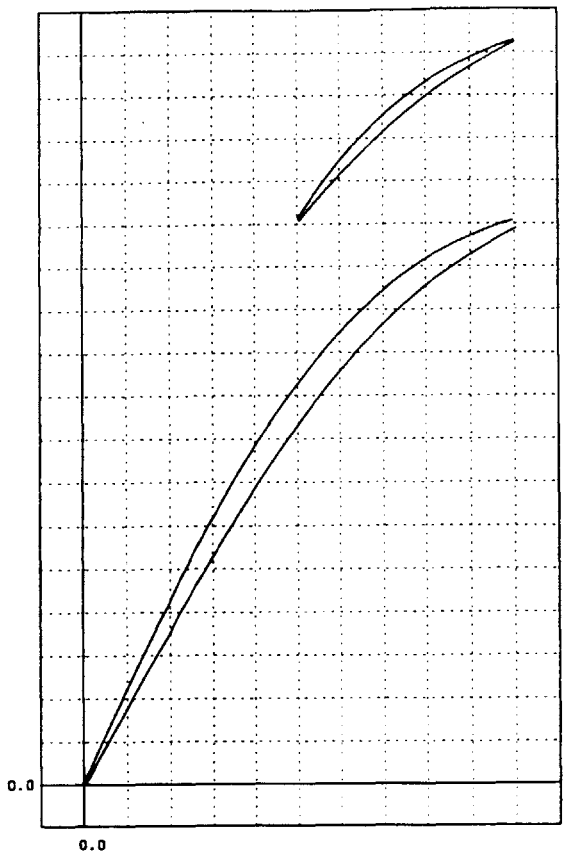

Figure 1.1: Blade sections for ARL cascade with splitter vane.

examined the ARL cascade with and without the splitter vane, attempting to do a design study with limited success. A second effort [7] in 1978, again by Dodge, brought a much more capable inviscid 3D potential method to bear on the ARL cascade and rotor, although the lack of viscous blockage effects made comparisons to test data somewhat inconclusive.

The large loss levels and deviation angles from the experiment indicate that the ARL cascade has extensive separated flow, which is likely the source of problems in earlier analytical work. The current method, with its full inviscid/viscous coupling scheme, is capable of modeling these blockage effects and should give a more complete picture of the splitter vane interaction with the main blade.

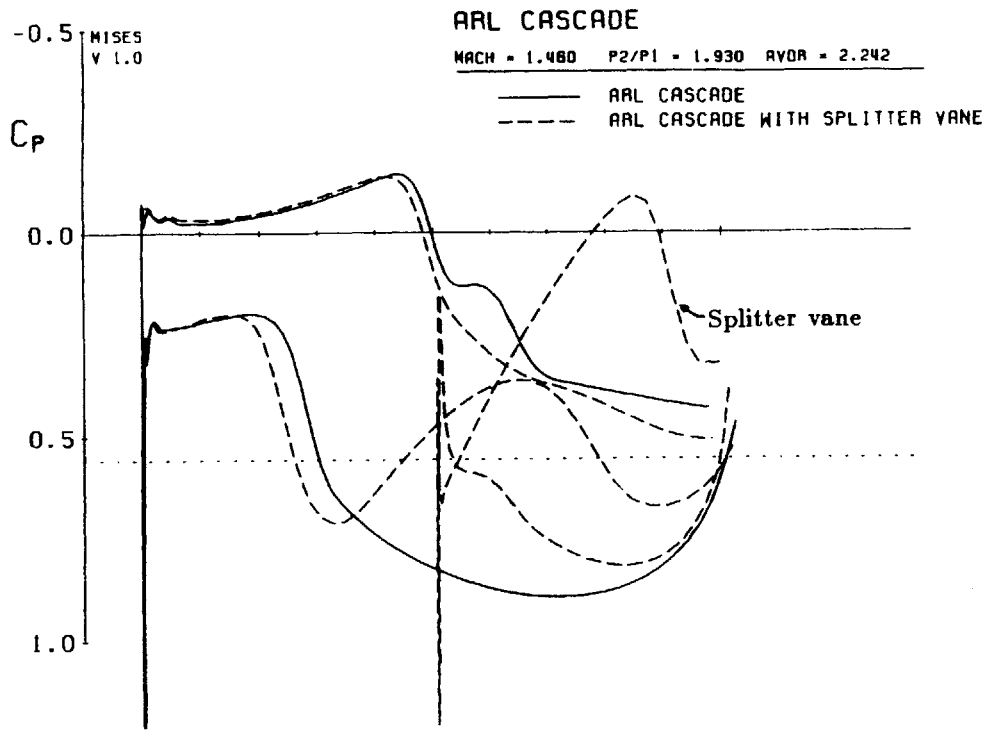

Figure 1.2: Effect of splitter vane on pressure distributions for ARL cascade.

1.3 Overview of Thesis

The thesis is structured so the introductory material briefly discusses the development of the method, while the bulky derivations and detailed material is presented in the appendices. A brief sketch of the contents of the thesis is given below:

Chapter 2 introduces the coordinate systems, governing equations and boundary conditions appropriate to the quasi-3D blade to blade problem.

Chapter 3 presents the discrete form for the equations and boundary conditions on the intrinsic streamline grid. The Newton-Raphson method used to solve the non-linear system is discussed. Design options and the modifications for multiple blade analysis and design are introduced. The offset-periodic grid and solver used for supersonic cascades is discussed.

Chapter 4 exercises the method on several analysis test cases at subsonic, transonic and supersonic inlet Mach numbers to validate the quasi-3D capabilities. Solutions for the supersonic ARL cascade with splitter vane are compared to test data.

Chapter 5 examines the ARL cascade with splitter vane in greater detail. The effects the splitter vane position are analyzed and compared to test data. The splitter and main blade are redesigned to optimize loss and turning. Additional avenues for cascade modification are explored using the method.

Appendix A presents the derivation of the discrete form of the quasi-3D Euler equations on the streamline grid.

Appendix B outlines the modifications to the integral boundary layer method to include quasi-3D effects.

Appendix C presents the loss model and the loss sensitivity calculation used in design optimization.

Appendix D contains the details of the Jacobian matrices and matrix solution.

Chapter 2

Theory

2.1 Cascade Coordinate Systems

The geometric quantities defining a two-dimensional cascade are illustrated in Figure 2.1. The cascade blades are periodic in y with pitch y_{pitch}. The blade chordlines

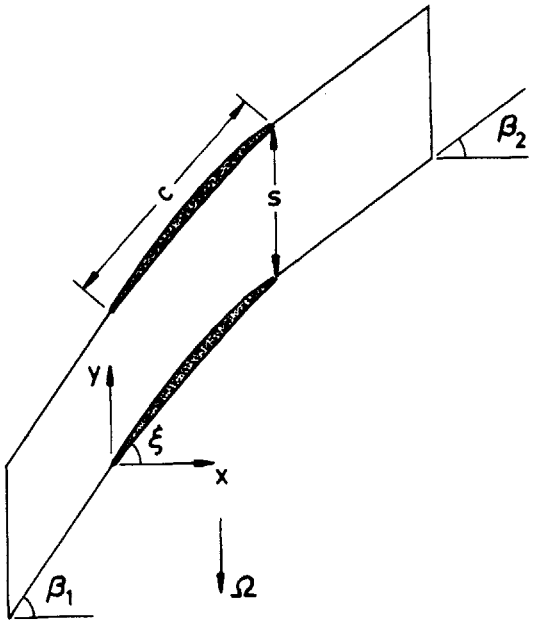

Figure 2.1: Cascade coordinate system

are inclined to x direction by the stagger angle ξ. The inlet flow direction is β_1 and the outlet flow angle is β_2.

The three-dimensional flow in an axial stator or rotor is treated as an axisymmetric meridional flow and a quasi-3D blade-to-blade flow defined on the axisymmetric stream surfaces, as shown in Figure 2.2. In this figure blade elements for the blade-to-blade flow

are shown defined by a stream surface of revolution. The axisymmetric stream surfaces are defined in terms of the radius $r(z)$ and streamtube thickness $b(z)$, where z is the axial coordinate, and are shown as streamlines in the meridional plane in Figure 2.3.

Meridional streamlines can be determined using a through-flow method to solve the

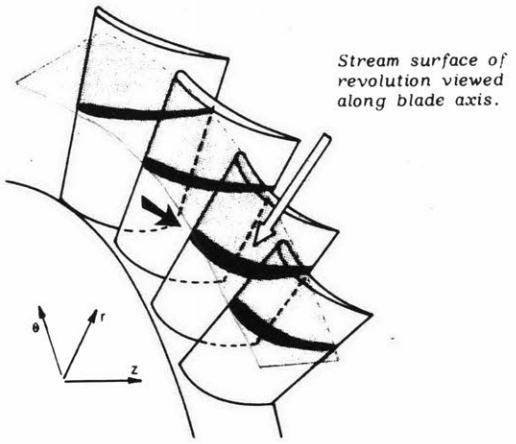

Figure 2.2: Blade-to-blade flow on a stream surface of revolution

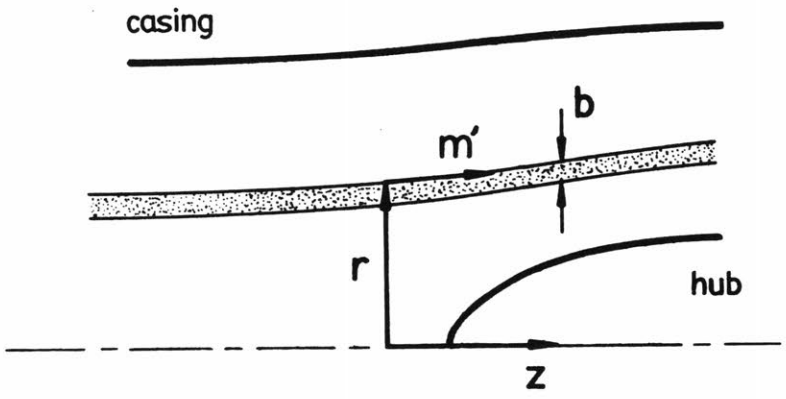

Figure 2.3: Meridional (r-z) plane for defining stream surfaces

axial and radial equilibrium relations for mass, momentum and energy given the basic stage inflow and outflow parameters and the hub and tip casing shapes. The flow over a complete blade can be approximated by a set of quasi-3D blade-to-blade problems for stream surfaces at several radial stations, a technique that forms the basis of many preliminary design systems for compressor design.

The cascade definitions in Figure 2.1 are also used for axial stator blades with x and y corresponding to the axial coordinate z and circumferential coordinate θ. Alternatively, x and y will correspond to a local m', θ coordinate system defined on the stream surface. This choice is advantageous because it is a conformal mapping of the surface of revolution to a plane, preserving angles and shapes. The new coordinate m' is defined as the normalized arc-length in the $r - z$ plane.

$$m' = \int \frac{dm}{r} = \int \frac{\sqrt{(dr)^2 + (dz)^2}}{r} \tag{2.1}$$

In the current method the quasi-3D blade-to-blade flow is solved on a stream surface in an m', θ coordinate system with specified radius and stream tube thickness.

These definitions also apply for a rotor, except that the flow problem is defined in a blade-relative coordinate system rotating with respect to an inertial frame. Referring to Figure 2.1, the blades on an axial rotor are defined to rotate with angular velocity Ω in the $-y$ direction.

2.2 Viscous/Inviscid Flow Solution

Unlike most airfoil flows, cascade flows normally exhibit strong coupling between the inviscid flow and the viscous boundary layers, particularly at transonic and supersonic Mach numbers. This coupling can be sufficiently strong, involving extensive flow separation, that the flow cannot be solved without considering viscous effects on blockage, e.g. the ARL cascade in Chapter 4. Viscous effects must also be included for the prediction of cascade losses.

Instead of solving the viscous flow directly, the zonal approach of ISES is used. An equivalent inviscid flow, EIF [8], is postulated using a displacement surface to represent the viscous layer, as illustrated in Figure 2.4. The inner boundary of the EIF is displaced outward from the wall by the boundary layer displacement thickness δ^*. The outer inviscid flow is solved using the steady state Euler equations while the boundary layer flow is solved using an integral boundary layer method. The outer flow is coupled

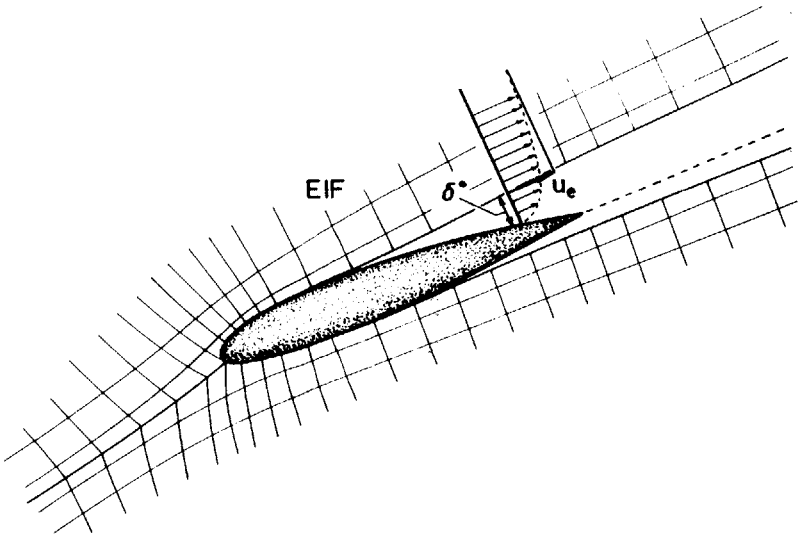

Figure 2.4: Equivalent inviscid flow defined by BL displacement thickness

to the boundary layer through the edge velocity and density that drive the integral boundary layer solution for the displacement thickness. These two interdependent flow domains are fully coupled by a simultaneous Newton-Raphson solution procedure for the non-linear equations.

2.3 Steady-State Euler Equations

The inviscid flow is solved using the steady-state Euler equations in a blade-relative coordinate system. The integral form for the Euler equations is derived using the conservation laws for mass, momentum and energy applied to a control volume V with boundary ∂V and unit normal $\hat{\mathbf{n}}$.

$$\textbf{Mass} \qquad \oint_{\partial V} \rho(\vec{\mathbf{q}} \cdot \hat{\mathbf{n}})\, dA \;=\; 0 \tag{2.2}$$

$$\textbf{Momentum} \qquad \oint_{\partial V} \rho(\vec{\mathbf{q}} \cdot \hat{\mathbf{n}})\vec{\mathbf{q}} + p\hat{\mathbf{n}}\, dA \;=\; -\oint_{V} \rho\vec{\mathbf{f}}\, dV \tag{2.3}$$

$$\textbf{Energy} \qquad \oint_{\partial V} \rho(\vec{\mathbf{q}} \cdot \hat{\mathbf{n}})\, \mathbf{I}\, dA \;=\; 0 \tag{2.4}$$

These equations apply to a reference frame rotating with angular velocity $\vec{\Omega}$ with respect to the inertial frame, adding rotational terms to the momentum and energy equations.

The source term in the momentum equation, $\vec{\mathbf{f}}$ represents the Coriolis and centrifugal force terms in the blade relative system.

$$\vec{\mathbf{f}} = \vec{\Omega} \times \left(\vec{\Omega} \times \vec{r}\right) + 2\vec{\Omega} \times \vec{\mathbf{q}} \tag{2.5}$$

The conserved quantity in energy equation is the *rothalpy*, **I**, which is invariant in the rotating system.

$$\mathbf{I} = h + \frac{q^2}{2} - \frac{(\Omega r)^2}{2} \tag{2.6}$$

The inviscid formulation is completed with the assumption of the ideal gas law.

$$h = \frac{\gamma}{\gamma - 1}\frac{p}{\rho} \qquad \text{with } \gamma = c_p/c_v \tag{2.7}$$

The strategy for solving the inviscid equations is to discretize them on a streamline grid, eliminating convection terms across the streamline faces. This leads to a particularly simple form for the Euler equations, where the continuity and energy equations are replaced by statements of constant mass flow and rothalpy in each streamtube, leaving only the equations for streamwise and normal momentum to be solved.

2.4 Boundary Layer Solution

The viscous flow is solved using the integral boundary layer method from ISES [9], modified to include quasi-3D effects, see Appendix B. This is a two-equation method employing the venerable von Kármán integral momentum equation and the kinetic energy shape parameter equation. In turbulent flow regions a dissipation lag equation, similar to Green's lag equation [10], is added to model upstream history effects on the Reynolds stress. These equations have the form

$$\frac{d\theta}{ds} = \mathcal{F}_1(\theta, \delta^*, u_e) \tag{2.8}$$

$$\frac{d\left[H^*(\theta, \delta^*, u_e)\right]}{ds} = \mathcal{F}_2(\theta, \delta^*, u_e, C_\tau) \tag{2.9}$$

$$\frac{dC_\tau}{ds} = \mathcal{F}_3(\theta, \delta^*, u_e, C_\tau) \tag{2.10}$$

Relations derived using Swafford's turbulent flow profiles provide turbulent closure for the shape factors, skin friction and dissipation.

In laminar flow regions the same basic scheme is used, with the dissipation lag equation (2.10) replaced by a transition equation. An envelope method for maximum disturbance amplification is used, based on spatial amplification of Tollmein-Schlichting waves in the Orr-Sommerfeld equation. The maximum disturbance amplitude variable $\tilde{N}$ replaces C_τ in the BL equation set. The amplification equation has the form

$$\frac{d\tilde{N}}{ds} = \mathcal{F}_4(\theta, \delta^*, u_e) \tag{2.11}$$

The transition point is determined by the variable $\tilde{N}$ exceeding a specified critical value $\tilde{N}_{crit}$. The result is roughly equivalent to the classical e^9 transition prediction method. The laminar flow equations are completed using closure relations derived from correlations with Falkner-Skan profiles.

The boundary layer solution is influenced by the edge velocity u_e, which is also the surface velocity in the EIF. Correspondingly, the displacement thickness from the boundary layer influences the inviscid flow by offsetting the edge of the inviscid region from the surface. Because the inviscid and viscous solutions are fully coupled in the Newton system, flows involving separation may be calculated.

2.5 Boundary Conditions

The principal requirement for the boundary conditions is that they must completely specify the flow problem and be physically realizable. This is a more serious problem for cascades than for airfoils due to the finite domain and transonic or supersonic conditions into or within the passage, presenting far more opportunities to specify ill-posed boundary conditions.

The boundary conditions must specify the inflow thermodynamic quantities — stagnation density and stagnation enthalpy. Inflow direction must also be specified, although

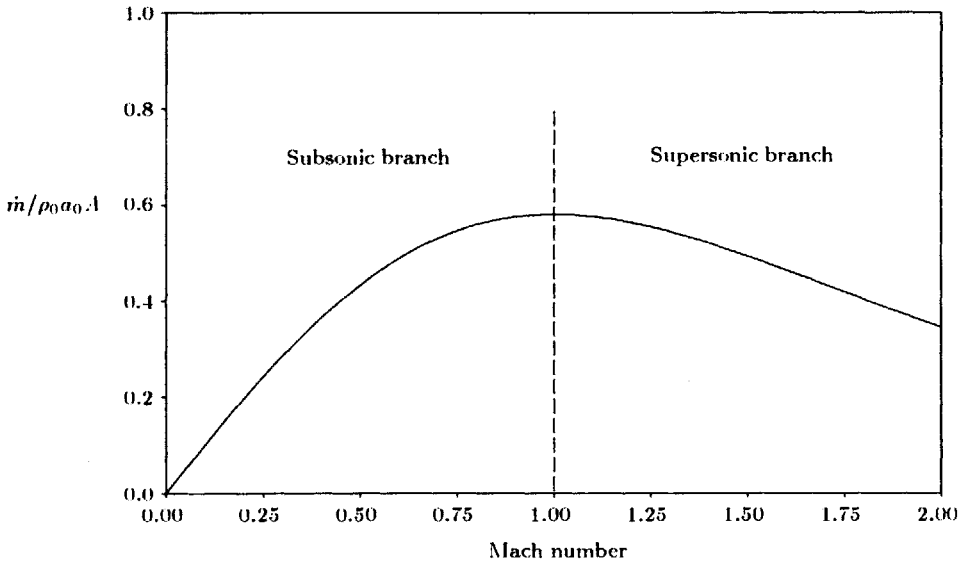

Figure 2.5: Variation of mass flow with Mach number

the form this takes depends on the Mach number. One additional quantity must be specified, either the mass flow or the exit pressure. Additional boundary conditions that constrain added variables (or DOF's) are required on a one-to-one basis. These are often used to drive the system to a specified flow condition or for design applications.

Some combinations of boundary conditions are ill-posed - consider the mass flow in a passage of area A, shown as a function of Mach number in Figure 2.5. Up to the point at which the passage chokes, the specification of mass flow is well-posed. Beyond the choke point, further increases of mass flow are ill-posed. In fact, the discrete equations with specified mass flow become increasingly ill-conditioned as the choking point is approached, leading to numerical problems. These can be alleviated by specifying exit pressure and allowing the mass flow be determined by the solution, which is well-posed because mass flow is uniquely specified by exit pressure, while the reverse is not true.

The Newton method used to solve the non-linear equations requires an initial flow condition from which to begin iterating to a solution. For a given mass flow in Figure 2.5 there exists two possible Mach numbers, one subsonic and one supersonic. It is essential

that the initial state correspond to the desired branch.

2.5.1 Subsonic BC's

For subsonic inflow the boundary conditions that must be specified depend on whether the flow in the passage is choked. These take the form

Subsonic BC

inflow BC	outflow BC	determined
$\rho_0, h_0, \dot{m}, \beta_1$		p_{exit}
or		
ρ_0, h_0, β_1	p_{exit}	$\dot{m}$

Either of these combinations may be used for unchoked flow. Exit pressure need not be specified since p_{exit} is uniquely determined for unchoked flow by the inlet conditions and cascade geometry. Alternatively, p_{exit} can be specified, provided one of the inflow boundary conditions is dropped to avoid over-specifying the problem. The inlet flow angle β_1 must be specified, although it should be imposed sufficiently far forward of the cascade that this specification is relatively unaffected by its flow disturbance. The inlet mass flow specifies the inlet Mach number, given the other inlet quantities.

As the flow becomes choked there is no longer a unique exit pressure for a given set of inflow conditions. The second boundary condition must be used, with p_{exit} specified and one of the inflow boundary conditions dropped, usually mass flow since it is always uniquely determined by exit pressure.

2.5.2 Supersonic BC's

As a result of the high stagger angles used on supersonic cascades the inflow is normally also axially subsonic, i.e. $M_1 \cos\beta_1 < 1.0$. The incoming flow is influenced by the fixed pattern of expansion and/or compression waves that run axially forward from the supersonic upper surface of the blade, see Figure 2.6. These waves turn the incoming

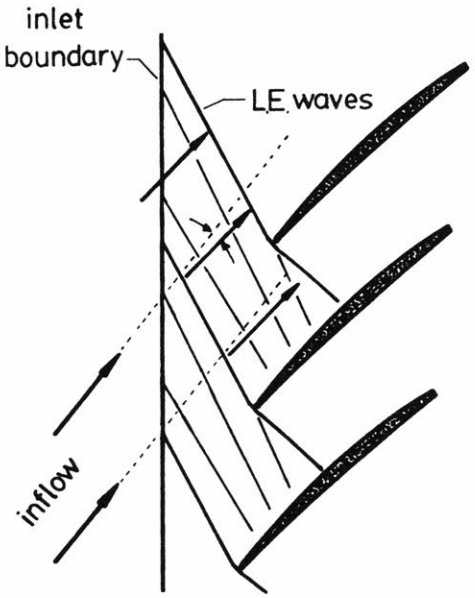

Figure 2.6: Supersonic/axially-subsonic inflow for cascade, showing inlet wave system

flow to approximately align with the supersonic portion of the blade upper surface. At the point where the cascade is choked the upstream flow into the infinite cascade is at the so-called "unique incidence" condition for the cascade. In practice, whenever the inflow is supersonic the range of inlet flow angles into the cascade is quite close to the unique incidence point.

Supersonic, axially subsonic BC

inflow BC	outflow BC	determined
ρ_0, h_0, c_{inl}	p_{exit}	$\dot{m}$

The inflow angle cannot be arbitrarily specified for supersonic flow due to the influence of the cascade wave system. The correct inlet condition for supersonic/axially-subsonic inflow is to specify an inlet characteristic condition so that the inlet boundary acts as a *free boundary* to expansion or compression waves in the flow domain, see [11, page 291]. This inflow condition is defined by

$$c_{inl} = \theta \pm \nu(M) = c_{inl_{spec}} \tag{2.12}$$

where θ is the local inlet flow angle and $\nu(M)$ is the Prandtl-Meyer function,

$$\nu = \frac{\gamma-1}{\gamma+1}\arctan\sqrt{(M^2-1)\frac{\gamma-1}{\gamma+1}} - \arctan\sqrt{M^2-1} \tag{2.13}$$

With inlet characteristic conditions the inflow angle and Mach number are no longer independent. As the inflow angle is changed by expansion or compression waves from the cascade, the local Mach number changes along the inlet characteristic. The Mach and local flow angle dependence for a family of characteristics is shown in Figure 2.7. Since the slope $d\theta/dM$ vanishes at the sonic point, the Mach number becomes very sensitive to flow angle changes near $M = 1.0$.

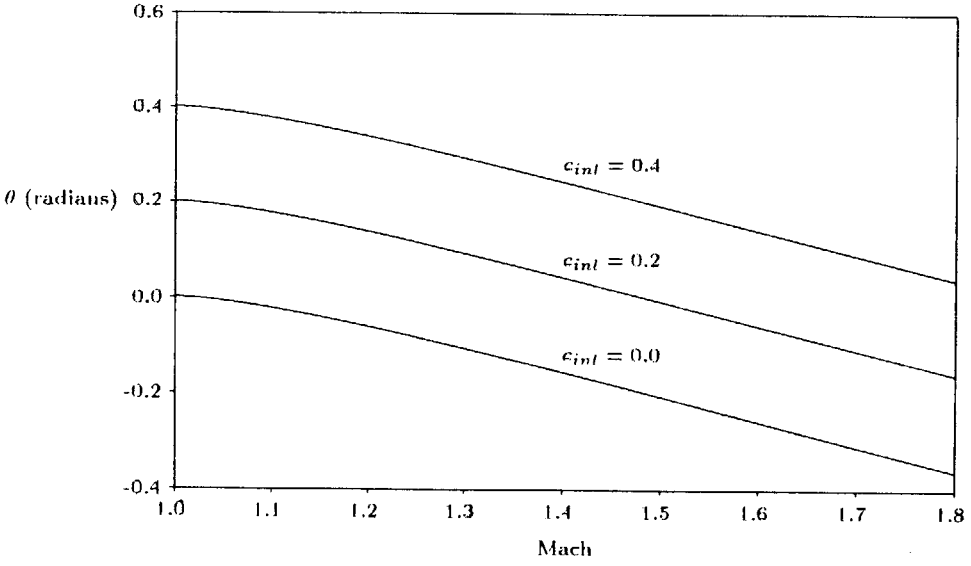

Figure 2.7: Characteristic families for local angle θ and Mach

2.5.3 Periodic BC

Periodic conditions for geometric continuity must be imposed on the stagnation streamlines upstream and downstream of the blade. In addition the streamlines must be force-free, set by imposing equal pressures across the periodic boundary.

2.5.4 Solid Wall BC

Since a streamline-based solution technique is used for the inviscid flow, solid wall conditions are easily imposed since no mass flow crosses the blade surface streamline, by definition. The solid wall boundary condition fixes the streamline position to the blade surface, i.e. $\delta n = 0$, where n is the coordinate normal to the surface streamline. For viscous cases, where the EIF is displaced by the boundary layer, this becomes $\delta n = \delta(\delta^*)$, where δ^* is the displacement thickness from the BL solution.

2.5.5 Design BC

One of the useful options for design applications is a form of inverse boundary condition where, instead of specifying the surface position and having the pressure set by the flow field, the surface pressure is specified directly and the streamline geometry is determined by the flow solution. This is easily done within the framework of the streamline solver by imposing a wall pressure condition in place of the solid wall condition. An arbitrary specified pressure distribution may not give a physically realizable blade, so specified pressure distributions are subject to several compatibility conditions, as discussed in [9].

Inverse design boundary conditions cannot be applied over a separated region because there exists only a very weak local constraint for surface displacement in the separated BL. A modal design scheme has been implemented, using a set of geometric shape functions (or bump functions), to circumvent this limitation. Modal design is discussed in greater detail in Chapter 3. Camber changes to achieve a specified pressure loading for fixed thickness may also be determined using a variant of the periodic boundary condition.

2.6 Loss Calculation

Losses through a cascade result from the entropy rise from inlet to outlet produced by inviscid shock losses and viscous dissipation in the blade boundary layers. The increase in entropy causes a reduction of the stagnation pressure from the equivalent isentropic value. The loss coefficient ω is defined as the reduction in exit stagnation pressure non-dimensionalized by the inlet dynamic pressure.

$$\omega = \frac{p_{0_{isen}} - \bar{p}_{0_2}}{p_{0_1} - p_1} \tag{2.14}$$

where $\bar{p}_{0_2}$ is the mass-averaged exit stagnation pressure and $p_{0_{isen}}$ is the isentropic (i.e. lossless) stagnation pressure at the exit. Two approaches are used for calculating loss — a mass-averaged stagnation pressure defect at the exit plane, and an extrapolation to a fully mixed condition. Further details on the loss calculation are presented in Appendix C.

2.7 Non-Dimensionalization and Reference Quantities

Although the basic equations can be used with quantities having any consistent set of units, it is advantageous to impose a systematic non-dimensionalization of the quantities defining the geometry and flow. The physical quantities, such as $\tilde{x}$, etc., are non-dimensionalized using reference quantities $\tilde{c}$, $\tilde{\rho}_0$ and $\tilde{a}_0$.

$$\begin{aligned} x &= \frac{\tilde{x}}{\tilde{c}_{axial}} & y &= \frac{\tilde{y}}{\tilde{c}_{axial}} \\ \rho &= \frac{\tilde{\rho}}{\tilde{\rho}_0} & q &= \frac{\tilde{q}}{\tilde{a}_0} \end{aligned} \tag{2.15}$$

This means that, in the non-dimensional variables, inlet reference values for flow variables are defined at $r = 0$ as

$$\begin{aligned} \rho_{0_{ref}} &= 1 & p_{0_{ref}} &= \frac{1}{\gamma} \\ a_{0_{ref}} &= 1 & I &= \frac{1}{\gamma - 1} \end{aligned} \tag{2.16}$$

Chapter 3
Numerical Formulation

This chapter describes the numerical implementation of the Newton system and boundary conditions for the streamtube-based Euler solution with integral boundary layers. A design capability for viscous cascade redesign using a set of geometric perturbation modes is introduced. The basic scheme is generalized to treat multiple blade cascades and several new modes for the design of splitter vanes are introduced. Problems with regular topology grids for supersonic cascades are discussed along with the formulation for the new offset-periodic grid topology. Additional details on the derivation and implementation are presented in the Appendices.

3.1 Overview of Numerical Scheme

The viscous cascade flow is solved using a zonal approach, dividing the flow into an inviscid outer flow modeled using the steady-state Euler equations, and viscous layers over blades and in wakes modeled with an integral boundary layer method. The two zones are interacted by driving the boundary layer with the edge flow quantities from the inviscid flow, whose edge is defined by the boundary layer displacement thickness. The non-linear equations for the two zones are solved simultaneously using a Newton-Raphson solver making it possible to treat fully separated flows. The Newton solver uses a direct solution of the linearized system, making the method robust, and allowing additional well-conditioned degrees-of-freedom (DOF's) and constraint equations to be freely added to apply useful boundary conditions or design functions.

3.1.1 Inviscid Flow

The inviscid flow is solved with a conservative formulation of the steady-state Euler equations in the blade-relative coordinate system. The equations for mass, momentum and energy are solved on an $I \times J$ streamline grid of nodes that define the problem domain, see Figure 3.1. The grid is defined by families of streamlines and quasi-normal lines indexed by j by i, respectively.

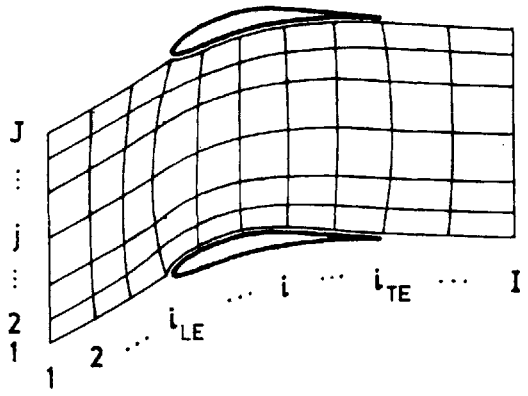

Figure 3.1: Streamline grid system for discrete Euler equations.

The discrete form of the equations is derived by applying the integral equations 2.2 through 2.4 to the basic conservation cell at i, j, defined on a streamtube between three quasi-normal lines, as shown in Figure 3.2. The use of the streamline grid considerably

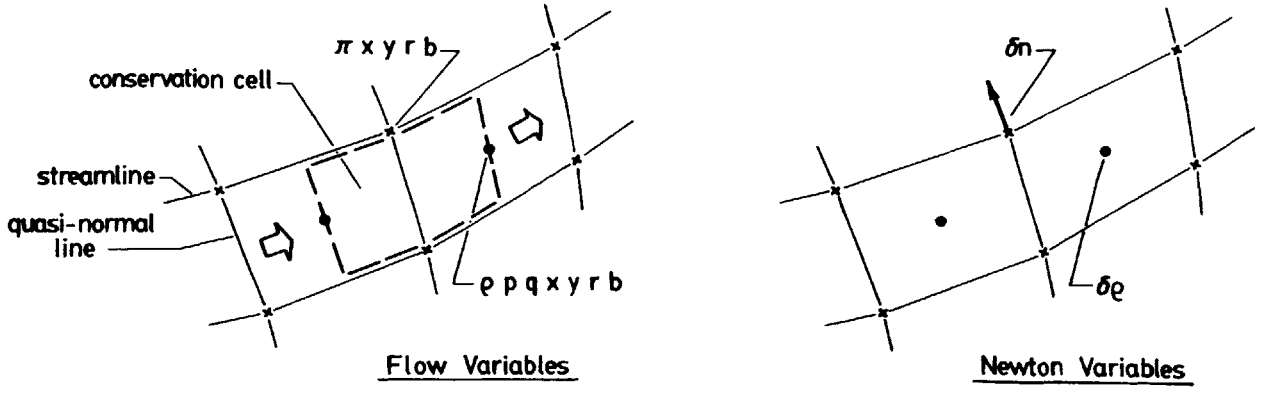

Figure 3.2: Conservation cell and variable locations.

simplifies the discrete form of the equations because it eliminates convection terms across the streamline grid faces. The velocity and density need only be defined on the two quasi-normal faces of the cell. Pressures are defined on quasi-normal faces as p, and on streamwise faces as $\Pi^{\pm}$. The mass equation reduces to an implicit statement of constant mass flow in each streamtube.

$$\dot{m}_1 = \dot{m}_2 = \cdots = \dot{m}_i$$

Similarly the energy equation becomes an statement of constant rothalpy

$$\mathbf{I}_1 = \mathbf{I}_2 = \cdots = \mathbf{I}_i$$

The two equations remaining explicitly are the components of momentum. The momentum forces are resolved into a streamwise, or S-momentum, equation and a quasi-normal, or N-momentum, equation.

$$\vec{S} \cdot \sum \vec{F}_{i,j} = \mathcal{F}_{S_{i,j}}(\rho, p, q, x, y, r, b) = 0 \tag{3.1}$$

$$\vec{N} \cdot \sum \vec{F}_{i,j} = \mathcal{F}_{N_{i,j}}(\rho, p, q, \Pi^-, \Pi^+, x, y, r, b) = 0 \tag{3.2}$$

where the forces consist of pressure, mass flux and rotational forces. Rather than use the N-momentum equation directly, the $\Pi^{\pm}$ streamline pressure variables are eliminated by differencing the N-momentum equations on adjacent streamtubes. The resulting equation, the reduced N-momentum equation, gives the net force across the streamline directly.

$$\mathcal{F}_{\tilde{N}_{i,j}}(\rho, p, q, x, y, r, b)_j^{j+1} = 0 \tag{3.3}$$

where the dependence is now on the variables in two streamtubes j and $j+1$. Note that the solution of the Euler equations must result in the balancing of the streamwise forces in each streamtube and the normal forces across each streamline.

One of the advantages of this formulation is that the streamline equations require no added dissipation for subsonic flow. Dissipation is added in supersonic regions in the form of an upwinded velocity term, similar to a bulk viscosity. This term becomes significant in strong velocity gradients and stabilizes the scheme for capturing shocks. The first-order dissipation scheme from reference [9] is normally used, although a second-order dissipation scheme has been added that reduces spurious dissipation loss. Stability

problems at supersonic Mach numbers have limited the use of the second-order scheme to subsonic and transonic flows.

Corresponding to the two momentum equations for each conservation cell there must be two unknowns. These have been chosen as the changes in density $\delta\rho$ on each quasi-normal cell face, and the normal displacement δn of each streamline node, as shown in Figure 3.2. The grid node positions are therefore determined as part of the solution, making it simple to extend the basic method to design problems where the streamline shape corresponding to a specified pressure distribution is determined. The discrete form for the interior equations is fully derived in Appendix A.

3.1.2 Boundary Conditions

The system of interior equations must be closed by applying boundary conditions at the edges of the domain, see Figure 3.3 These take the form of periodic and solid wall

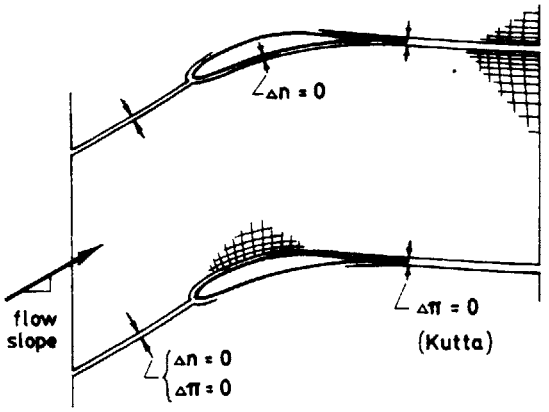

Figure 3.3: Boundary conditions on domain boundaries.

boundary conditions on the $j = 1$ and $j = J$ faces of the domain and inlet and exit slope conditions on the $i = 1$ and $i = I$ faces. Although they are not unknowns in the equations, quantities for rothalpy and mass flow are also implicitly or explicitly set at $i = 1$. Each streamtube also has a specified stagnation density condition set at the inlet. For choked flow the static pressure is imposed at the exit.

The discrete form for the edge boundary conditions is summarized in Table 3.1. Periodic conditions are applied across stagnation streamlines upstream and downstream of the blade, specifying Δn_i, the gap between streamlines $j = 1$ and $j = J$, accounting for the pitch offset. Solid wall conditions are applied on each of the stagnation streamlines between the blade leading and trailing edge by imposing Δn, the gap between streamline and the wall. These definitions for Δn are modified for viscous flows to account for blade and wake boundary layer displacement thickness.

Table 3.1: Discrete boundary conditions on domain edges.

Boundary type	Discrete boundary condition
solid surface	$\Delta n_{i,1} = 0$ $\Delta n_{i,J} = 0$
periodic	$\Delta n_i = 0$ $\Pi^-_{i,1} - \Pi^+_{i,J} = 0$
subsonic inflow	$\frac{y_{2,j} - y_{1,j}}{x_{2,j} - x_{1,j}} = s_{inl}$ $\rho_{0_{1,j}} - \rho_{0_{ref}} = 0$
supersonic inflow	$\arctan\left(\frac{y_{2,j}-y_{1,j}}{x_{2,j}-x_{1,j}}\right) \pm \nu(M_{1,j}) = c_{inl}$ $\rho_{0_{1,j}} - \rho_{0_{ref}} = 0$
outflow	$\frac{y_{I,j} - y_{I-1,j}}{x_{I,j} - x_{I-1,j}} = s_{out}$

The inlet flow direction is imposed by requiring that all streamline segments at $i = 1$ have a specified slope $s_{inl} = \tan\beta_1$. For supersonic inlet conditions the inlet slope condition is replaced by an inlet characteristic condition specifying the local angle for streamlines $1 \leq j \leq J - 1$. The angle for the remaining $j = J$ streamline is set by geometric periodicity.

The outlet flow direction is treated analogously to the inlet direction, and is imposed by requiring that all segments at $i = I$ have slope $s_{out} = \tan\beta_2$. In practice, to avoid a large pressure jump at the blade trailing edge, the exit angle should be treated as an additional unknown which is set by the trailing edge Kutta condition.

The inlet stagnation density condition is imposed using

$$\rho_{1,j}\left(\frac{h_0}{\mathbf{I}}\right)^{-\frac{1}{\gamma-1}} - \rho_{0_{ref}} = 0 \qquad \text{where } h_0 = \mathbf{I} - \frac{q_{1,j}^2}{2} + \frac{(\Omega r)^2}{2} \tag{3.4}$$

The streamtube approach encourages several of the boundary conditions to be applied implicitly, written directly into the momentum equations. The rothalpy is constant in the domain and is not treated as an unknown. The mass flow is also constant for each streamtube and is treated implicitly. Mass flow is set by inflow Mach number and streamtube area at the inlet. The implicit treatment of mass flow requires special treatment for choked flow, where the mass flow is effectively determined by an imposed exit pressure. The details of the choked flow solution are discussed in Appendix D.

3.1.3 Newton-Raphson Solution

The complete set of flow equations and boundary conditions specify a large non-linear system which is solved using a full Newton-Raphson method. An initial streamline grid, roughly corresponding to an incompressible flow solution, is generated about the blades using an elliptic grid generator and supplies the initial guess for the Newton iteration. The flow field is initialized with a uniform density for subsonic flow, or a smooth gradient of density to a specified exit condition at supersonic or choked conditions.

The basic Newton method solves the general non-linear system

$$\mathbf{R}(\mathbf{Q}) = 0 \tag{3.5}$$

where $\mathbf{Q}$ is the vector of variables and $\mathbf{R}$ is the vector of equations. At iteration level m, the Newton solution procedure is

$$\left[\frac{\partial \mathbf{R}}{\partial \mathbf{Q}}\right]^m \delta\mathbf{Q}^m = -\mathbf{R}^m \tag{3.6}$$

$$\mathbf{Q}^{m+1} = \mathbf{Q}^m + \delta\mathbf{Q}^m \tag{3.7}$$

Care must be taken with the last step when updating the variables to limit changes to ensure that the variables remain within reasonable limits. The Newton changes are clamped so that density and velocity may only change by 30% per iteration.

For the inviscid flow $\mathbf{R}$ consists of the S-momentum equations on each streamtube and the N-momentum equations on each streamline plus the boundary conditions at the domain edges. The vector of unknowns $\mathbf{Q}$ is made up of unknowns for the interior equations consisting of perturbations to the streamtube cell density $\delta\rho$ defined on quasi-normal faces and perturbations to the streamline normal node displacement δn. A few additional global unknowns are normally introduced to control boundary conditions such as inlet or exit angle. One additional global constraint equation must be added to the system for each global unknown.

The Jacobian matrix $\left[\frac{\partial\mathbf{R}}{\partial\mathbf{Q}}\right]^m$ must be generated and inverted for each Newton step. This system represents the linearized change in the residual with respect to the unknowns and is constructed by taking variations of the equations with respect to each of flow and geometric variables. These variations are resolved by repeated application of the chain rule for partial derivatives to be minimally expressed only in terms of the Newton system unknowns $\delta\rho$ and δn. For example, taking the S-momentum equation 3.1 at i, j

$$\delta\mathcal{F}_{S_{i,j}} = \frac{\partial\mathcal{F}_S}{\partial\rho}\delta\rho + \frac{\partial\mathcal{F}_S}{\partial p}\delta p + \frac{\partial\mathcal{F}_S}{\partial q}\delta q + \frac{\partial\mathcal{F}_S}{\partial x}\delta x + \frac{\partial\mathcal{F}_S}{\partial y}\delta y + \frac{\partial\mathcal{F}_S}{\partial r}\delta r + \frac{\partial\mathcal{F}_S}{\partial b}\delta b$$

The variations δp, δq, etc. are resolved in terms of *their* dependencies on $\delta\rho$ and δn using repeated applications of the chain rule, as an example the pressure variation $p(\rho, q, x, y, r, b)$ is resolved using

$$\delta p = \left(\frac{\partial p}{\partial\rho} + \frac{\partial p}{\partial q}\frac{\partial q}{\partial\rho}\right)\delta\rho + \left(\frac{\partial p}{\partial r}\frac{\partial r}{\partial x}\frac{\partial x}{\partial n} + \frac{\partial p}{\partial q}\left(\frac{\partial q}{\partial x}\frac{\partial x}{\partial n} + \frac{\partial q}{\partial y}\frac{\partial y}{\partial n} + \frac{\partial q}{\partial r}\frac{\partial r}{\partial x}\frac{\partial x}{\partial n}\right)\right)\delta n + \cdots$$

where the intermediate derivatives such as $\frac{\partial p}{\partial q}$ are generated and stored at each iteration level. Although it looks awkward on paper, the chain rule process is reasonably efficient at the Fortran level, at least.

3.1.4 Matrix System

The Jacobian matrix is a large linear system of $I \times (2J-1)$ equations, made up of $(I-2) \times (J-1)$ S-momentum equations and $(I-2) \times (J-2)$ reduced N-momentum equations. Boundary conditions supply equations on the $j = 1$ and $j = J$ streamlines and the $i = 1$ and $i = I$ quasi-normal lines.

The domain of dependence for the S and N-momentum equations is relatively compact, as shown in Figure 3.4. The basic equations span three streamwise nodes, corre-

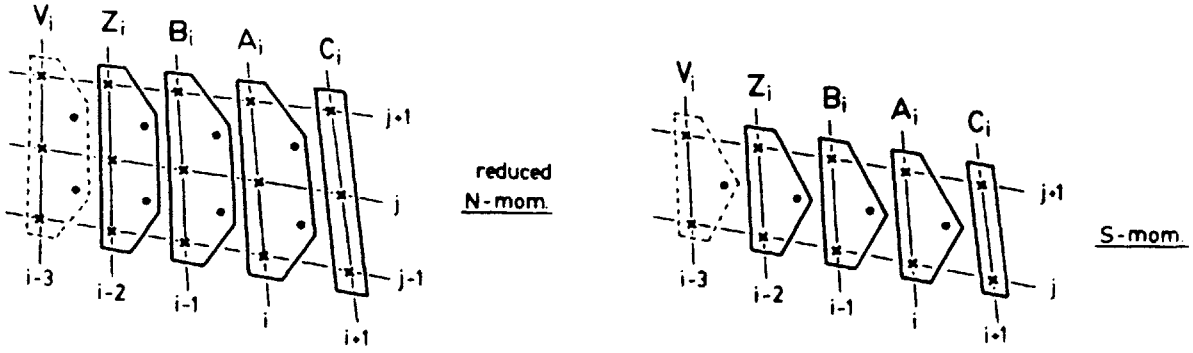

Figure 3.4: Domain of dependence for S-momentum and N-momentum equations.

sponding to blocks B_i, A_i and C_i. The S-momentum equation spans one streamtube (two streamlines) and the N-momentum equation spans two streamtubes (three streamlines). Additional upstream dependence, due to artificial dissipation, increases the domain of dependence to include one or two additional streamwise nodes. The small 'molecule' of dependence results in a sparse Jacobian matrix whose equations are most efficiently

arranged as I block rows of (2J-1) equations in each block and have the form

$$
\begin{bmatrix}
\bar{\bar{\mathbf{A}}}_1 & \bar{\bar{\mathbf{C}}}_1 & & & & & & & & & \bar{\bar{\mathbf{H}}}_1 \\
\bar{\bar{\mathbf{B}}}_2 & \bar{\bar{\mathbf{A}}}_2 & \bar{\bar{\mathbf{C}}}_2 & & & & & & & & \bar{\bar{\mathbf{H}}}_2 \\
\bar{\bar{\mathbf{Z}}}_3 & \bar{\bar{\mathbf{B}}}_3 & \bar{\bar{\mathbf{A}}}_3 & \bar{\bar{\mathbf{C}}}_3 & & & & & & & \bar{\bar{\mathbf{H}}}_3 \\
\bar{\bar{\mathbf{V}}}_4 & \bar{\bar{\mathbf{Z}}}_4 & \bar{\bar{\mathbf{B}}}_4 & \bar{\bar{\mathbf{A}}}_4 & \bar{\bar{\mathbf{C}}}_4 & & & & & & \bar{\bar{\mathbf{H}}}_4 \\
 & \cdot & \cdot & \cdot & \cdot & \cdot & & & & & \cdot \\
 & & \bar{\bar{\mathbf{V}}}_i & \bar{\bar{\mathbf{Z}}}_i & \bar{\bar{\mathbf{B}}}_i & \bar{\bar{\mathbf{A}}}_i & \bar{\bar{\mathbf{C}}}_i & & & & \bar{\bar{\mathbf{H}}}_i \\
 & & & \cdot & \cdot & \cdot & \cdot & \cdot & & & \cdot \\
 & & & & \bar{\bar{\mathbf{V}}} & \bar{\bar{\mathbf{Z}}} & \bar{\bar{\mathbf{B}}} & \bar{\bar{\mathbf{A}}} & \bar{\bar{\mathbf{C}}} & & \bar{\bar{\mathbf{H}}} \\
 & & & & & \bar{\bar{\mathbf{V}}} & \bar{\bar{\mathbf{Z}}} & \bar{\bar{\mathbf{B}}} & \bar{\bar{\mathbf{A}}} & \bar{\bar{\mathbf{C}}} & \bar{\bar{\mathbf{H}}} \\
 & & & & & & \bar{\bar{\mathbf{V}}}_I & \bar{\bar{\mathbf{Z}}}_I & \bar{\bar{\mathbf{B}}}_I & \bar{\bar{\mathbf{A}}}_I & \bar{\bar{\mathbf{H}}}_I \\
-- & -- & -- & -- & -- & -- & -- & -- & -- & -- & -- \\
\bar{\bar{\mathbf{G}}}_1 & \bar{\bar{\mathbf{G}}}_2 & \bar{\bar{\mathbf{G}}}_3 & \cdot & \bar{\bar{\mathbf{G}}}_i & \cdot & \cdot & \cdot & \cdot & \bar{\bar{\mathbf{G}}}_I & \bar{\bar{\mathbf{G}}}_g
\end{bmatrix}
\times
\begin{bmatrix} \bar{\delta}_1 \\ \bar{\delta}_2 \\ \bar{\delta}_3 \\ \bar{\delta}_4 \\ \cdot \\ \bar{\delta}_i \\ \cdot \\ \bar{\delta} \\ \bar{\delta} \\ \bar{\delta}_I \\ -- \\ \bar{\delta}_g \end{bmatrix}
=
\begin{bmatrix} -\bar{\mathbf{R}}_1 \\ -\bar{\mathbf{R}}_2 \\ -\bar{\mathbf{R}}_3 \\ -\bar{\mathbf{R}}_4 \\ \cdot \\ -\bar{\mathbf{R}}_i \\ \cdot \\ -\bar{\mathbf{R}} \\ -\bar{\mathbf{R}} \\ -\bar{\mathbf{R}}_I \\ -- \\ -\bar{\mathbf{R}}_g \end{bmatrix}
\tag{3.8}
$$

The unknown vector for each block is $\bar{\delta}_i = (\delta n_{i,1\to J},\ \delta\rho_{i,1\to J-1})$, corresponding to the density changes and displacements on the i quasi-normal line. The $\bar{\mathbf{R}}_i$ terms are the Newton residuals for the S-mom. and N-mom. equations. Additional global unknowns $\bar{\delta}_g$ and constraint equations, made up of $\bar{\bar{\mathbf{G}}}_i$ entries for the interior flow unknowns, and $\bar{\bar{\mathbf{G}}}_g$ entries for the global unknowns, do not fit within the compact block structure. The $\bar{\bar{\mathbf{H}}}_i$ blocks represent the effect of the global unknowns on the S-mom. and N-mom. equations. Further details on the block structure of the matrix and solution are presented in Appendix D.

3.1.5 Global Variables and DOF's

The large, sparse matrix in 3.8 is solved using a specialized direct solver that divides the full matrix into a banded matrix and a small matrix for the global unknowns. The global influence columns $\bar{\bar{\mathbf{H}}}$ are simply treated as additional right-hand sides, so that the addition of global unknowns, or DOF's to the system, increases the solution cost by a negligible 3% per DOF. This treatment of global variables as separate unknowns with global constraint equations adds considerable flexibility in the implementation of boundary conditions or design conditions. The equation added to constrain a DOF need only be well-posed, it does not even need to directly involve the global variable.

For example, the exit angle s_{out} can be explicitly set, typically resulting in a pressure mismatch at the blade trailing edge. The unique (but unknown) exit slope that satisfies the Kutta condition can be found setting s_{out} as a DOF and adding a pressure equality constraint equation at the trailing edge

$$\Pi^{-}_{i_{TE},1} - \Pi^{+}_{i_{TE},J} = 0 \tag{3.9}$$

Most of the quantities that affect the boundary conditions can be used as DOF's and have corresponding direct constraint equations, see Table 3.2.

Table 3.2: Direct constraint equations for global DOF's.

DOF	Global Unknown	Direct Constraint Equation
s_{inl}	δs_{inl}	$s_{inl} - s_{inl_{spec}} = 0$
s_{out}	δs_{out}	$s_{out} - s_{out_{spec}} = 0$
c_{inl}	δc_{inl}	$c_{inl} - c_{inl_{spec}} = 0$
$\dot{m}$	$\delta \dot{m}$	$\dot{m} - \dot{m}_{spec} = 0$
p_{exit}	δp_{exit}	$p_{exit} - p_{exit_{spec}} = 0$

The power of the global variable/global constraint arrangement can be used to provide some powerful capabilities for cascade work. For example, the inlet characteristic global variable c_{inl} can be used to set the Mach number into the infinite cascade when it is paired with a constraint equation for the mass-averaged Mach number at the inlet station $i = 2$.

$$\sum_{j=1}^{J-1} \frac{\dot{m}_j}{\dot{m}} M_{i,j} - M_{spec} = 0 \tag{3.10}$$

The Mach constraint equation can be generalized and applied across a line at any specified position in the cascade. This is particularly valuable for determining the exit pressure for a cascade corresponding to a given flow condition. The exit pressure p_{exit} is set as a DOF, constrained by the mass averaged Mach number constraint applied at

a specified position in the cascade. If the Mach number is specified as $M_{spec} = 1.0$ this constraint can be used to set the position of a normal shock, although this condition must be used with some care so that the desired shock position and Mach number is physically realizable. The exit pressure to attain a given exit Mach number can also be determined using this technique.

Blades with round leading edges add a DOF for tangential movement of the leading edge stagnation point. This is handled by sliding the streamline nodes along the blade surface accordian-fashion to match the stagnation node movement. The leading edge movement is implemented as a a global grid displacement DOF that also moves nearby nodes in the interior mesh to minimize local grid skewing. The displacement of each grid node depends on normal streamline displacements and on the global DOF s_{LE}.

$$\delta\,(x_{i,j}\,\hat{\imath} + y_{i,j}\,\hat{\jmath}\,) = \delta n_{i,j}\,\hat{n}_{i,j} + \delta s_{LE}(x_{LE_{i,j}}\,\hat{\imath} + y_{LE_{i,j}}\,\hat{\jmath}) \tag{3.11}$$

The position of the stagnation point s_{LE} is constrained by a leading edge Kutta condition similar to the trailing edge Kutta condition 3.9. This is covered in more detail in reference [9].

3.2 Boundary Layer Coupling

Viscous effects are included by modifying the wall boundary condition on blade and wake streamlines using the displacement surface concept. The condition that fixes the wall streamline to the blade surface from Table 3.1 is replaced by

$$\delta n_i - \delta(\delta_i^*) = \delta_i^* - \Delta n_i \tag{3.12}$$

where δ^* is the BL displacement thickness, and Δn is the streamline offset distance, as shown in Figure 3.5. The same condition is used on the wake, but the thickness is applied between the two streamlines bounding the wake.

The theory and numerical implementation of the boundary layer solution is given in references [9, 12, 13]. Details of the quasi-3D modifications and matrix implementation are contained in the Appendices.

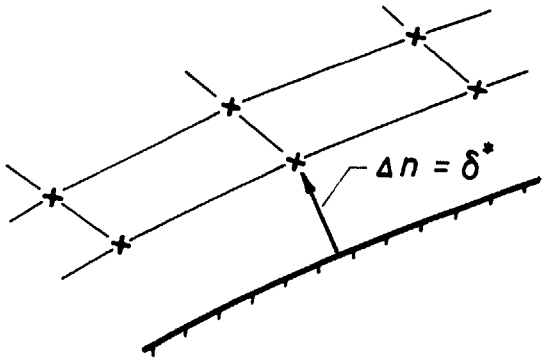

Figure 3.5: Boundary conditions for viscous coupling.

3.3 Design Capabilities

The streamline-based method makes possible a variety of useful design capabilities. The classical inverse problem, where the geometry corresponding to a prescribed surface pressure is determined, is easily implemented with the current approach by replacing the boundary condition imposing the displacement of surface nodes with an imposed surface pressure condition. Full inverse design is rarely used in practice, however, and has been removed from the current method, in favor of mixed-inverse design. The mixed-inverse problem, where one portion of the geometry is prescribed and the other is to be designed, is better suited to the iterative nature of design where problem areas are identified and fixed on a local basis. For cases with areas of strongly constrained geometry, such as the supersonic zones on a transonic airfoil or the supersonic surface of a supersonic cascade, it is essential that only localized geometric changes be made. Both of these methods are fully described in reference [9]. Note that these techniques are only marginally useful for separated flow cases, where the local geometry is poorly constrained by the pressure.

For external aerodynamics, where viscous effects are usually second-order, design changes are made inviscidly to maintain profile smoothness, and a series of viscous check cases run to assess performance. This inviscid redesign strategy is likely to fail for cascades due to the strong viscous coupling, involving some degree of separated flow

at the operating point[1]. An alternative strategy is to deal with a fixed set of geometric modes to perturb the airfoil contour, assuring that any design changes remain smooth without locally wild behavior. For a modal scheme the surface node displacement is given by a sum of geometric perturbations

$$\delta n_i = \sum_{\ell=1}^{L} \delta\tilde{n}_\ell \, g_\ell(s_i) \tag{3.13}$$

where the L geometric modes $g_\ell(s)$ are defined in terms of surface arc length and have mode amplitudes $\tilde{n}_\ell$. Seven geometric modes are implemented in the current method and are used in for a redesign case in Chapter 5. The mode shapes are shown in Figure 3.6, although any reasonably orthogonal set of perturbations could be used. The modes can

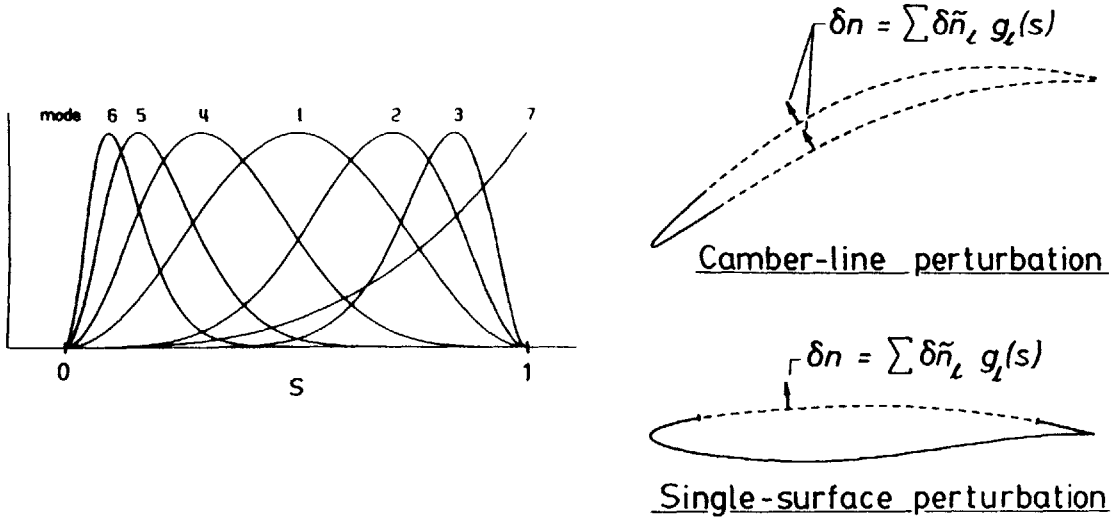

Figure 3.6: Mode shapes and design modes for geometric perturbations.

be used to perturb all or any specified region of a single blade surface, or the same perturbation could be applied to opposing sides on both blade surfaces. The latter possibility is equivalent to a camber redesign mode, preserving blade thickness. The mode amplitudes $\tilde{n}_\ell$ can be set as global DOF's with global unknowns $\delta\tilde{n}_\ell$. The modes can be specified directly using the corresponding direct modal constraint equations

$$\tilde{n}_\ell - \tilde{n}_{\ell_{spec}} = 0 \tag{3.14}$$

[1] The possible exception being for blading designed to avoid separation, e.g. DCA sections.

For modal-design cases, the surface displacement boundary condition, 3.12, is modified with an extra term corresponding to the geometric modes.

$$\delta n_i \; - \; \delta(\delta_i^*) \; = \; \delta_i^* \; - \; \Delta n_i \; + \; \sum_{\ell=1}^{L} \delta \tilde{n}_\ell \; g_\ell(s_i) \tag{3.15}$$

Note that the streamline is still offset from the airfoil by the boundary layer thickness, but the blade surface can be displaced by the geometry modes.

The inverse modal formulation minimizes the integrated mismatch between a specified and resulting surface pressure distribution. The discrete form for this is

$$I \; \equiv \; \frac{1}{2} \sum_i \left(p_i - p_{\text{spec}}(s_i) \right)^2 \tag{3.16}$$

summed only over the inverse segment. Minimization constraints are obtained in the standard way by setting the variations with respect to the mode amplitudes to zero.

3.4 Multiple Blades

One of the goals for the current work is the development of methodology for analysis and design of cascades with splitter vanes. The problem was approached from a general point of view so that any number of intermediate blades may be used, although the discussion and examples focus on one splitter vane. The basic configuration for a cascade with splitter vane is shown in Figure 3.7. The intermediate blade introduces an additional stagnation line that splits at the leading edge to define the upper and lower surface streamlines with associated boundary layers. This stagnation line also acts as a dividing streamline between the upper and lower passages, each with its own mass flow. The relative passage mass flows are set by the position of the stagnation line at the inflow boundary, which is in turn set by the trailing edge Kutta condition, $\Delta\Pi = 0$ on the intermediate blade.

The streamline grid structure is modified for a splitter vane as shown in Figure 3.8, where the stagnation streamline for the intermediate blade defines two grid streamlines and a *null streamtube* through which there is no flow. The conditions on the new

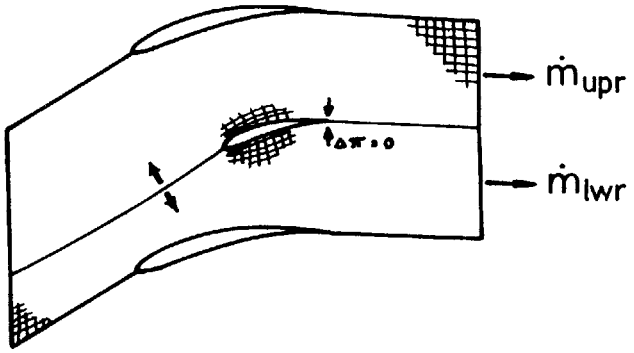

Figure 3.7: Cascade with splitter blade, showing stagnation lines.

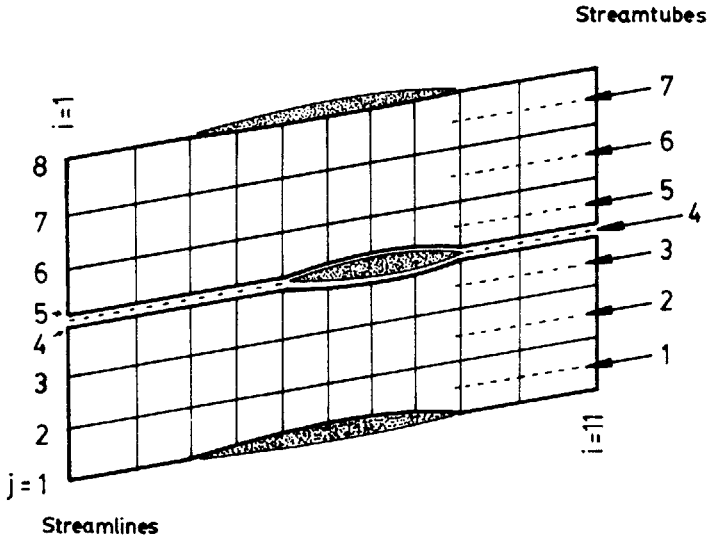

Figure 3.8: Grid arrangement for multiple blades.

stagnation streamlines are handled by generalizing the periodic boundary conditions in Table 3.1 for the $j = 1$ and $j = J$ domain boundaries to apply across adjacent streamlines. Further details on the treatment of multiple blades are covered in Appendix D.

3.4.1 Global Variables and DOF's for Multiple Blades

The stagnation line for the intermediate blade divides the cascade into upper and lower passages with mass flows, $\dot{m}_{lwr}$ and $\dot{m}_{upr}$. This effectively introduces a new global unknown for mass flow into the system. It is convenient to treat the two unknown mass flows as a total mass flow $\dot{m} = \dot{m}_{lwr} + \dot{m}_{upr}$ and a differential mass flow $\Delta\dot{m} = \dot{m}_{upr} - \dot{m}_{lwr}$. This allows the total mass flow to be imposed from upstream conditions and the differential mass flow determined by a single added DOF. The global unknown for differential mass flow is normally constrained by a global equation for the trailing edge Kutta condition on the intermediate blade. It may also be directly specified by a constraint equation for the mass-fraction-ratio $m_{fr} = \dot{m}_{upr}/\dot{m}_{lwr}$,

$$\frac{\dot{m}_{upr}}{\dot{m}_{lwr}} - m_{fr_{spec}} = 0 \tag{3.17}$$

Each additional blade with a blunt leading edge also requires a DOF and constraint equation for LE stagnation point movement, similar to the main blade. The global grid movement mode that accompanies leading edge movement extends only over the passages immediately above and below the blade.

Two new design modes have been added for intermediate blade redesign – a blade displacement mode D_{mov} and a blade shearing mode D_{rot}. The movement mode moves the blade in the circumferential direction and is used to change the mass flow fraction between the flow passages. The shearing mode maintains axial chord and trailing edge position and is used primarily for modal design and modal inverse redesign. Figure 3.9 shows the associated mode shapes at the splitter blade. These modes differ from the modal design modes in Figure 3.6 because they are not limited to modal displacements along the streamline normal direction and they are global in the sense that they specify displacements for every grid node. The global modes are treated in a similar way as

the leading edge movement mode. In practice any reasonably well-defined mode shape could be used in place of the movement or shearing modes. The form for the node displacement equation includes both normal displacements δn and global displacements from movement and rotation modes which specify x and y nodal displacements for the entire grid, for example

$$\delta\,(x_{i,j}\,\hat{\imath} + y_{i,j}\,\hat{\jmath}\,) = \delta n_{i,j}\,\hat{n}_{i,j} + \delta D_{mov}(x_{mov_{i,j}}\,\hat{\imath} + y_{mov_{i,j}}\,\hat{\jmath}) \tag{3.18}$$

The new modes can be set as DOF's and have direct constraint equations similar to the direct modal constraints 3.14. The intermediate blade global modes may be mixed with the geometric modes in inverse design calculations where an inverse pressure constraint similar to 3.16 is used. Alternatively the mass fraction constraint in 3.17 can be used to drive the blade position to give a specified mass flow ratio across the blade.

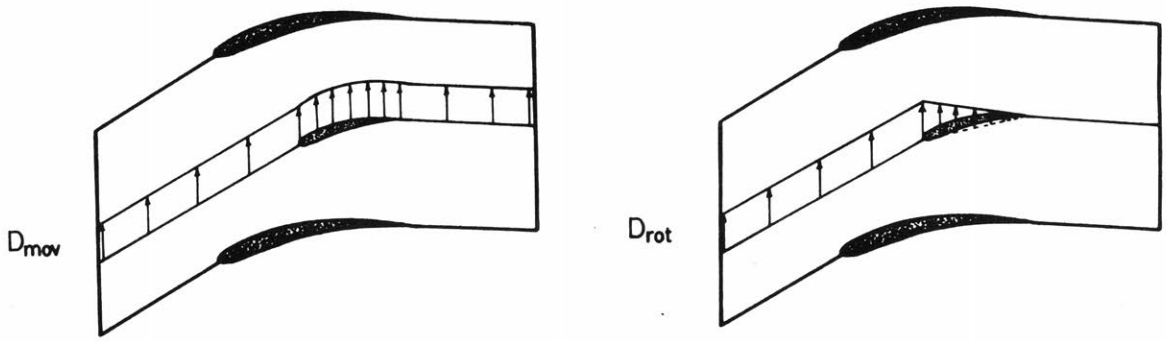

Figure 3.9: Design modes for splitter movement and rotation.

3.4.2 Grid Generation

Since the velocity and pressure are determined by streamtube geometry, a streamline grid generator is used to supply the initial guess for the flow field. Grid generation for a single blade cascade is relatively straightforward — once a distribution of nodes is established on the domain boundaries an elliptic grid generator is used to establish the position of interior nodes, determining the streamlines and quasi-normal lines. The

normal spacing of streamlines is set by the fractional mass flow through each streamtube. The resulting grid essentially corresponds to an incompressible flow solution for the assumed positions of the inflow and exit stagnation lines.

The multiple blade grid is generated in similar fashion, treating each of the flow passages as an independent domain, bordered by stagnation streamlines. Two difficulties are introduced for multiple blades.

1. The position of the intermediate stagnation lines is not known a priori.
2. The initial node spacing on stagnation lines strongly affects grid skew in the interior mesh. Grid skew has little effect in subsonic flow but can lead to serious problems for supersonic cascades (this will be discussed in the following section).

The approach used for cascades assumes the main and intermediate blades are not closely spaced (as they would be in a multi-element airfoil) and that a cascade 'meanline' based on axial position can be defined using the stagnation line and camberline of the main blade. The position of an intermediate stagnation line can be determined from the 'meanline' using the relative circumferential position of the intermediate blade at the leading or trailing edge, i.e.

$$y_{stag}(x) = y_{m.l.}(x) + \eta\, y_{pitch} \qquad \text{with } \eta = \frac{y_{LE} - y_{m.l.}(x_{LE})}{y_{pitch}}$$

The resulting stagnation line is smoothed to even out any remaining discontinuities.

Spacing on stagnation lines is handled using a curvature-based node distribution on the blades and a primitive blocking scheme to roughly match spacing on inlet and exit streamlines. This sometimes requires user interaction to achieve a satisfactory grid but is largely automatic. As the blades become more closely spaced, e.g. the ARL tandem splitter in Chapter 5, the spacing requirements become more draconian and require greater user intervention. For such cases a different approach may be needed, subdividing the domain into grid blocks with an 'arbitration' scheme for resolving spacing requirements between blocks to obtain a compatible grid layout. A variant of the multiple blade cascade code has been applied to the multi-element airfoil problem by

Drela and uses a panel method solution to determine the initial stagnation line positions and node distribution.

3.5 Leading Edge Problems

The leading edge radii for cascade blades, especially supersonic blading, is typically much smaller than for airfoils — 0.5% for the DFVLR blade and 0.25% for the ARL supersonic cascade discussed in Chapter 4. Problems are sometimes encountered in resolving the flow near the leading edge stagnation point, particularly due to spurious velocity or total pressure loss from dissipation terms that become significant in the strong velocity gradients near the leading edge. The small radii can produce gradients that are difficult to distinguish from shocks, although the actual flow is nearly isentropic. Decelerating flow produces spurious loss, while accelerating flow can produce a total pressure increase. Typically only the first few streamtubes immediately adjacent to the blade are strongly affected. Unfortunately loss or gain in the inner stream tube has a strong effect on the boundary layer through changes in the edge velocity. Overall spurious loss effects thus depend on details of the alteration in edge velocity and on the inviscid loss.

One solution to this problem is to modify the leading edge geometry to alleviate the strong gradients by ellipticizing or sharpening it, although some of the genuine physics may be lost, particularly for supersonic blades with bow shocks. The ARL case, for example, shows a 6% loss in the innermost streamtubes due to the bow shock, although this represents a much smaller portion of the mass-averaged total loss. An alternative solution, implemented as an option, is to treat a region near the leading edge isentropically, completely eliminating dissipation loss or gain. The special treatment is limited to the two streamtubes immediately above and below the blade and extends from just downstream of a bow shock to a point behind the leading edge expansion. This allows the loss in the bow shock to be correctly modeled and minimizes spurious dissipation effects.

3.6 Grid Skew Problems for Supersonic Cascades

While the current approach for solving the inviscid flow works well for subsonic and transonic flows, and works well for supersonic airfoils, problems were encountered with supersonic cascades at high stagger angles. Grids with highly skewed cells were found to exhibit spurious odd-even instabilities in the flow field at supersonic conditions. These problems were associated with strong passage shocks or the leading edge wave system. Figure 3.10 shows the converged inviscid result for a sharp leading edge blade with 50° stagger. The waves upstream of the shock result from dispersion problems with the numerical scheme, similar to those found by Shapiro [14] for the linearized steady-state Euler equations. Shapiro showed that the dispersive behavior of several discrete operators were well predicted by his Fourier analysis but offered no wisdom on reducing the effect. Higher dissipation reduces the dispersive behavior only for mild cases, but results in increased shock smearing. The geometry of the streamlines and quasi-normals

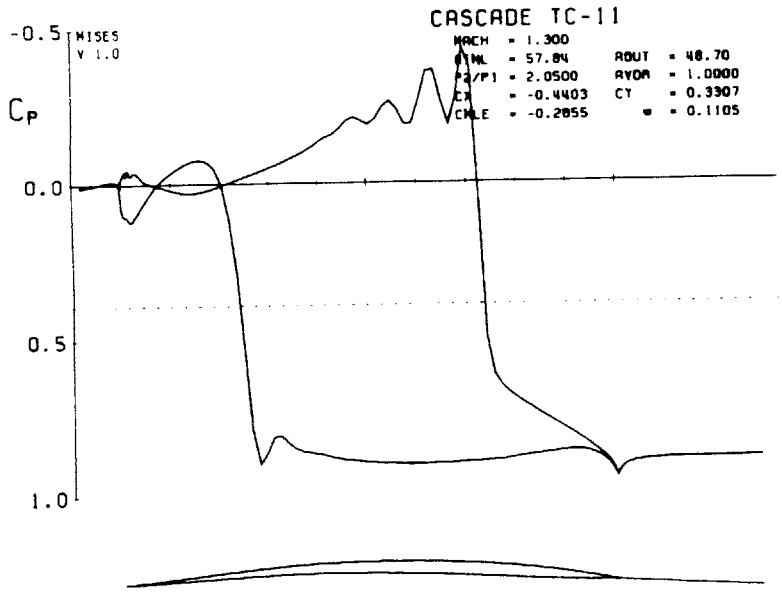

Figure 3.10: Dispersion effects at shock for skewed grid.

at the instability in a skewed grid is shown in Figure 3.11. The strongly oblique initial grid is further distorted at alternate streamline nodes, where the local Mach angle roughly matches the mean cell skew.

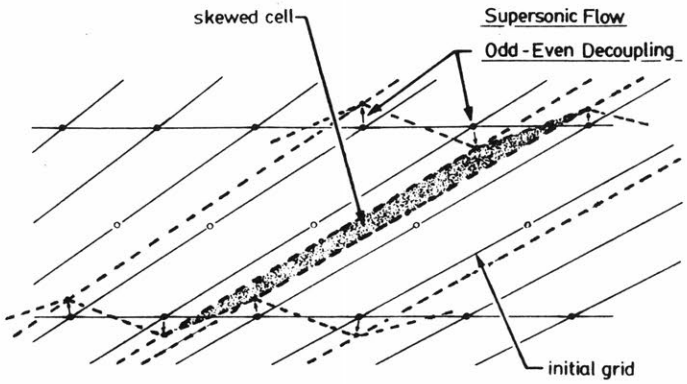

Figure 3.11: Supersonic odd-even instability for skewed grids.

The problem becomes more serious as the skew increases, leading to non-convergence or totally inconsistent solutions. The grid and Mach contours for a round leading edge blade, similar to the sharp edged blade above, is shown in Figure 3.12. The Mach contours show a 'lozenge' of accelerated flow (M=1.7) located below and upstream of the blade leading edge where the skew is highest. Note that the passage shock is also badly smeared by the axial elongation of cells in the skewed mesh.

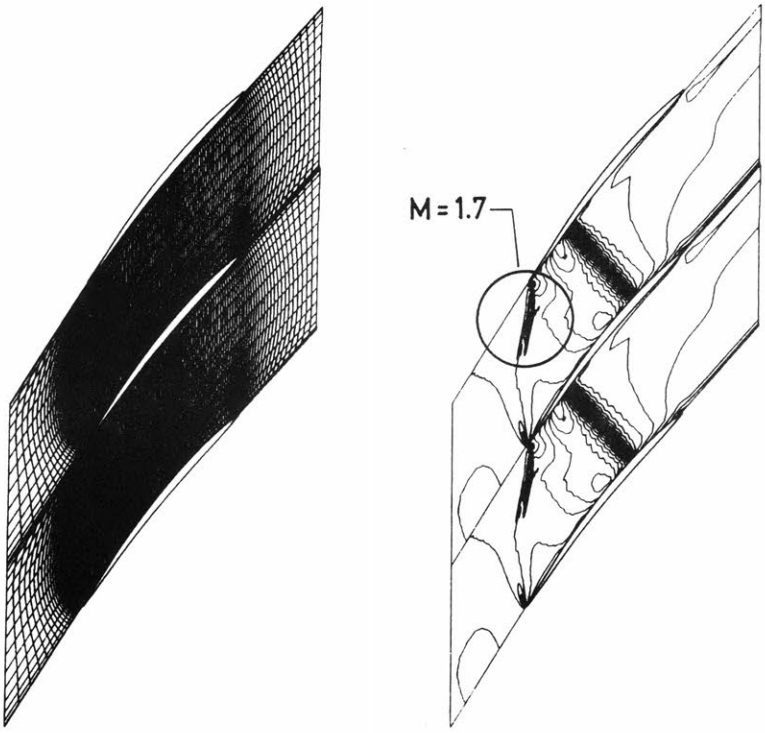

Figure 3.12: Grid and Mach contours for blunt LE blade, $\xi = 50°$, $M = 1.3$

3.7 Offset-Periodic Grid and Solution

Using the direct approach to problem solving, the skewed grid problems were solved by un-skewing the mesh in the inlet area. The topology of the grid was changed to make the quasi-normals roughly orthogonal to the streamlines in the inflow region. This results in a 'stairstep' grid, as shown in Figure 3.13, where the $j = 1$ and $j = J$ domain edges overlap but are shifted by a streamwise offset i_{off}.

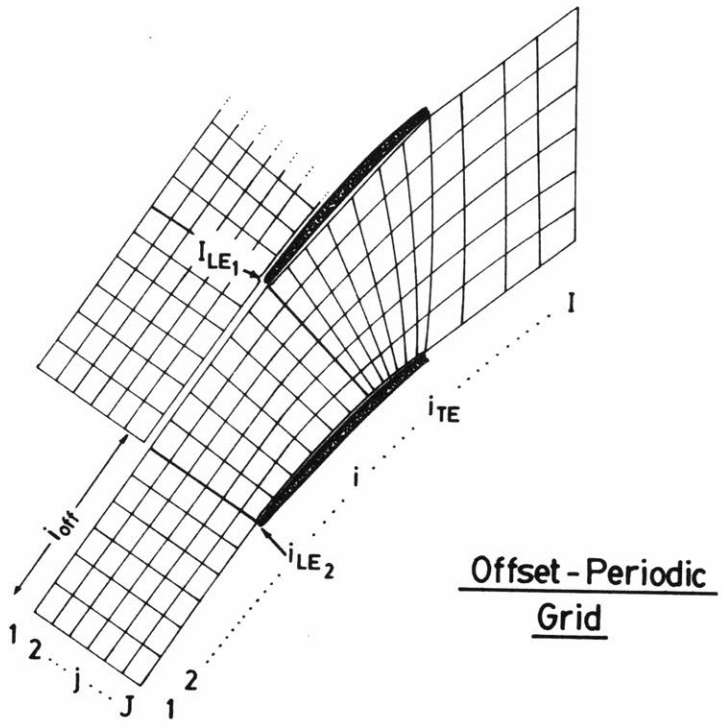

Figure 3.13: Layout of offset-periodic grid.

Skipping the details of the formulation for the moment, Figures 3.14 and 3.15 show results for the cascade from Figure 3.12 modeled with an offset-periodic grid. The dispersion problems are absent and the shock is well resolved as a result of the approximate alignment of the quasi-normals with the shock.

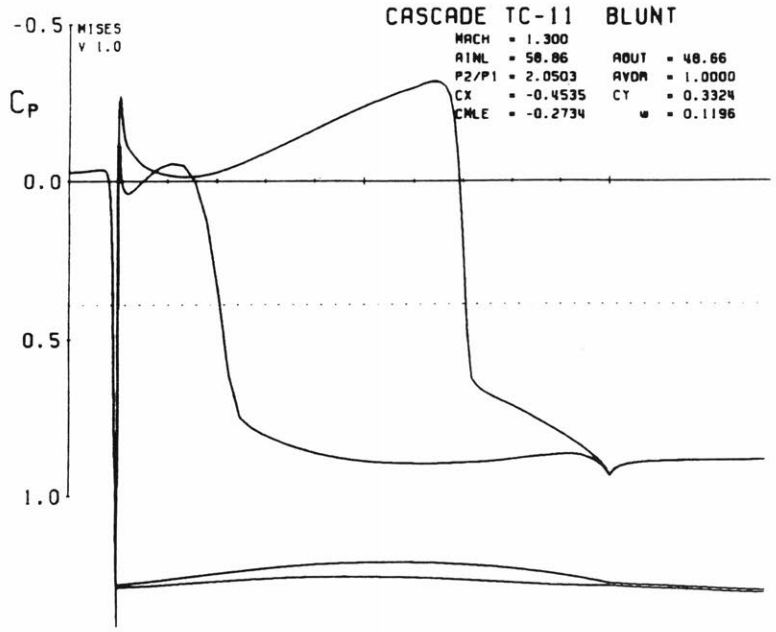

Figure 3.14: Pressure distribution for supersonic cascade with offset-periodic grid.

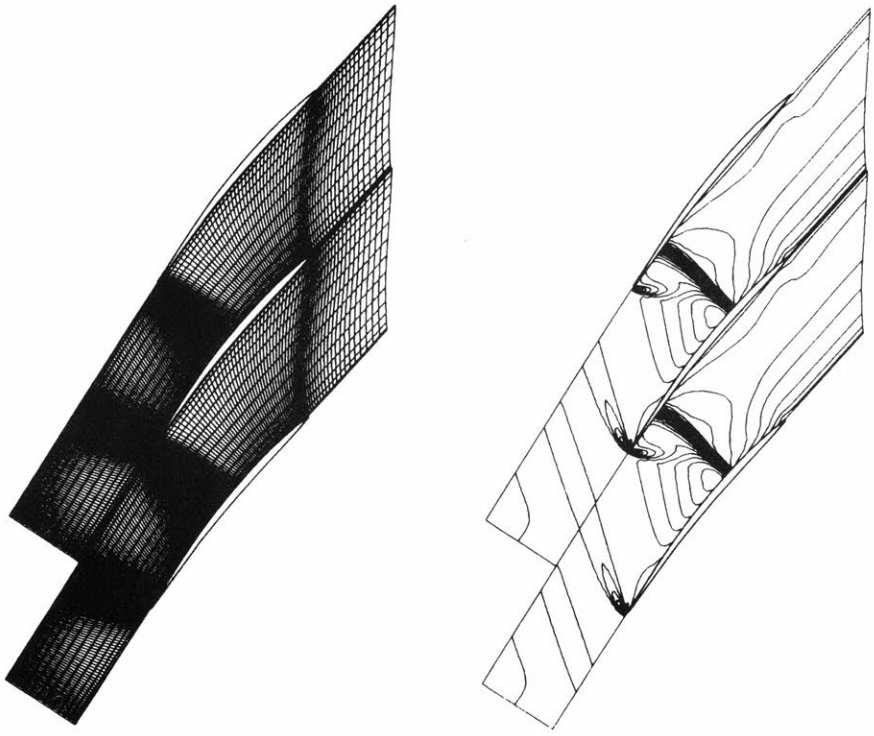

Figure 3.15: Grid and Mach contours for cascade with offset-periodic grid.

3.7.1 Offset-Periodic Matrices and Solution

The offset grid is configured with the offset portion of the grid extending from the inflow boundary to the trailing edge, $1 \leq i \leq i_{TE}$. The outflow conditions are thus not affected. Periodicity for the stairstep inlet is achieved with a modification of the periodic conditions from Table 3.1. The $\Delta n_i = 0$ geometric matching condition is applied across nodes i on streamline J and $i - i_{off}$ on streamline 1. Similarly for the pressure matching condition, where $\Pi_{i-i_{off},1} - \Pi_{i,J} = 0$. The offset inlet conditions alter the arrangement of terms in the block matrix 3.8 by moving these periodic terms to off-diagonal blocks, as shown in Figure 3.16.

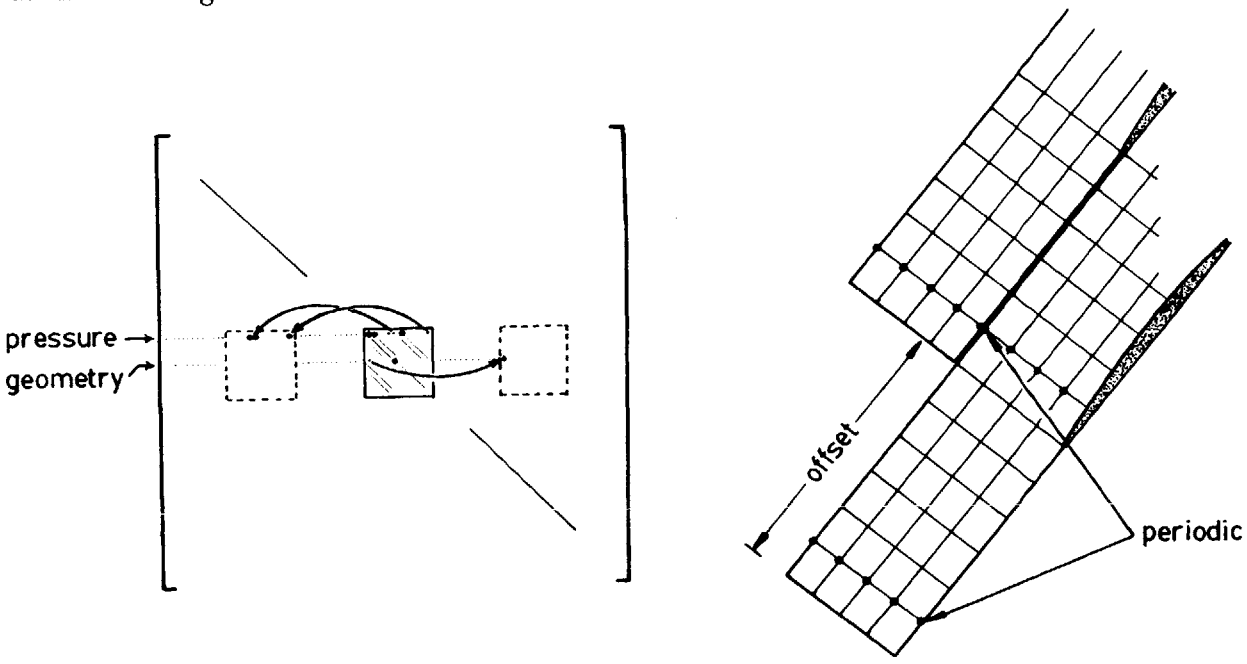

Figure 3.16: Arrangement of off-diagonal periodicity terms for offset grid.

The off-diagonal terms complicate the matrix solution somewhat and require modifications to the specialized direct solver. Note that to minimize fill-in of the upper triangle during the matrix solution the indicial order of streamlines in Figure 3.13 must be used. Further details on the offset matrix and solver are included in Appendix D.

3.7.2 Offset-Periodic BC

The new grid topology requires that boundary conditions be imposed on the *free boundary* streamline at $j = 1$ in the first offset block. The conditions specified on this streamline segment depend on the inlet Mach number.

Subsonic The local angle of $j = 1$ streamline segments is prescribed to be s_{inl}, the same condition used at the $i = 1$ face. The offset segments should be located far enough upstream that they are relatively unaffected by the disturbance from the blade, implying that subsonic cases should use at least three offset inlet blocks.

Supersonic/Axially Subsonic The local angles on the $j = 1$ streamline segments are set by the inlet characteristic c_{inl}. An area behind the $i = 1$ inlet face is in a forbidden-signal zone with respect to the wave system from the blades, so the local streamline angles on the $i = 1$ face are set to match the angle on the $i = i_{off}$ streamline segment on $j = 1$.

3.7.3 Offset-Periodic Grid Generation

Initial grid generation for the offset grids uses the concept of an inlet offset block, which becomes the basic unit determining the length of the inlet and the number of quasi-normal lines. The leading edge index on the upper and lower surface streamlines of the main blade are set by

$$i_{LE_{j=1}} = i_{LE_{j=J}} + i_{off} \quad \text{with} \quad i_{LE_{j=1}} = n_{blocks}\, i_{off}$$

The offset index i_{off} is set by the position on the $j = J$ upper surface of the quasi-normal line from the lower surface leading edge. The spacing of nodes on the streamline edges of each offset block is prescribed by its opposite upstream neighbor to maintain the shifted periodicity. One of the disadvantages of the offset grid is that it is generally wasteful of streamwise resolution over the blades. This is chiefly a problem at inlet Mach numbers near unity, where inlet waves are nearly normal to the inflow and longer

inlets are required. Fortunately, resolution in the streamwise direction is cheap, $O(I)$, due to the banded matrix structure.

Chapter 4
Results - Analysis Cases

Previous chapters have described the development of a method for quasi-3D blade-to-blade analysis and design. Since this effort is an extension of the ISES algorithm developed by Giles [15] and Drela [9] and duplicates the characteristics of the original method for their subsonic and transonic test cases, only results pertaining to the new capabilities will be presented. Effects of splitter position and redesign cases will be covered in the following chapter. The principal objectives for the test cases presented here are

- Investigate accuracy of loss prediction for a range of inlet Mach numbers.
- Validate the quasi-3D capabilities for AVDR (streamtube width) effects.
- Demonstrate the multiple blade capability on a highly loaded supersonic cascade with splitter blade.

In this chapter the method is exercised on several test cases for purposes of comparison and validation of the basic analysis capability. These cases do not include rotational effects.

- **UTRC Build I** - A subsonic, attached flow cascade at a Mach number of 0.113 for low speed loss comparison.
- **DFVLR L030-4** - A transonic and low supersonic compressor cascade at Mach numbers from 0.82 to 1.10 and a range of AVDR.
- **ARL Splitter** - A supersonic, highly loaded compressor cascade with splitter vane at an inlet Mach number of 1.46 with strong streamtube contraction.

4.1 General Effect of AVDR

The axial velocity-density ratio, or AVDR, is related to the streamtube width by

$$\text{AVDR} = \frac{\rho_2 q_{x_2}}{\rho_1 q_{x_1}} = \frac{b_1}{b_2} \tag{4.1}$$

The conservation of y-momentum dictates that $q_{y_2} = q_2 \sin\beta_2$ is constant, defining a relation between AVDR and exit angle.

$$\tan\beta_2 = \frac{\rho_2 K}{\text{AVDR}} \qquad \text{where K is a constant set by inlet conditions} \tag{4.2}$$

The effect of AVDR is to change axial velocity at the cascade exit, affecting both the inviscid flow (exit angle and pressure) and the boundary layer development. The effect on the viscous flow is especially pronounced for highly-loaded blades, where boundary layers at or beyond the point of separation show strong effects on blockage and/or loss from a small relief in adverse velocity gradient. In a subsonic, unchoked cascade AVDR uniquely determines both exit pressure and exit angle. In a choked or supersonic cascade AVDR determines only the exit angle, since the exit pressure is not uniquely set by inlet conditions and geometry.

4.2 UTRC Low Speed Cascade

The intent of this comparison is to validate the cascade loss model for a low speed case without separation or strong compressible effects. Data was obtained from a $M = 0.113$ test of a DCA blade (Build-I) by UTRC in Reference [16]. A conventional 132x20 grid was used for this case, as shown in Figure 4.1. Linear streamtube width variation was assumed, with an AVDR = 1.023. Free transition was used for the MISES comparison, as experimental pressure data indicated that separation bubbles were present on both upper and lower surfaces, not surprising in light of the low Reynolds number of 4.78×10^5. The surface pressures compare well to test data, with good definition of both upper and lower separation bubbles, see Figure 4.2. The loss comparison is excellent, although the predicted turning is slightly greater than the test ($+2.2°$).

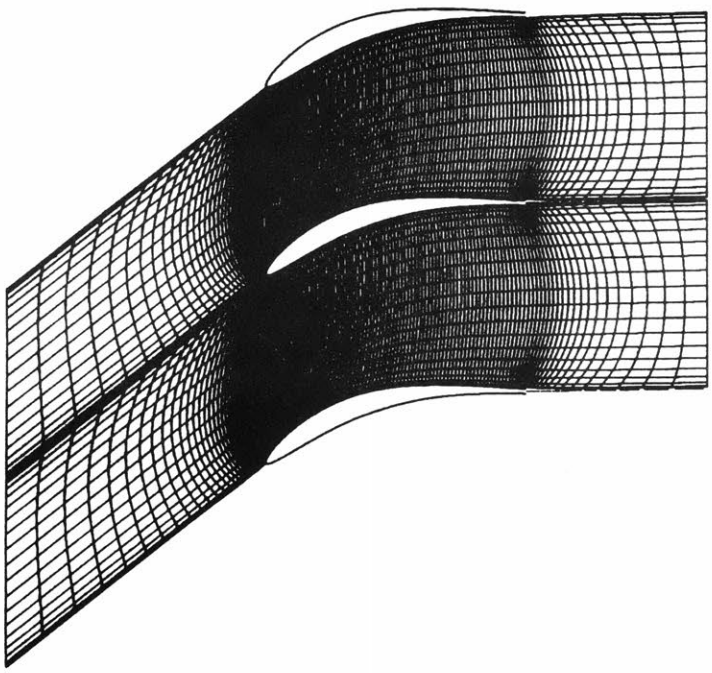

Figure 4.1: UTRC test case grid 132x20

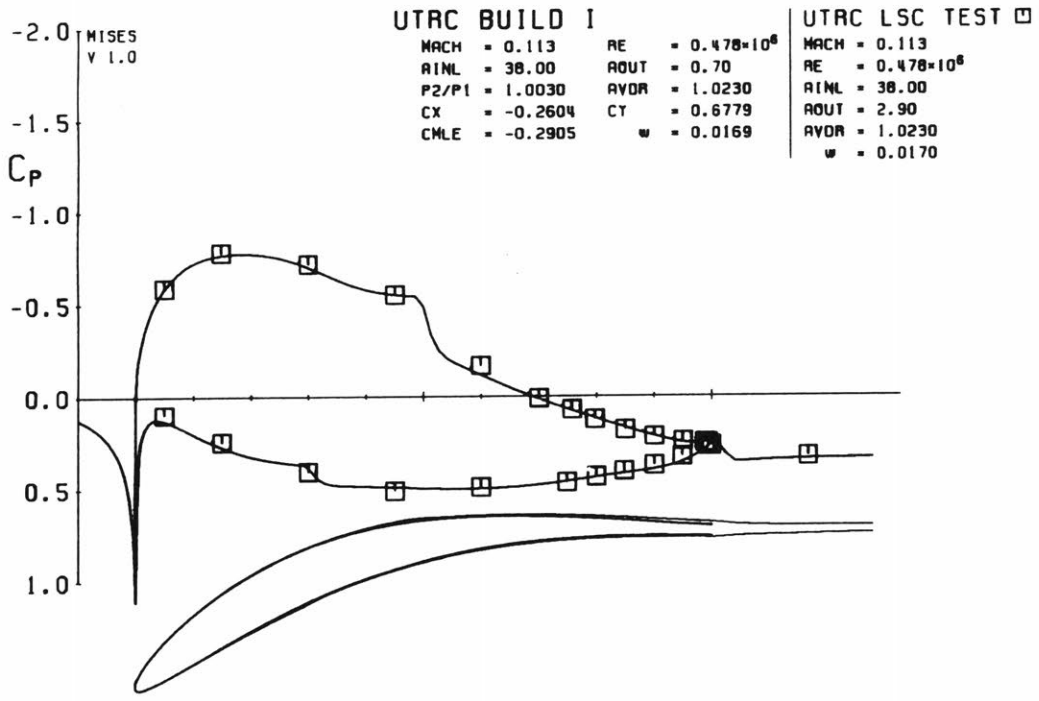

Figure 4.2: Pressure distribution for UTRC Build I: $M = 0.113$, $\beta_1 = 38.0°$, AVDR = 1.023

4.3 DFVLR Cascade

This case analyzes the flow in a two-dimensional low turning compressor cascade at transonic and low supersonic inlet Mach numbers. Comparison data was obtained from Schreiber&Starken [17] with additional detailed data for two specific supersonic operating points from Reference [18]. This data includes overall performance data for Mach numbers from 0.82 to 1.1 at a range of inlet angles and AVDR. Surface pressures were measured at several AVDR for the same inflow conditions, making this a useful test case for quasi-3D effects.

4.3.1 Section Characteristics

The cascade corresponds to the 45% height section from a rotor designed with MCA profiles for a 1.51 pressure ratio with a tip Mach number of 1.38. The blade section, shown in Figure 4.3, has a design Mach number of 1.09 and stagger angle $\xi = 48.51°$. The blade definition from Reference [18] was used, with a circular leading edge and thick trailing edge (0.695%).

4.3.2 Experimental Flow Conditions

The testing configuration used for the DFVLR cascade presents several problems for comparison of experimental and computational results.

- The exact inlet conditions at the cascade were not measured but were assumed to correspond to far-upstream conditions.
- For supersonic flow, no upstream wedge or similar device was used to establish periodic flow. The first blade set the inlet flow field for the remaining blades.
- Sidewall and endwall suction was used to minimize sidewall boundary layer effects *and* to change AVDR through the cascade!

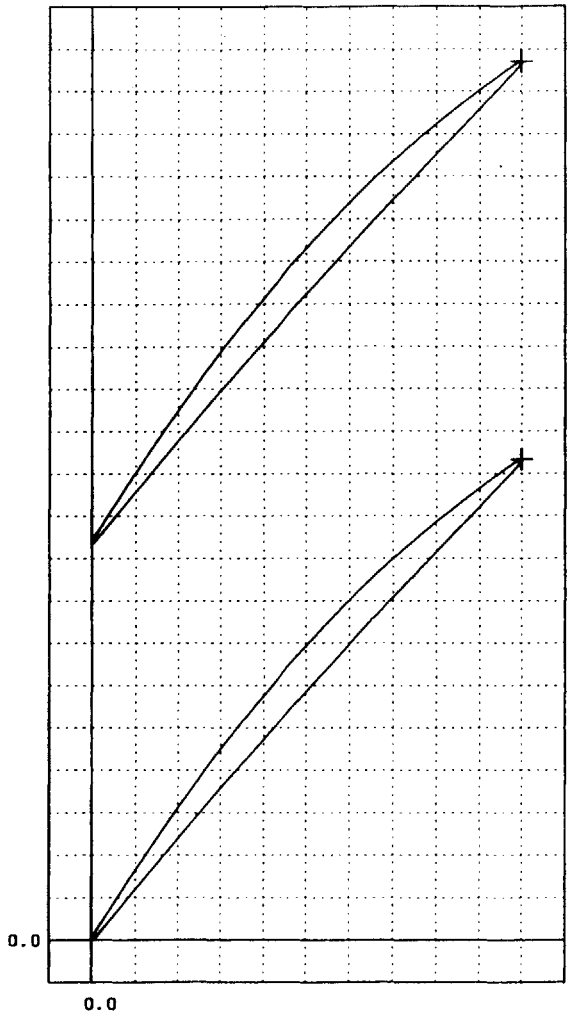

Figure 4.3: Blade section for DFVLR tests

As a result, the inlet flow conditions corresponding to an "infinite" cascade are not known. Experimental exit pressures were not supplied, except for the final two cases, so supersonic cases were compared by adjusting exit pressures to match experimental pressure distributions at the blade trailing edge.

The Reynolds number for these tests was 1.45×10^6 and turbulent flow conditions were assumed, using transition at 2% chord for upper and lower surfaces.

4.3.3 Comparison of AVDR Effects

Since Mach numbers for this comparison were close to $M = 1.0$, a relatively long inlet length was used to define the grid for the MISES computations. A grid density of 220x20 was used for this case with 4 offset blocks in the inlet region, as shown in Figure 4.4. The streamtube width between leading edge and trailing edge was assumed to be linear. Isentropic treatment was used near the blade leading edges to minimize spurious dissipation losses near the stagnation point.

Figure 4.4: Offset-periodic 220x20 grid for DFVLR cases

Surface pressure data at inlet Mach numbers of 0.82, 0.92, 1.03 and 1.10 are compared in Figures 4.5 through 4.8 In each figure experimental and computed pressures are compared for two AVDR values. The upstream inlet angle was constant $\beta_1 = 58.5°$ for all Mach numbers. The pressure coefficient C_{p_0} was used for this comparison, defined by

$$C_{p_0} = \frac{p_{0_1} - p}{p_{0_1} - p_1} \tag{4.3}$$

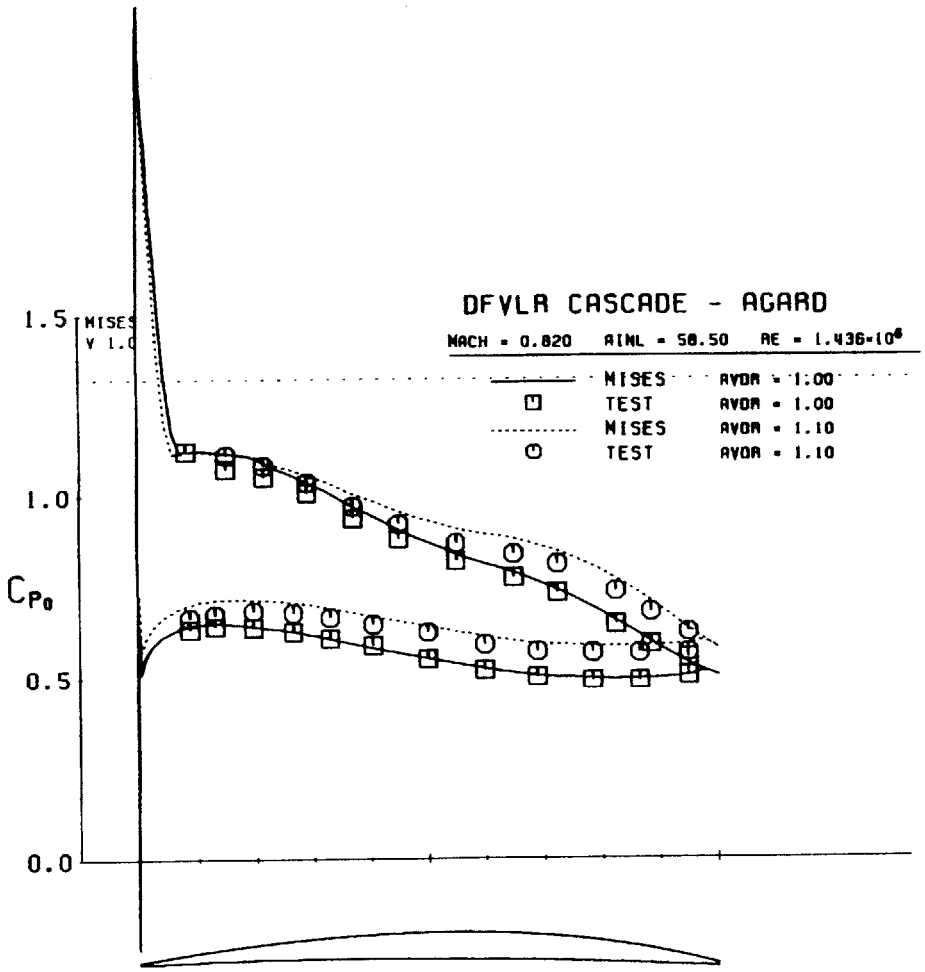

Figure 4.5: AVDR Effect on DFVLR blade: $M = 0.82$, $\beta_1 = 58.5°$.

Transonic Cases

Figures 4.5 and 4.6 compare surface pressures for transonic inlet Mach numbers of $M = 0.82$ and $M = 0.92$. For these cases the experimental inlet angle and Mach number were used as boundary conditions for MISES results. Surface pressures for the $M = 0.82$ case compare closely at the tested AVDR. At Mach 0.92 the lower surface and trailing edge pressures were best matched to test data by using a slightly higher AVDR (1.04). The general agreement for the pressures is good, although the test data for $M = 0.92$, AVDR = 1.17 shows a longer supersonic region on the blade upper surface. The effective inlet Mach number may be higher than 0.92, possibly resulting from suction effects on the sidewall boundary layer changing the upstream streamtube width.

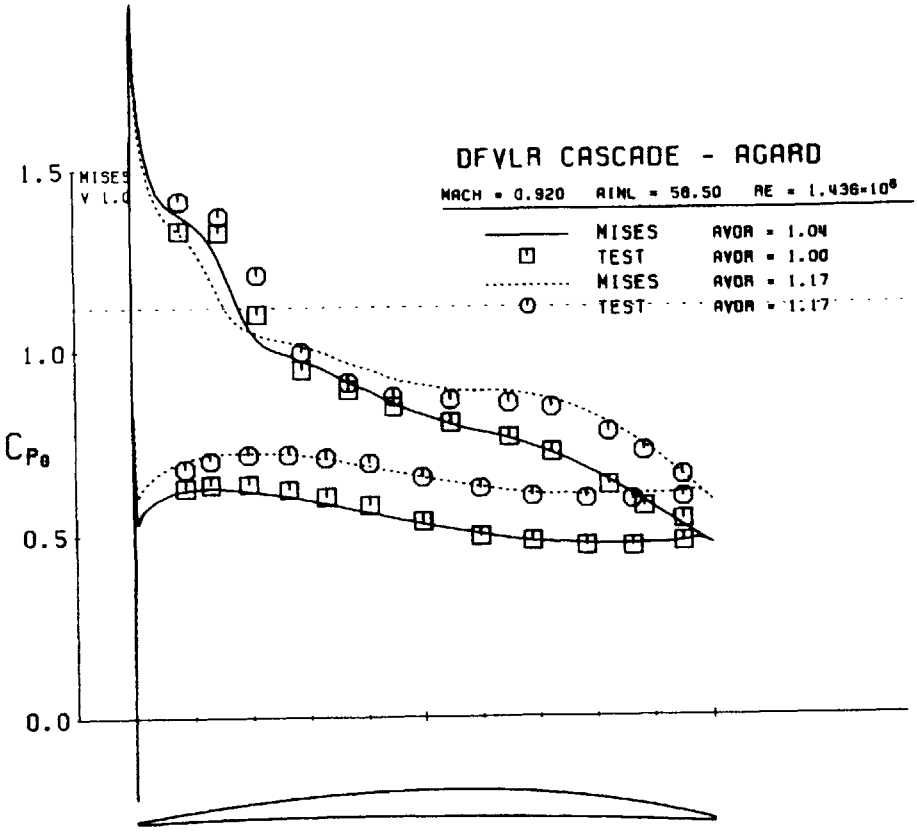

Figure 4.6: AVDR Effect on DFVLR blade: $M = 0.92$, $\beta_1 = 58.5°$.

Supersonic Cases

Figures 4.7 and 4.8 compare MISES results with test data for the supersonic $M = 1.03$ or $M = 1.10$ cases. Since exit pressures were not specified in Reference [17], they were adjusted to match surface pressures at the blade trailing edge. A global DOF using c_{inl} to drive mass flow was used to match mass flow from the upstream test conditions, resulting in a different Mach number and inlet angle at the infinite cascade due to the blade wave system. MISES pressures were re-normalized to the test condition dynamic pressures to permit comparison of C_{p_0}.

The pressures compare well except for $M = 1.10$, AVDR $= 1.15$ where the lower surface shock near the leading edge indicates that the specified mass flow may be excessive. Alternate boundary conditions, using a specified $c_{inl} = [c_{inl}]_{upstream}$ inflow condition, made very little change in the results, although the loss levels were slightly lower, $\Delta\omega = -0.002$.

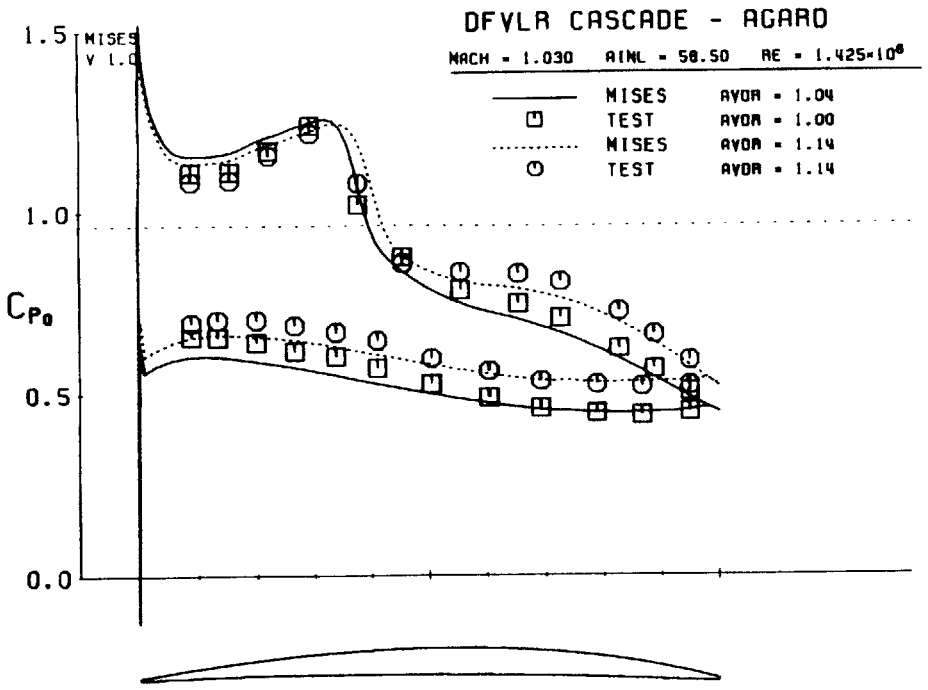

Figure 4.7: AVDR Effect on DFVLR blade: $M = 1.03$, $\beta_1 = 58.5°$.

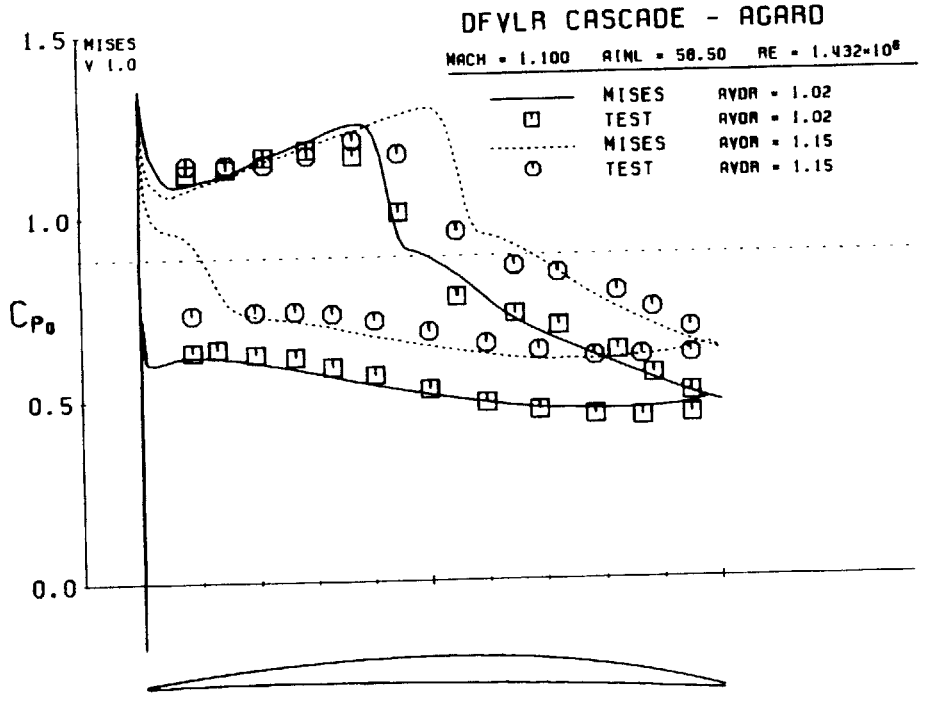

Figure 4.8: AVDR Effect on DFVLR blade: $M = 1.10$, $\beta_1 = 58.5°$.

4.3.4 Loss Comparison

The loss data for the flow conditions in Figures 4.5- 4.8 are compared with experimental loss data in Figure 4.9. The differences in loss for low AVDR = 1.0 – 1.04 and high

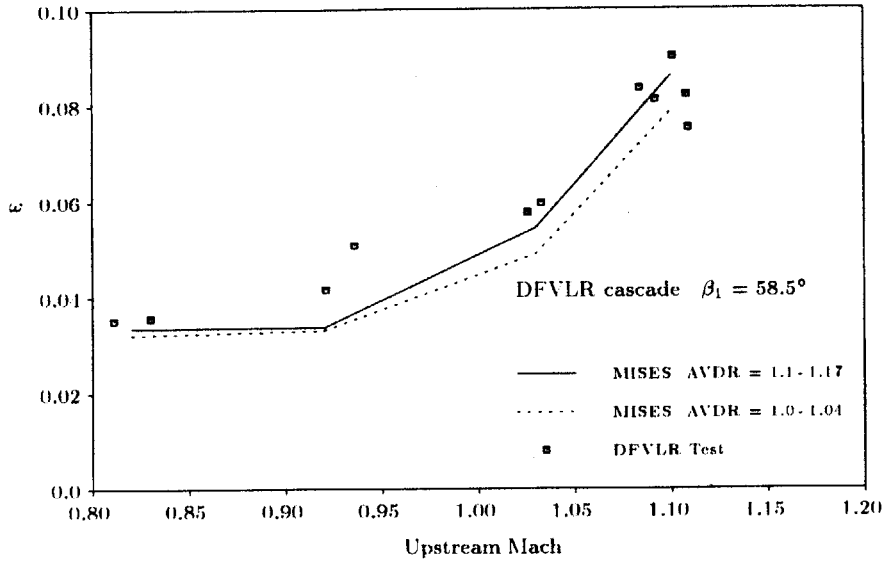

Figure 4.9: Comparison of predicted and measured loss for DFVLR cascade

AVDR = 1.10 – 1.17 are relatively small and the predicted losses are in generally good agreement with tested losses. The lower loss levels predicted for $M = 0.92$ are consistent with the differences in the upper surface supersonic region observed in the pressure comparisons.

4.3.5 Additional Supersonic Test Cases

Data for two additional supersonic operating points from Reference [18] are compared to MISES results in Figure 4.10 and 4.12 for upstream Mach numbers of 1.023 and 1.086, respectively. For these cases the exit pressures were specified, although again only far-upstream inlet conditions were given. Like the previous supersonic cases, a DOF was used to match the far-upstream mass flow.

The $M = 1.023$ case was run at a low inlet angle $\beta_1 = 56.8°$, near the spill point

for the cascade, with an AVDR = 1.092. The pressure ratio was set from the test conditions. The pressure data comparison is shown in Figure 4.10, with Mach contours in Figure 4.11. Considering the match in the pressure data, the difference between the MISES and experimental loss levels is surprising.

The $M = 1.086$ case was run at inlet angle $\beta_1 = 58.5°$, much closer to the design angle for the blade, and at a high AVDR = 1.184. The pressure ratio was adjusted upward +0.04 from the test conditions to match the trailing edge and lower surface pressures. The pressures are compared in Figure 4.12 and the Mach contours are shown in Figure 4.13. MISES again under-predicted the loss, this time by 0.0252.

Considering the excellent match in surface pressures, and the previous favorable match in losses for the AVDR comparison, the magnitude of the mismatch in loss levels is surprising. It is especially puzzling considering the typical mismatch between ISES results and tested drag levels is less than ± 0.0010[1] for transonic airfoils with similar upper surface Mach numbers to this cascade. The differences in loss may result from the simplistic modeling of of the sidewall contraction. The sidewall boundary layers are actually subject to different flow conditions on each side of the blade. Although a simple blockage correction using the total sidewall BL thickness to set AVDR is adequate for subsonic flow, it cannot represent the physics as the flow becomes sonic and the local sensitivity of the flow to blockage effects increases. At this point separate blockage effects are required for upper and lower surfaces.

The sidewall boundary layers also strongly influence the apparent thickness of the mid-span boundary layer in a two-dimensional test. The mechanism for this is simply continuity, changing the boundary layer thickness as a result of the local effective sidewall contraction downstream of the blade. Since the drag (or loss) is typically measured by a survey of the wake boundary layer at the mid-span of the tested blade, the locally increased thickness can indicate falsely high losses. Overall, the best approach for transonic or supersonic testing is to eliminate the sidewall boundary layer completely through sidewall suction over the blade.

[1] For carefully conducted tunnel tests, such as the AGARD RAE 2822 series.

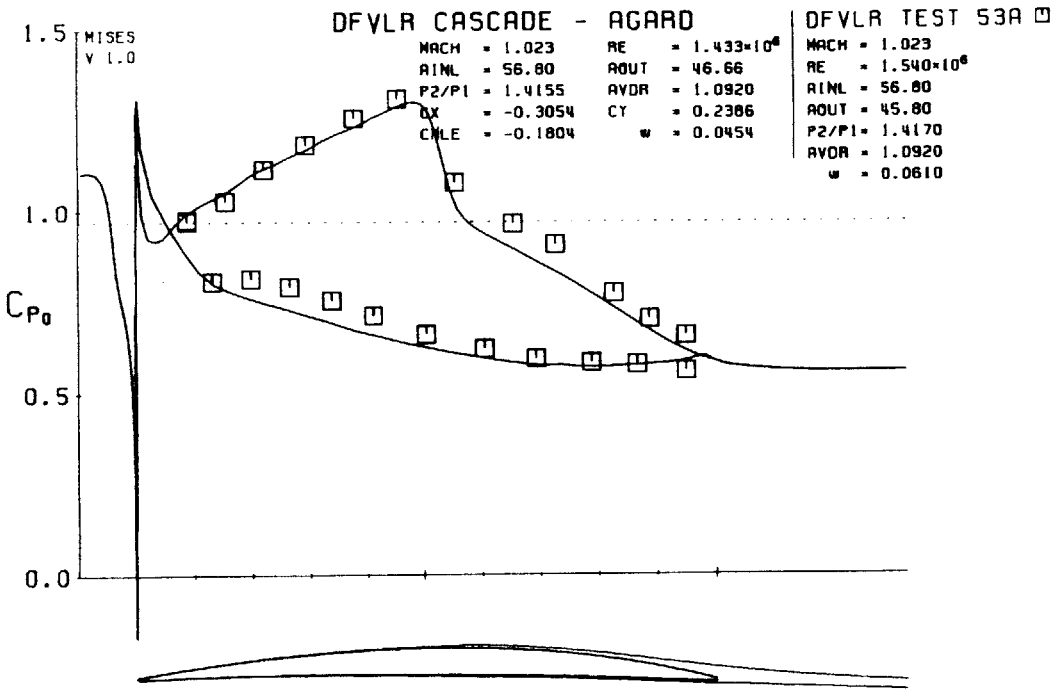

Figure 4.10: DFVLR blade: $M = 1.023$, $\beta_1 = 56.8°$, AVDR $= 1.092$

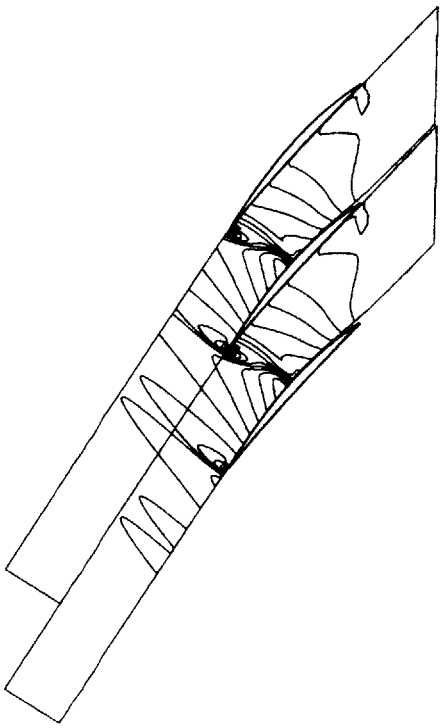

Figure 4.11: Mach contours for DFVLR blade, $M = 1.023$, contour interval 0.05

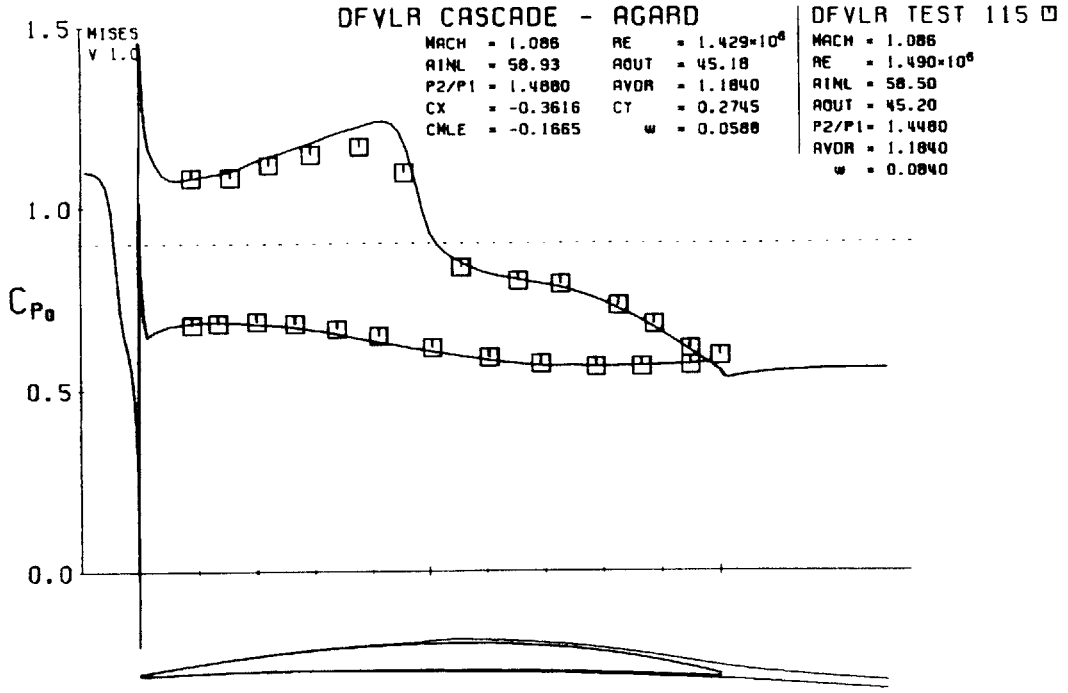

Figure 4.12: DFVLR blade: $M = 1.086$, $\beta_1 = 58.5°$, AVDR = 1.184

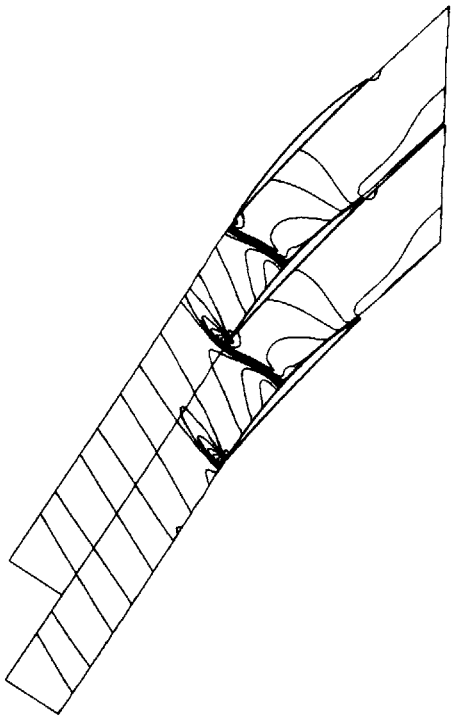

Figure 4.13: Mach contours for DFVLR blade, $M = 1.086$, contour interval 0.05

4.4 ARL Supersonic Cascade

This case analyzes the flow in a two-dimensional high turning supersonic compressor cascade with splitter vane at an inlet Mach number of 1.46. This cascade was designed to achieve high turning by high streamtube contraction from inlet to exit (a metal-metal AVDR = 2.053!). The blade and splitter vane sections are shown in Figure 4.14 with the splitter at the nominal 50% circumferential position.

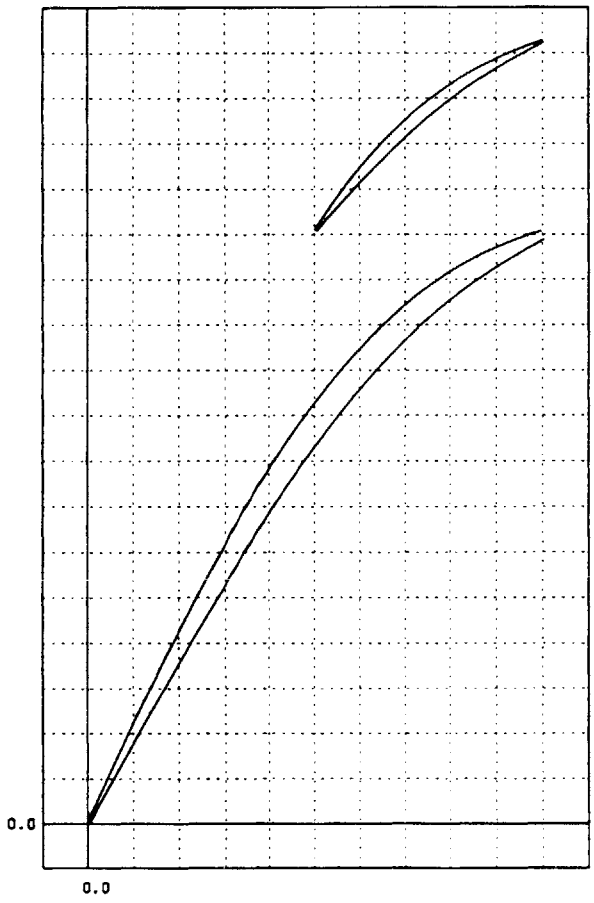

Figure 4.14: Blade and splitter vane for ARL cascade

Comparison data was obtained from References [2, 3, 5]. This data included turning and loss data at $M = 1.46$ for a range of pressure ratios, both with and without the splitter vane. Surface pressure data was measured for the main blade and splitter[2].

[2]Unfortunately only 5 taps were used to measure splitter pressures.

The blade definition was obtained from Reference [5], using circular leading edges on both main blade and splitter. The main blade and splitter thickness/chord ratios were 3.61% and 4.5%, with thick trailing edges, 1.964% and 1.021% respectively. As a result of problems early in the MISES development, a slightly elliptical leading edge was used for the main blade to reduce expansions at the leading edge. These problems were later corrected so that circular leading edges may be used, but the comparisons that follow use the modified blade profile.

4.4.1 Test Flow Conditions

Flow conditions for the ARL tests were carefully set up and thoroughly documented, simplifying the comparison of computational results to experiment. An upstream wedge was used to establish periodic flow in the cascade and inflow conditions were measured in the periodic flow field. A cross-section view of the test section, showing the blade row between the strongly contracted side walls is shown in Figure 4.15. Suction was used to remove sidewall boundary layers immediately upstream of the contraction. The blade aspect ratio was approximately 1:1, resulting from structural limitations on the blading. The two-dimensionality of the flow over such a low aspect ratio blade is questionable.

The inlet flow conditions were an inlet Mach number of 1.46, $\beta_1 = 66.84°$, and an inlet Reynolds number of 1.45×10^6. Turbulent flow conditions were assumed, with transition at 2% chord for all surfaces.

Measured data from the test was obtained by flow survey at 27% of axial chord downstream of the trailing edge. Mass-averaged *near-field*[3] exit data for exit pressure, angle, loss and other flow properties were generated from this data. A mixing loss analysis of the mass-averaged data was used to generate *far-field* exit data.

[3]My terminology, *near-field* refers to mass-averaged exit data from the flow survey, *far-field* refers to mixed-out exit data

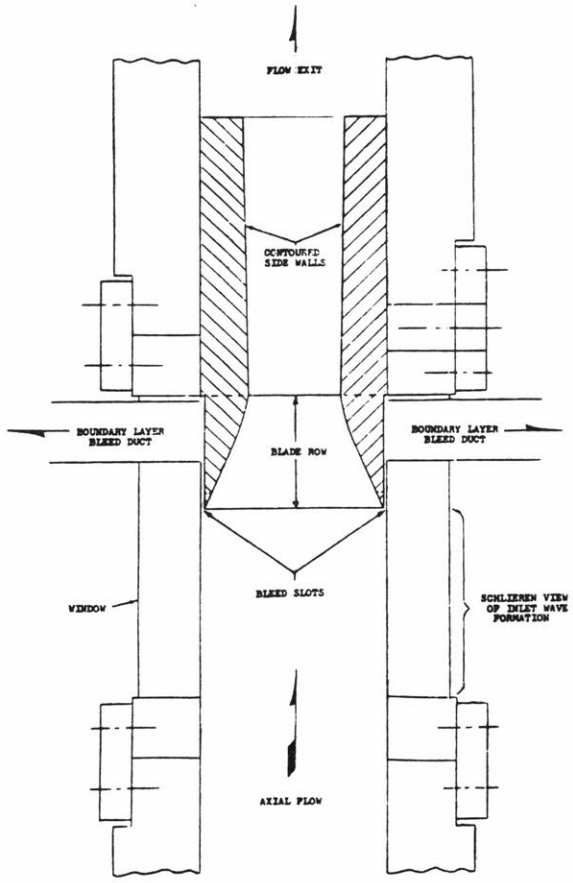

Figure 4.15: Top view of ARL test section showing sidewall contraction

4.4.2 Computational Model

Due to the high inlet angle $\beta_1 = 67°$ which accentuates skew problems for standard grids, an offset-periodic grid was used to model the ARL cascade. Most of the MISES results were obtained using a 220x20 computational grid with 2 offset blocks in the inlet region, see Figure 4.16. This grid is from a converged solution, showing large blockage effects from separated boundary layers on the main blade and splitter vane. Grids with densities from 180x16 to 240x32 were used with essentially identical results - within 2-3% of loss and turning.

The metal-metal streamtube width for this case is shown in Figure 4.17, corresponding to AVDR = 2.053. Also shown is the reduced streamtube width corresponding to AVDR = 2.242, or 109% of the metal-metal AVDR, used for much of the comparisons.

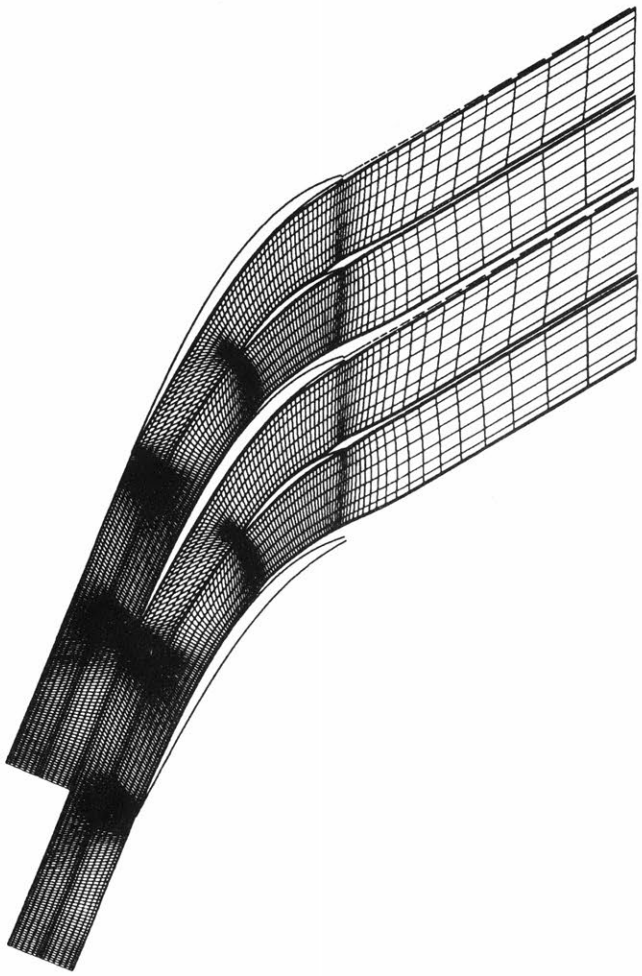

Figure 4.16: Offset-periodic 220x20 grid for ARL cases

The boundary conditions used for MISES specified exit pressure and applied an extra DOF using c_{inl} to drive the inlet Mach number to 1.46. An isentropic region was used from behind the leading edge bow shock through the leading edge expansion to minimize spurious losses due to dissipation in the near-surface streamlines.

4.4.3 AVDR Effects

As discussed in Section 4.1 AVDR has a strong effect on exit angle and loss for cascades. These effects are shown in Figures 4.18 and 4.19 for the ARL cascade with 50% splitter vane position and a static pressure ratio $p_2/p_1 = 1.93$. The intent of this comparison was to choose an AVDR that best matched exit angles in the test data. Unfortunately

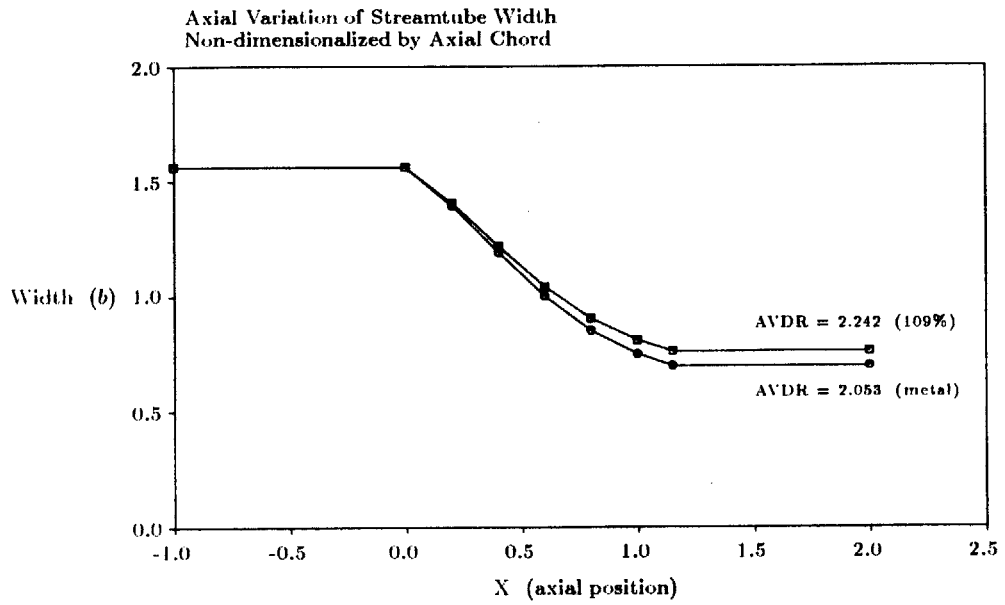

Figure 4.17: Streamtube width for ARL cascade at metal-metal and 109% AVDR.

a single AVDR value did not match the observed variation of far-field exit angles, in the range 28° – 31°. Rather than chase the 'correct' AVDR for each pressure ratio, a compromise AVDR of 2.242 (109%) was chosen as a best fit at pressure ratios of 1.8-1.9, and was used for further comparisons and design studies. The sidewall profile for the modified AVDR was obtained by scaling the streamtube thickness about the inlet value. This is not justifiable on the basis of using the viscous blockage, i.e. boundary layer thickness, to modify the AVDR. The issue of the 'real' blockage effects is considerably more complex and may invalidate the quasi-3D flow assumptions. This will be discussed further in the next section.

Pressure distributions for the two extremes are shown – for low AVDR, in Figure 4.20, and for high AVDR, in Figure 4.21. These show that the splitter loading increases at low AVDR from the locally increased incidence at the splitter due to separation on the main blade. Note that the pressure levels on the lower surface of the main blade are strongly affected by the AVDR.

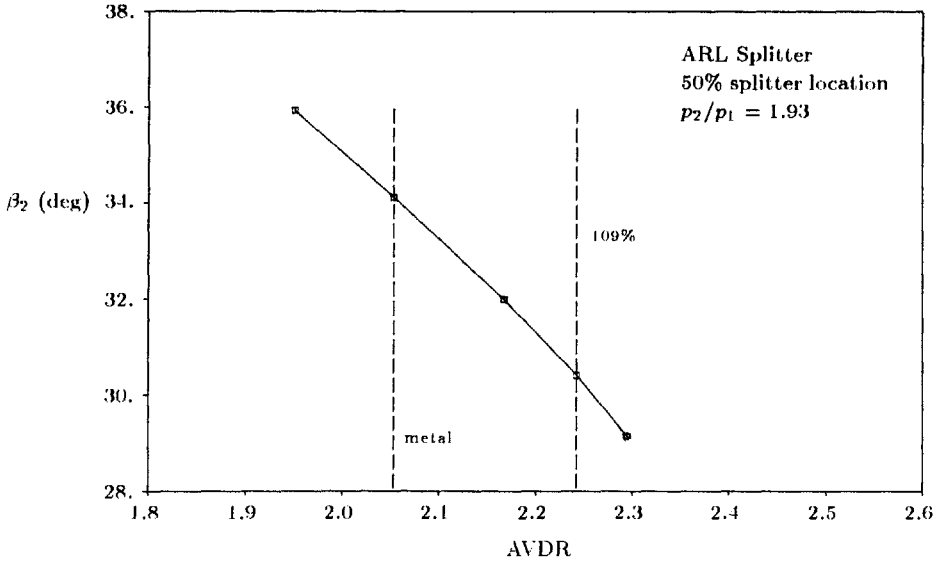

Figure 4.18: Effect of AVDR on exit angle for ARL cascade

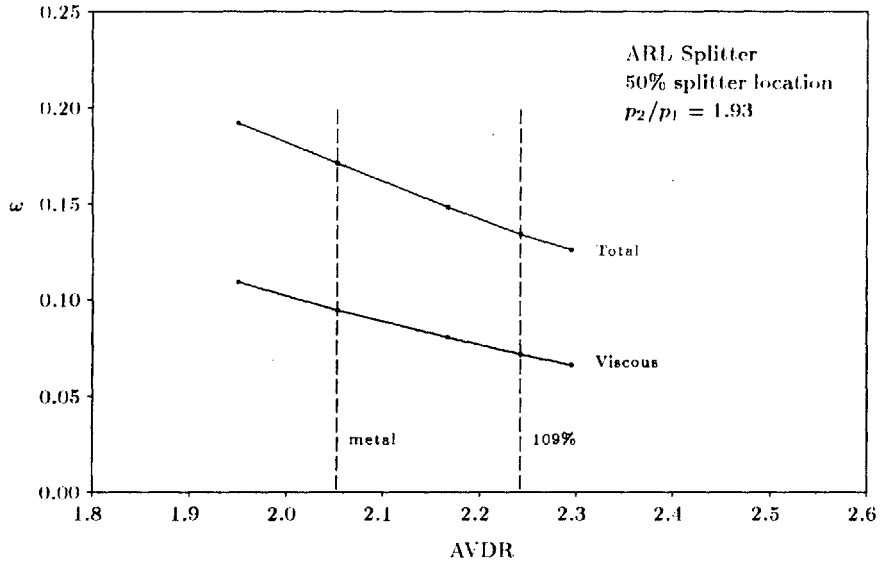

Figure 4.19: Effect of AVDR on total and viscous loss for ARL cascade

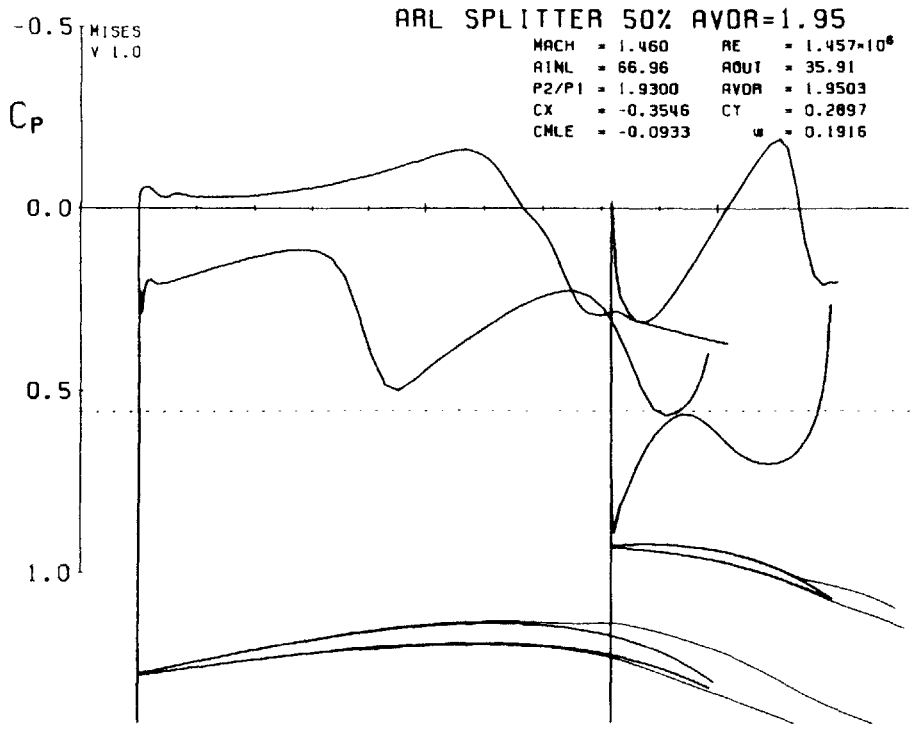

Figure 4.20: Pressure distribution for AVDR = 1.95.

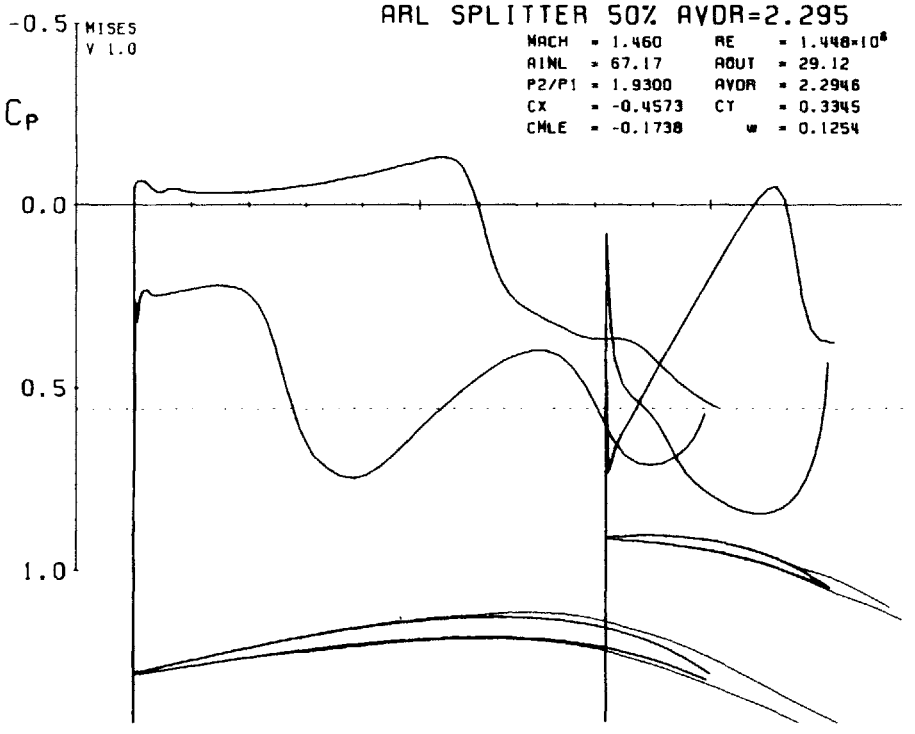

Figure 4.21: Pressure distribution for AVDR = 2.295.

4.4.4 Pressure Comparison

The difficulty in comparing pressure data for supersonic cascades lies in determining the features that should be matched using the available parameters. Since MISES results show strong curvature of exit streamlines immediately behind the blade, see Figure 4.16, exit angles from MISES were compared to the experimental far-field exit angle rather than the near-field angle. Exit angles in MISES were measured at the exit boundary one axial chord downstream and represent almost completely mixed-out values. For the ARL case, AVDR was adjusted to 109% of the metal-metal AVDR to roughly match exit angle with the far-field exit angle from the test. This corresponds to reducing the streamtube width by approximately *one-half* of the boundary layer thickness at the trailing edge. Since the sidewall boundary layers and blade boundary layers must be roughly comparable in thickness, this correction is certainly not excessive. In addition, the assumed profile for streamtube width does not take into account the actual axial variation of the sidewall boundary layer thickness.

The static pressure ratio for MISES that best matched surface pressures at the trailing edge and splitter lower surface turned out to be the same as the far-field static pressure ratio from the test. This indicates that the mixed-out flow quantities are more appropriate candidates for comparison than the near-field data. Results for static pressure ratio $p_2/p_1 = 2.034$ are shown in Figure 4.22, displaying excellent agreement to test data from Reference [5]. The near-field pressure ratio in the test was $p_2/p_1 = 2.011$. Mach contours for this flow condition are shown in the companion Figure 4.23.

Results for static pressure ratio $p_2/p_1 = 1.741$ are shown in Figure 4.24. The agreement on the splitter is good, showing a strengthening of the upper passage shock. The results for the main blade show considerable mismatch on the lower surface from mid-blade to the trailing edge. The measured near-field static pressure ratio for this case was $p_2/p_1 = 1.592$. Mach contours, in Figure 4.25, show passage shocks above and below the splitter vane.

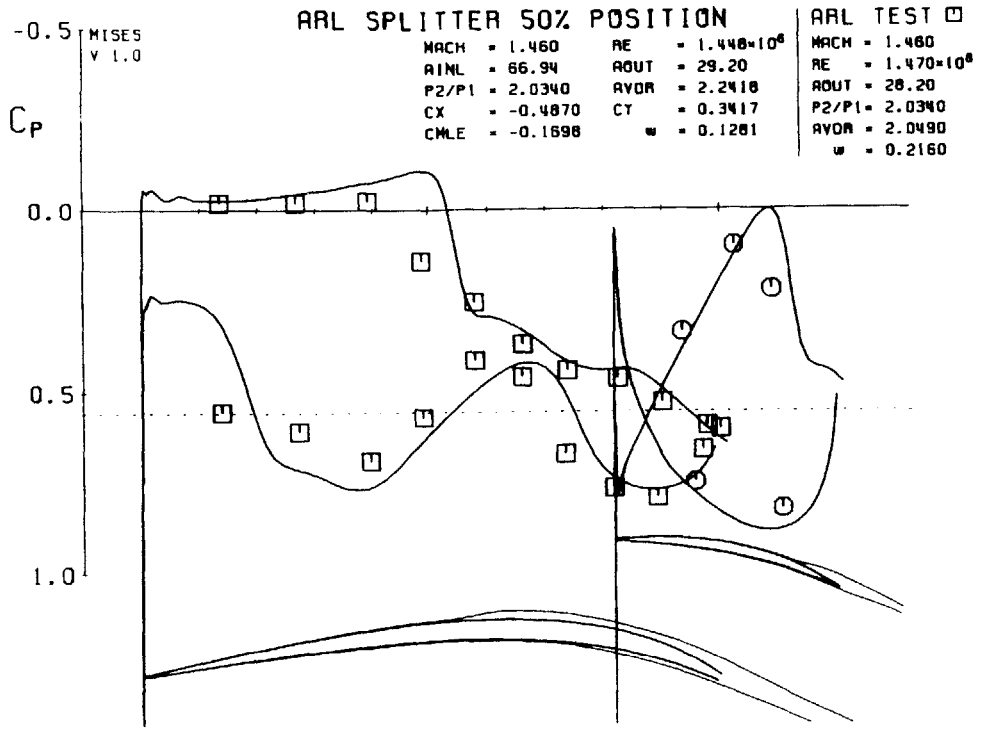

Figure 4.22: Surface pressures for ARL with splitter, $p_2/p_1 = 2.034$, 109% AVDR.

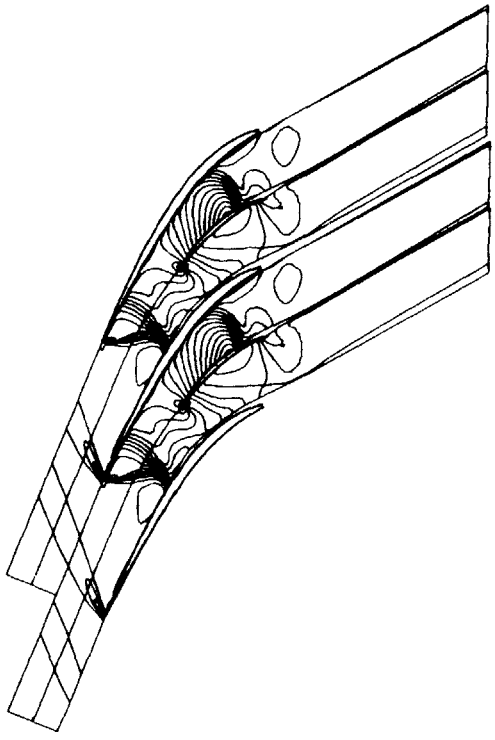

Figure 4.23: Mach contours for ARL cascade, contour interval 0.05, $p_2/p_1 = 2.034$

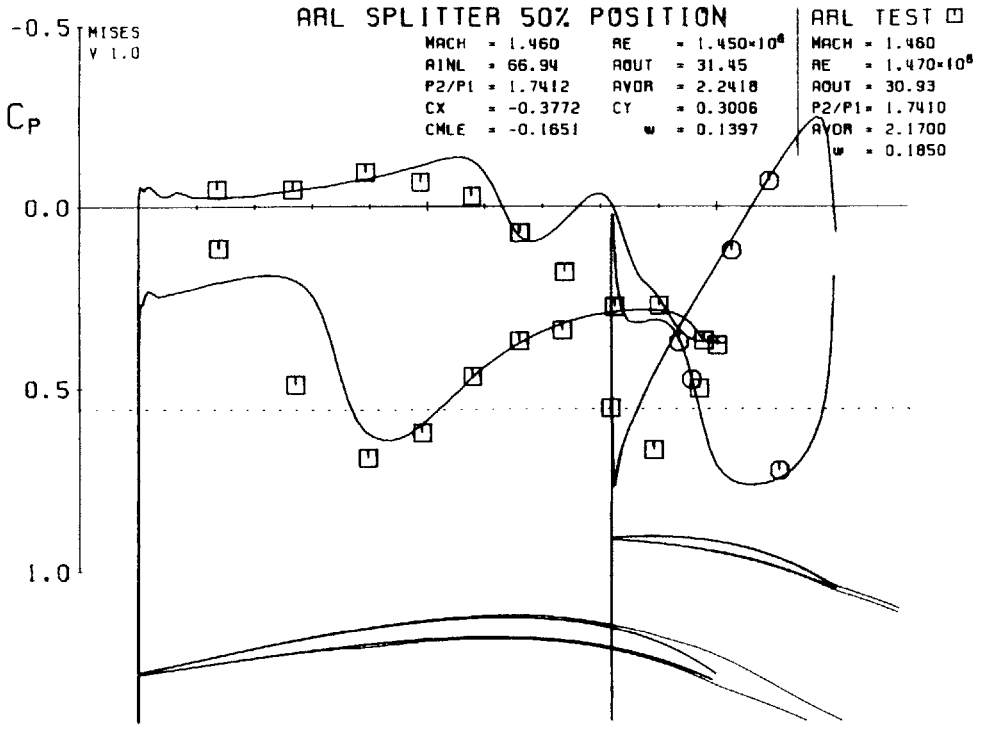

Figure 4.24: Surface pressures for ARL blades, $p_2/p_1 = 1.741$, 109% AVDR.

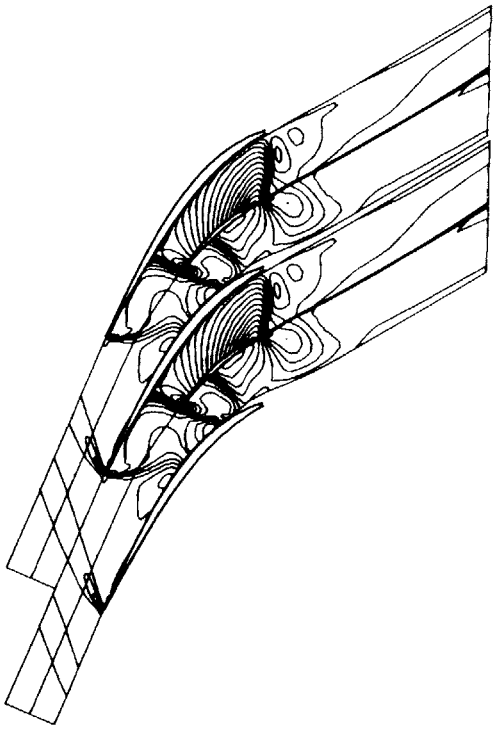

Figure 4.25: Mach contours for ARL cascade, contour interval 0.05, $p_2/p_1 = 1.741$

The effect of static pressure ratio on exit angle is shown in Figure 4.26. Computational results for exit angle are more nearly matched to far-field exit angles (no surprise here) and show a similar trend with pressure ratio. The effect of static pressure ratio on loss is summarized in Figure 4.27 showing that the computed loss levels were 25-40% lower than measured far-field loss. The computed and test results also show different trends with exit pressure, with the test data indicating decreasing losses at lower pressure ratios, a somewhat unexpected result.

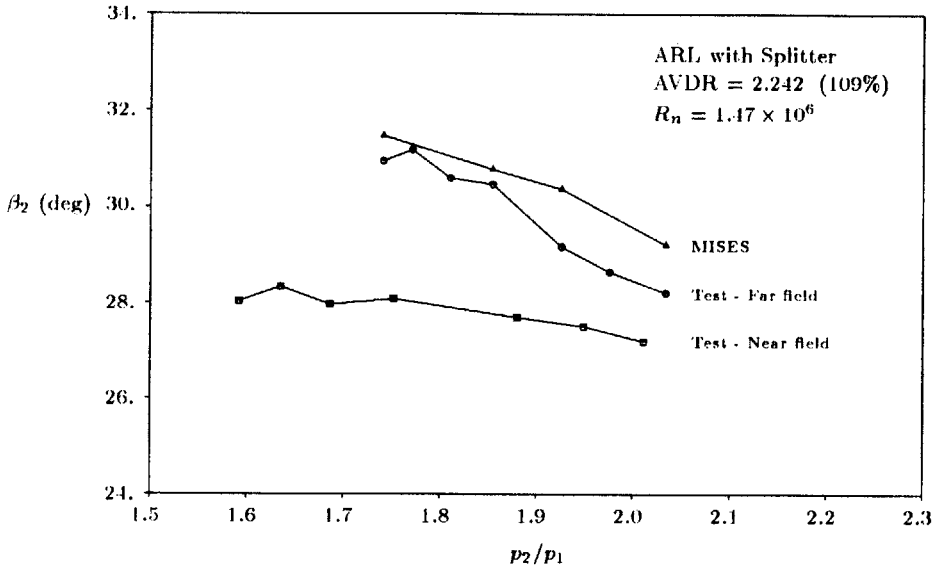

Figure 4.26: Effect of pressure ratio on exit angle for ARL cascade 109% AVDR.

The comparison of MISES results and test data shows that there may be additional factors at work not accounted for in the analytical modeling or the experimental measurements. The predicted and measured loss levels show an uncomfortably large mismatch and they show different trends with pressure ratio. The surface pressure comparisons showed an excellent match at $p_2/p_1 = 2.034$, yet the comparison at lower pressure ratio $p_2/p_1 = 1.741$ showed significant differences in the pressure distributions on the main blade lower surface near the trailing edge. Considering the boundary layer thickness variations and the sensitivity of loss and exit angle to AVDR it is not surprising that there are differences between these results, especially because of the simplistic modeling of cascade blockage with AVDR. For the analytical model AVDR was adjusted solely to match far-field exit angle which is largely insensitive to details in local blockage.

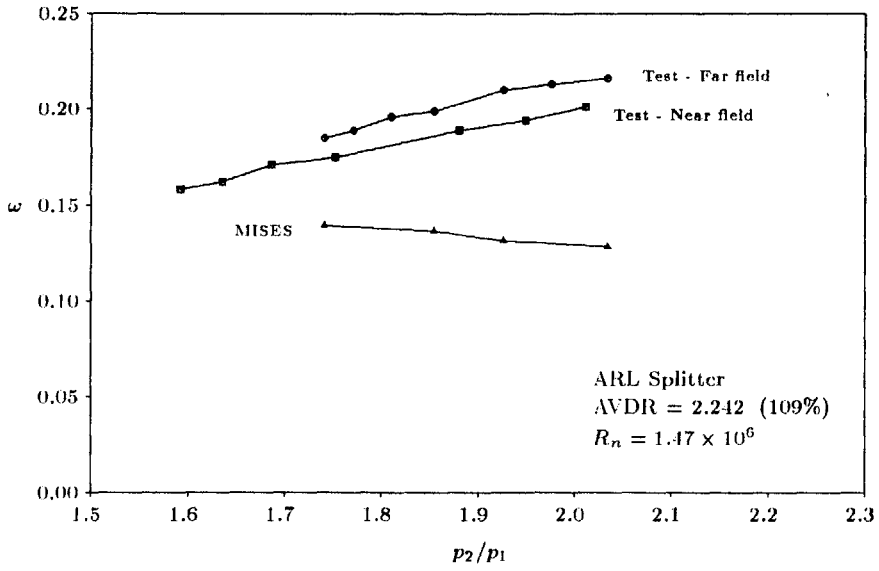

Figure 4.27: Effect of pressure ratio on loss for ARL cascade 109% AVDR.

Since the blade surface boundary layers have drastically different thicknesses and the sidewall BL thicknesses must be comparable to those on the blade, the actual blockage effects are very different for the upper and lower passages. The differences observed in surface pressures are likely to result from the local differences in sidewall blockage.

The losses measured in the tests may also be artificially high as a result of the nearly stagnant sidewall boundary layer fluid being driven by the blade-to-blade pressure gradient $-\nabla p$ into the suction surface boundary layer, thickening it and giving an incorrectly high loss. This flow mechanism is pictured in Figure 4.28, showing a view of the flow passage with paths for the inviscid and wall streamlines. One cannot assume that the upstream boundary layer bleed will eliminate sidewall boundary layer problems, since the separated blade and sidewall boundary layer thicknesses can reach 10% of the passage height.

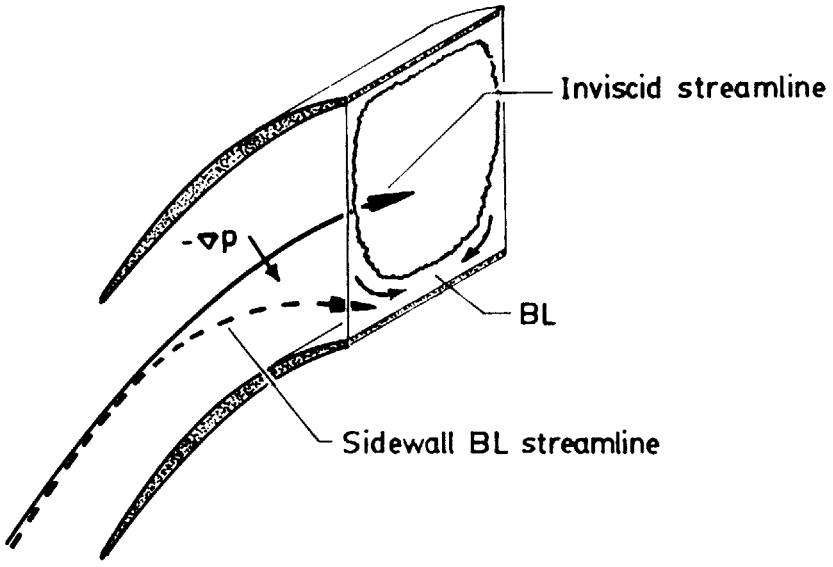

Figure 4.28: Thickening of blade boundary layer with sidewall boundary layer fluid.

4.5 Convergence of Newton Solution

The convergence of the Newton system is largely determined by the extent of strong compressible effects and viscous coupling, both of which become progressively more significant from the UTRC subsonic case to the supersonic ARL cascade with its strong viscous blockage effects. Convergence histories for the analysis test cases are shown in Figures 4.29 and 4.30. These figures show the maximum density change and loss level for each Newton cycle, and demonstrate the strong influence of Mach number on the convergence rate. It is characteristic of the Newton solution that the terminal rate of convergence to machine accuracy is roughly the same for all cases, but the non-linear cases spend many cycles moving non-linear residual errors around before getting to that point.

The maximum density change is normally used to indicate convergence for MISES, with a 10^{-2} drop as the threshold for engineering accuracy. Further convergence is recommended for parameter sensitivity analysis (e.g. loss sensitivity, see C.4), as functional gradients are inherently much noisier than the functions themselves.

The actual speed of the method depends on the time required for each Newton cycle, which is a function of the grid topology and density. For example, on a DEC DS5000 workstation (approx. 25MIPS, 4MFLOPS), the UTRC test case took 9 sec. per Newton cycle on a 132×20 standard grid, or 1 minute for a converged viscous solution. The ARL case took roughly 40 sec. per Newton cycle on a 220×20 offset-periodic grid, or roughly 20 minutes for a converged solution. By way of contrast with other methods, the ARL case was also run with UNSFLO [19], a time-marching Euler code with an embedded Navier-Stokes viscous layer. The case never fully converged, but required over 5000 iterations and many hours of computer time before the flow transients began to settle out.

Convergence from one flow condition to another, 'near-by' flow condition depends on the non-linear phenomena in the flow field. Typically, subsonic cases require only 3-4 Newton cycles to reconverge for near-by conditions, while 6-8 cycles were required

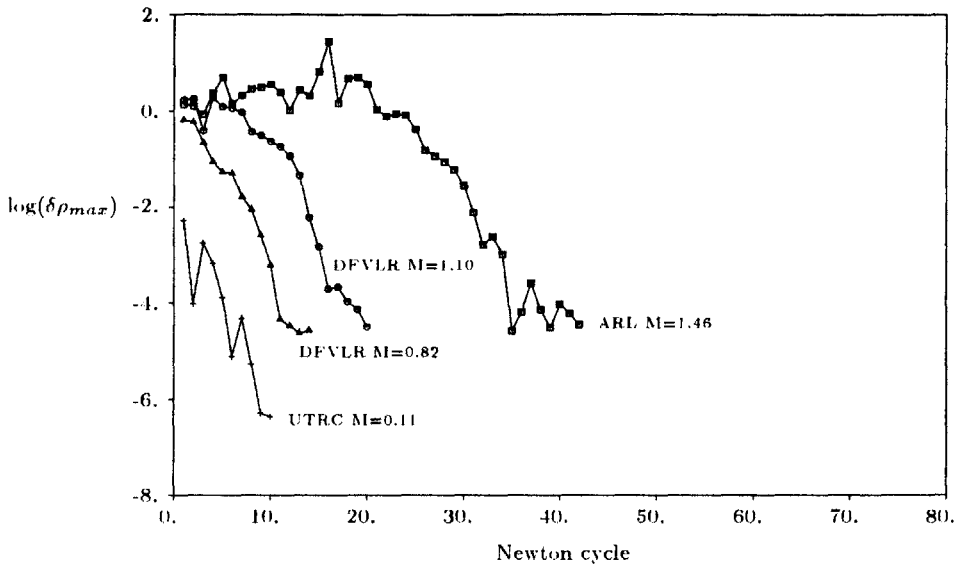

Figure 4.29: Convergence of Max density change for analysis cases

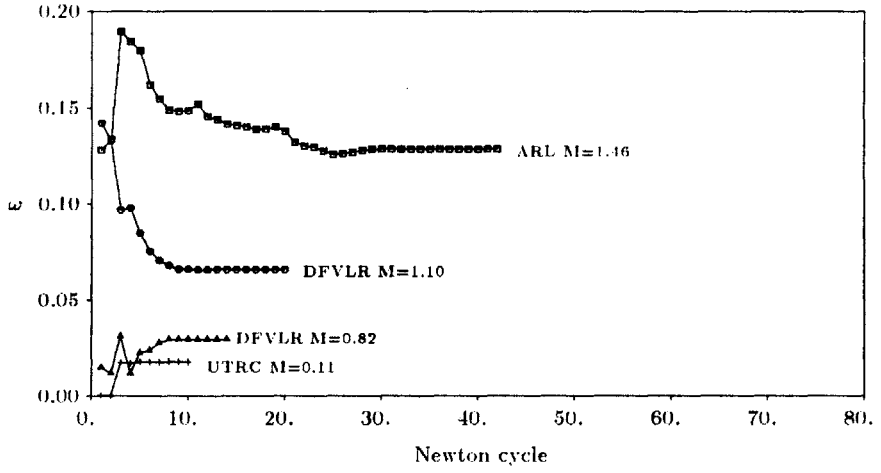

Figure 4.30: Convergence of loss for analysis cases

for the supersonic ARL case. Shock movement, or changes in the point of transition or separation slow convergence until the final position is attained. Note that small variations in specified flow conditions may not produce near-by solutions. Sometimes a particularly difficult flow condition must be approached through a succession of near-by solutions, or in extreme cases it may be necessary to reconverge a case from scratch.

The relatively large number of cycles to convergence for the ARL cases can be reduced by providing a better initial condition for the flow field. The 'standard' initial condition for cascades uses a smooth gradient of density along the passage specified by inlet conditions and exit pressure. Boundary layers are initialized to zero δ^*. A significantly better initial condition can be obtained by interpolating density and displacement thickness from a previous solution onto a new grid[4]. This reduces the number of cycles to convergence from $\sim$ 32 to 10, as shown in Figure 4.31.

The best convergence for the ARL case was obtained by specifying an exit pressure that produced a started condition, with the shock in the passage, but not so low as to strongly choke the splitter passages, typically $p_2/p_1 = 2.03$ was used. Normally, MISES will converge regardless, except when there may be no steady solution. Unstarted solutions for the ARL splitter at AVDR = 2.242 and $p_2/p_1 > 2.06$ never converged, suggesting that only unsteady solutions may exist for that state[5].

[4]The initialized displacement thickness probably has the more significant effect for the ARL case with its extensive separation.

[5]Although the nominal ARL cascade had no steady unstarted solution, several of the redesigned blades were found to have such solutions.

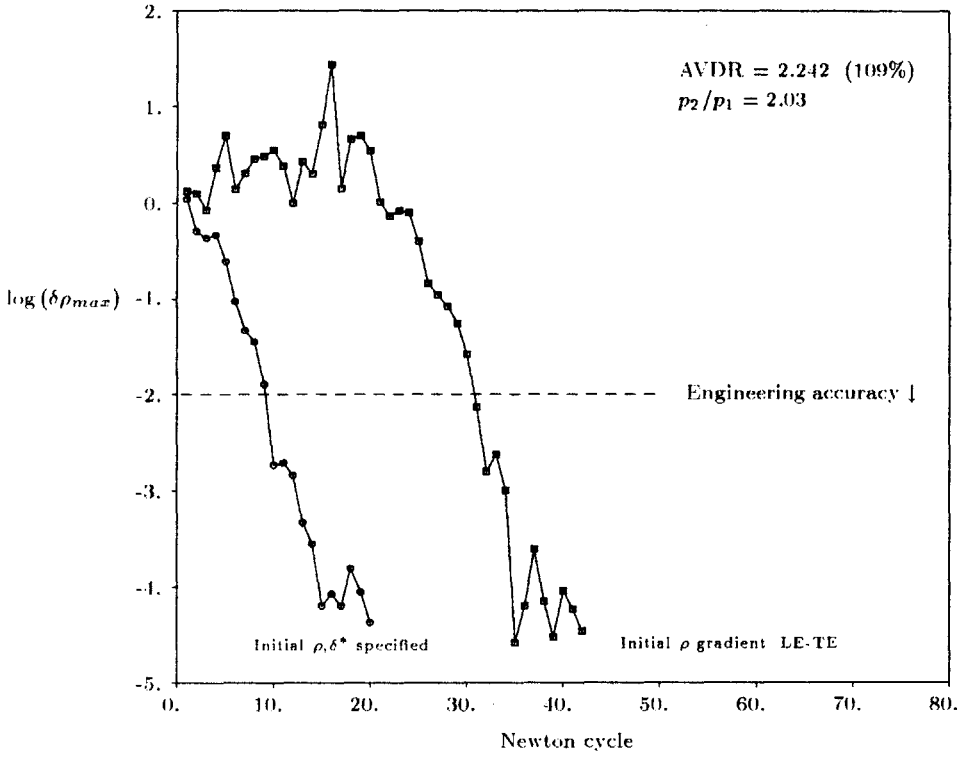

Figure 4.31: Convergence of Max density change for ARL Splitter with initialized flow field

Chapter 5
Results - Design Applications

The previous chapter compared analytical results with experimental data for several test cases, including the supersonic ARL cascade with splitter vane at its nominal 50% position. This chapter will focus on optimization of the ARL cascade with splitter vane. The principal objectives are

- Compare predictions for optimal splitter circumferential position with test data.
- Redesign main blade and splitter for improved performance.
- Examine design space for profitable directions for design changes.

5.1 ARL Cascade w/o Splitter

Before examining the splitter vane in detail, the performance of the basic ARL cascade without splitter vane was established. Essentially the same computational model developed for the ARL cascade in the previous chapter was used, with the splitter blade removed. The same inflow and boundary conditions were used.

Results at static pressure ratios of 1.93 and 2.03 are plotted with data from Reference [2] in Figures 5.1 and 5.2. The $p_2/p_1 = 1.93$ results are compared to test data at a near-field pressure ratio of 1.82. Corresponding pressures and forces for the cascade with splitter vane can be compared between Figure 5.11 and Figure 4.22 in the previous chapter. Analytical results indicate that the addition of the splitter increased turning by roughly 3° for a 30% increase in loss.

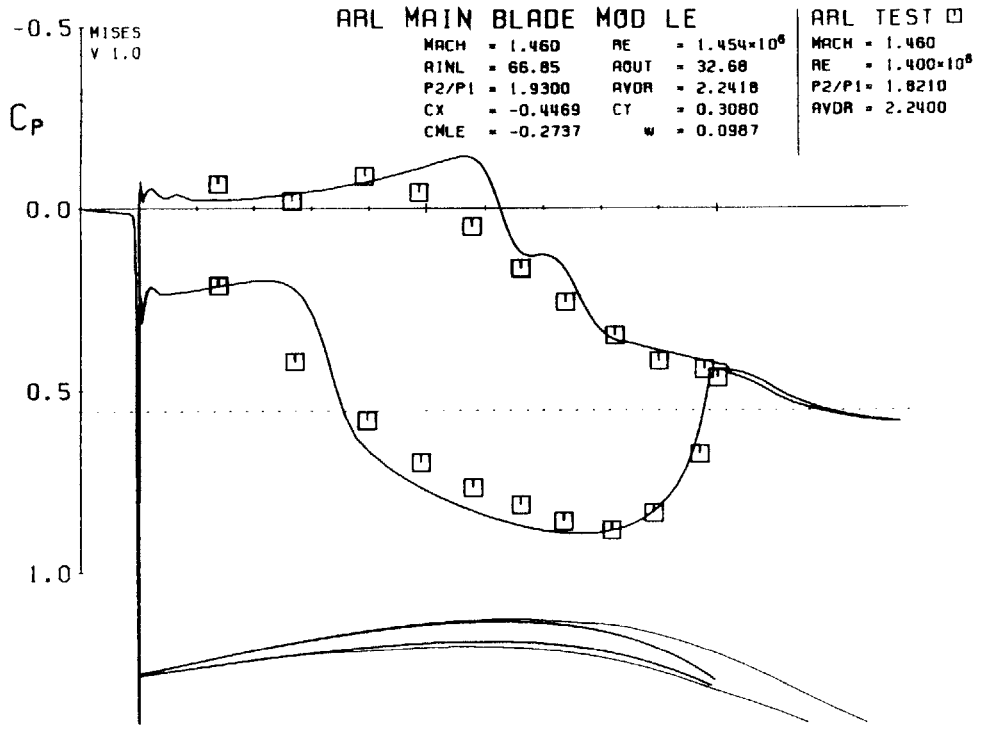

Figure 5.1: Pressure distribution for main blade at $p_2/p_1 = 1.93$, 109% AVDR

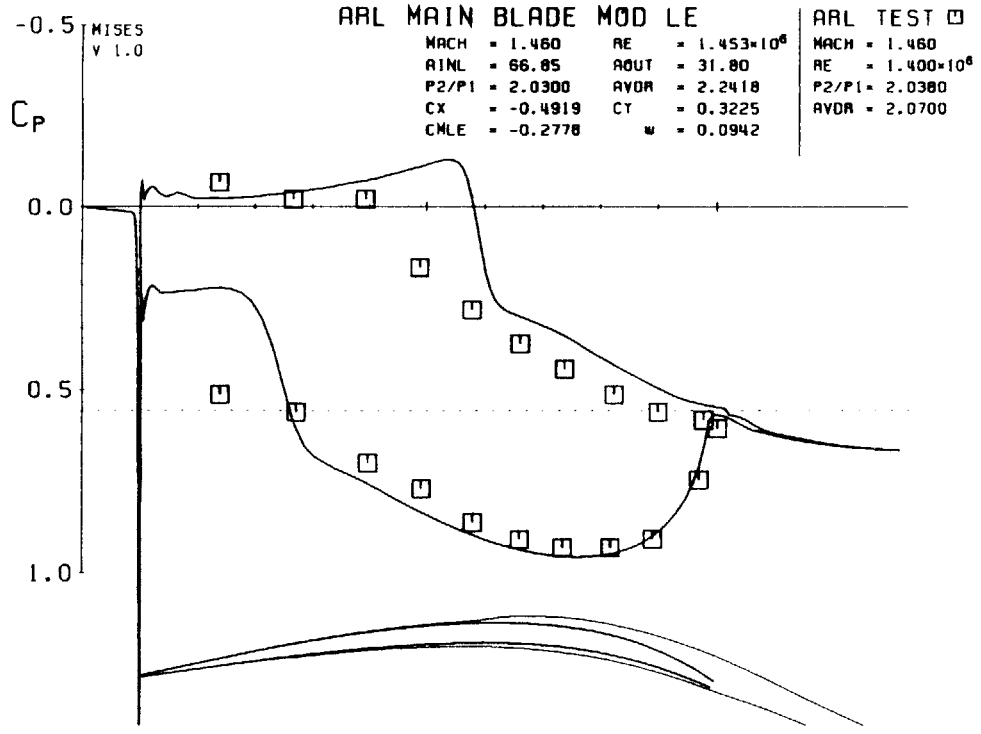

Figure 5.2: Pressure distribution for main blade at $p_2/p_1 = 2.03$, 109% AVDR

5.2 Splitter Vane - Background

The original splitter vane was added to the ARL cascade in an attempt to reduce deviation. It was designed to extend between 50% and 100% axial chord and used the mean camber line of the main blade in the overlap region. The vane thickness distribution corresponded to that of a circular-arc blade with the same inlet and exit angles and same maximum thickness as the main blade. The splitter thickness/chord ratio was 4.5%. The nominal position for the vane was midway between the main blades.

5.3 Splitter Vane Circumferential Position

The effects of splitter circumferential position were investigated using the computational model for the ARL cascade developed in the previous chapter. Data from an ARL experimental study [5] for splitter vane position was used for comparison of surface pressures, turning and loss. The splitter was displaced using the blade movement DOF D_{mov} and specified mode constraint discussed in Chapter 3. Other boundary conditions were identical to those used in section 4.4.2.

The effect of splitter circumferential position on loss is summarized in Figure 5.3 for splitter trailing edge positions from 44% to 56%. The computed loss levels were 20-30% lower than the measured near-field loss, and show no significant variation of loss levels with splitter position[1].

Pressure distributions for the 44% and 56% splitter positions are shown in Figure 5.4 and 5.5, compared to test data at 43% and 55% positions, respectively. The effect of upward movement of the vane was to increase splitter loading. The effect on the lower surface of the main blade was similar to the low pressure ratio comparison ($p_2/p_1 = 1.741$) in the previous chapter, where the MISES result indicates a strong acceleration forward of the trailing edge. Analytical results indicate that the load dis-

[1] This conclusion was also reflected in calculations of loss sensitivity to circumferential movement (see section C.4) where typical values of $d\omega/dD_{mov} = \pm 0.001/\%$ were obtained.

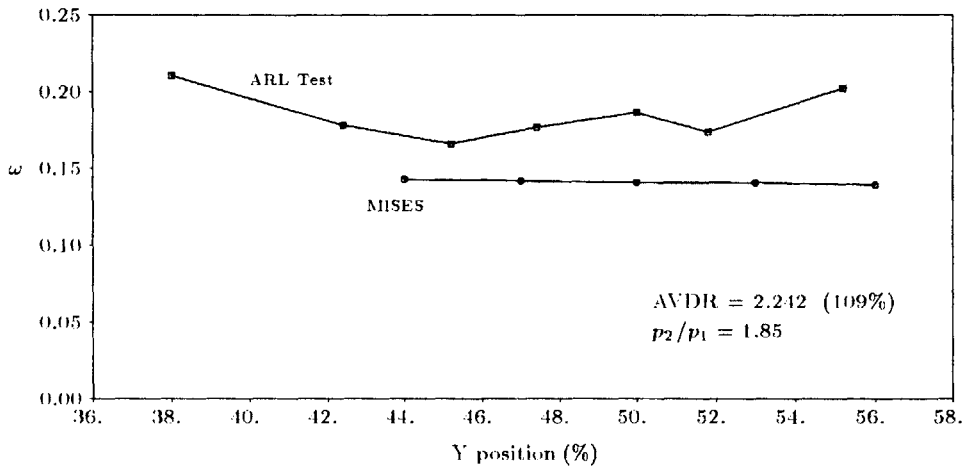

Figure 5.3: Effect of splitter vane circumferential position on loss

tribution between main blade and splitter is changed by splitter circumferential position, but the net loading and turning of the combination is unaffected. Given the strong sidewall influence, it is likely that the variation of ω in the test is due to sidewall boundary layer changes not modeled with the fixed AVDR assumption. The precise mechanism for the loss variation is not identifiable.

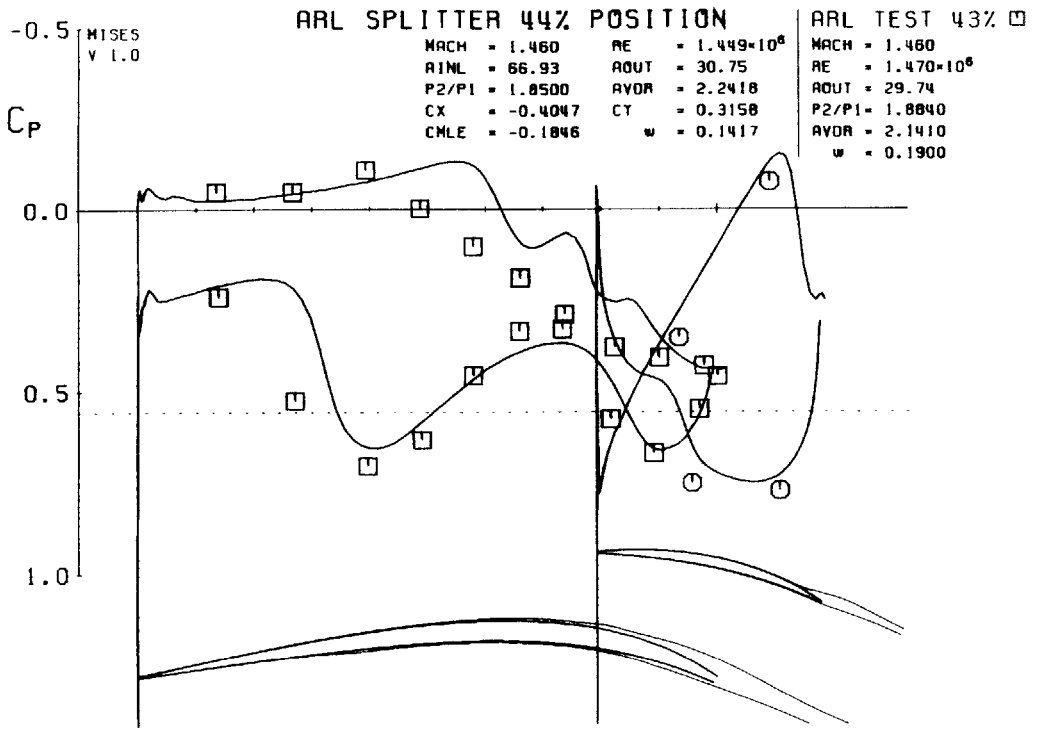

Figure 5.4: Pressure distribution for ARL cascade with 44% splitter position

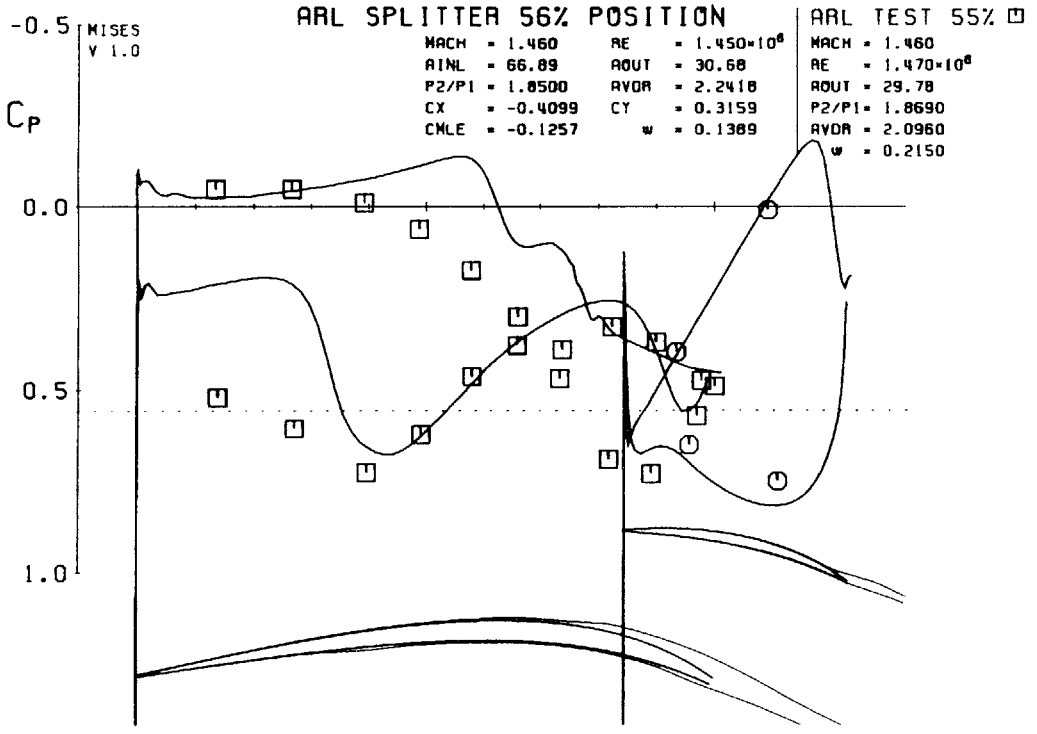

Figure 5.5: Pressure distribution for ARL cascade with 56% splitter position

5.4 Overview of ARL Cascade Flow Field

Before proceeding with changes to the blade geometry, we first review the problems we intend to cure by redesign. Analytical results have shown

- The flowfield is characterized by relatively mild forward passage shocks. The inviscid loss accounts for 30-60% of the total loss, depending on pressure ratio.
- The forward portion of the splitter is not loaded. The splitter leading edge near the sonic point, so that shocks are possible in either or both passages.
- The main blade pressure surface and the splitter upper surface form a supersonic nozzle terminated by a strong upper passage shock, usually with an associated separation region on the splitter.
- Strong separation is present on the main blade with subsequent reduced turning.

The goals for any optimization or redesign are generally to reduce losses and/or increase turning. The trade-off between loss and turning is not well defined here, and usually depends on details of the cascade application. Profitable directions for redesign of the ARL cascade, based on the flow features, appear to be

- Reduction of the strong acceleration in the upper passage to reduce shock strength and separation on the splitter.
- Shifting some of the splitter loading forward towards the leading edge.
- Reducing the strength of the main blade separation.

5.5 Modal Re-design of ARL Cascade

The splitter vane and main blade were redesigned using the modal design option discussed in Chapter 3. Modal design was selected because of the presence of separated flow on both main blade and splitter. Camber redesign was used to avoid thinning the already very thin blades.

The starting point was the ARL cascade with the original splitter at $p_2/p_1 = 1.93$ and 109% AVDR. A series of modal design steps was used, explicitly specifying modal changes while monitoring changes in loss, turning and loss sensitivity. Mode shapes called out in Table 5.5 correspond to those shown in Figure 3.6.

Iteration	Modes	Blade	Surface	Design region	Purpose
1	1, 3, 5	splitter	both	0-100%	decamber
2	D_{mov}	splitter	both		move down
3	D_{rot}	splitter	both		increase incidence
4	7	splitter	both	70-100%	add rear camber
5	1	main	lower	50-100%	fill out lower surface
6	7	main	both	75-100%	add rear camber

Table 5.1: Stepwise modal redesign of ARL cascade with splitter vane.

The intent in iteration 2 was to reduce the 'nozzle' effect in the upper passage. Step 5 pushed out the main blade lower surface to send compression waves onto the splitter suction surface to reduce the Mach number. Finally, iteration 6 added rear camber to the main blade to restore the turning to the original level. These changes could also have been accomplished using the inverse design mode, but the technique of explicit stepwise reshaping combined with loss sensitivity analysis gave more insight into the effects of each perturbation. The strong effect of turning on loss presents a problem for design guided by sensitivity analysis because a steepest descent down the loss sensitivity gradient in modal design space also tends to reduce turning. A more automated design

scheme should incorporate DOF's and constraints to evaluate sensitivity with turning held constant.

The blade shapes for the modified, MOD1C, cascade are compared to the original blades (dashed lines) in Figure 5.6. The pressure distribution for the modified cascade is

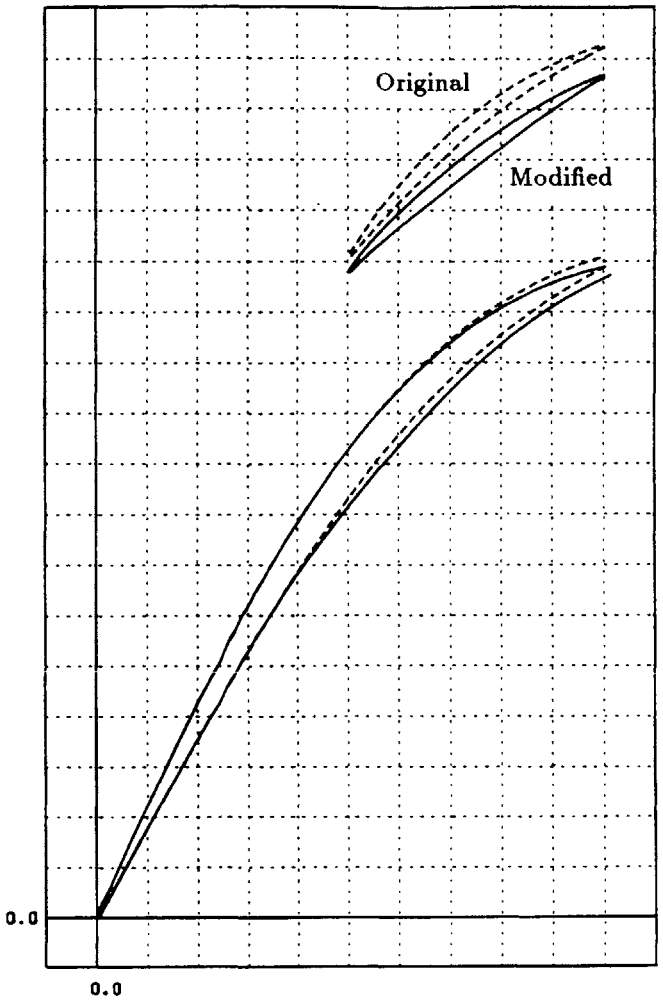

Figure 5.6: Redesigned blade section compared to original ARL blades.

shown in Figure 5.7. For comparison, the pressure distribution for the original blading is shown in Figure 5.10. The splitter loading has been moved forward, but loading on the main blade has decreased. The design changes resulted in 0.32° lower turning for a 2.7%

reduction in loss, a disappointingly small effect. The modified cascade was run for the range of pressure ratios 1.74–2.03 and demonstrated essentially identical performance to the original cascade as shown in Figure 4.27. This insensitivity to design changes is similar to that observed for turbulent flow airfoils where, so long as the flow remains attached and there are no strong compressible effects, the airfoil drag is basically fixed by the Reynolds number[2]. Since the transition was fixed for both blades in the ARL cascade, a similar effect may be operating for cascades. Still, considering the shock on the upper surface of the splitter, this degree of insensitivity is unexpected.

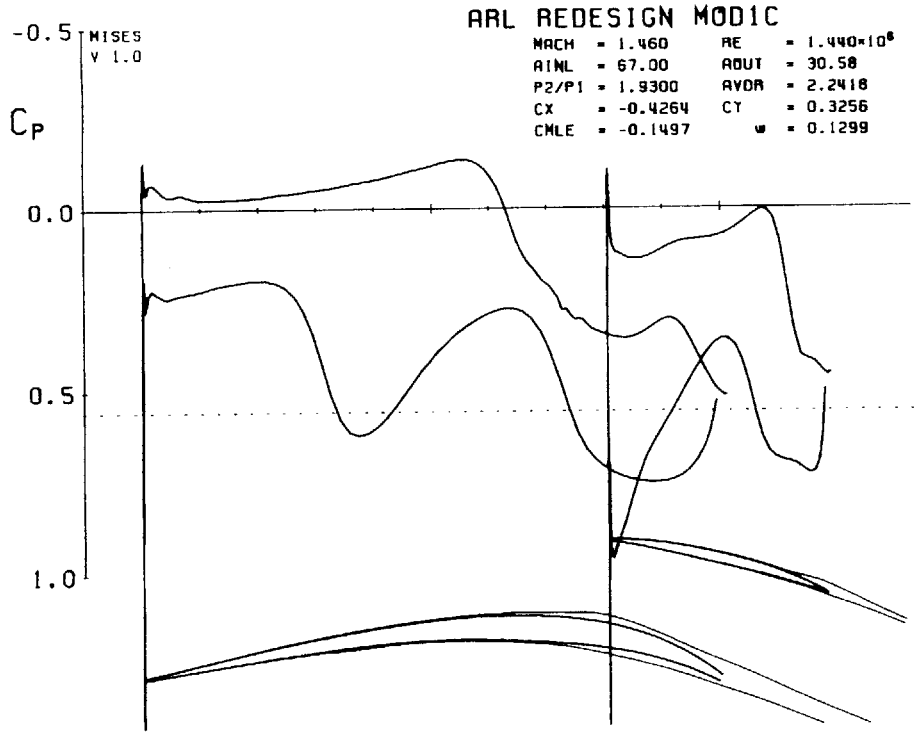

Figure 5.7: Surface pressures for redesigned ARL cascade at $p_2/p_1 = 1.93$

[2]The possibilities for optimization are expanded considerably for laminar flow airfoils, however.

5.6 Alternate Design Directions

The modal redesign resulted in little improvement in cascade performance. This, combined with the small effect of splitter circumferential position, implies that the design space should be explored in other directions. This section examines the effects of splitter rotation, splitter sizing and axial position on cascade performance.

5.6.1 Splitter Vane Rotation

The splitter position study showed that the circumferential position changed the relative loading of main and splitter blades, but had almost no effect on net turning and loss. The effect of splitter incidence on loading was investigated for a fixed splitter trailing edge position (50%). The splitter vane was rotated from $-3°$ to $+3°$ using the blade rotation DOF and fixed mode constraint. Computed pressure distributions for $p_2/p_1 = 1.93$ and 109% AVDR are compared in Figure 5.8. The loss and exit angles for splitter rotation are summarized in Table 5.2, showing an increase in both turning and loss for positive incidence on the splitter. Note that the $-3°$ rotation caused the lower passage to form a diverging nozzle with a mild shock on the splitter lower surface.

Incidence	ω	β_2
+3.0	0.1422	29.38°
0.0	0.1274	30.26°
−3.0	0.1300	30.58°

Table 5.2: Effect of splitter rotation, $p_2/p_1 = 1.93$, 109% AVDR.

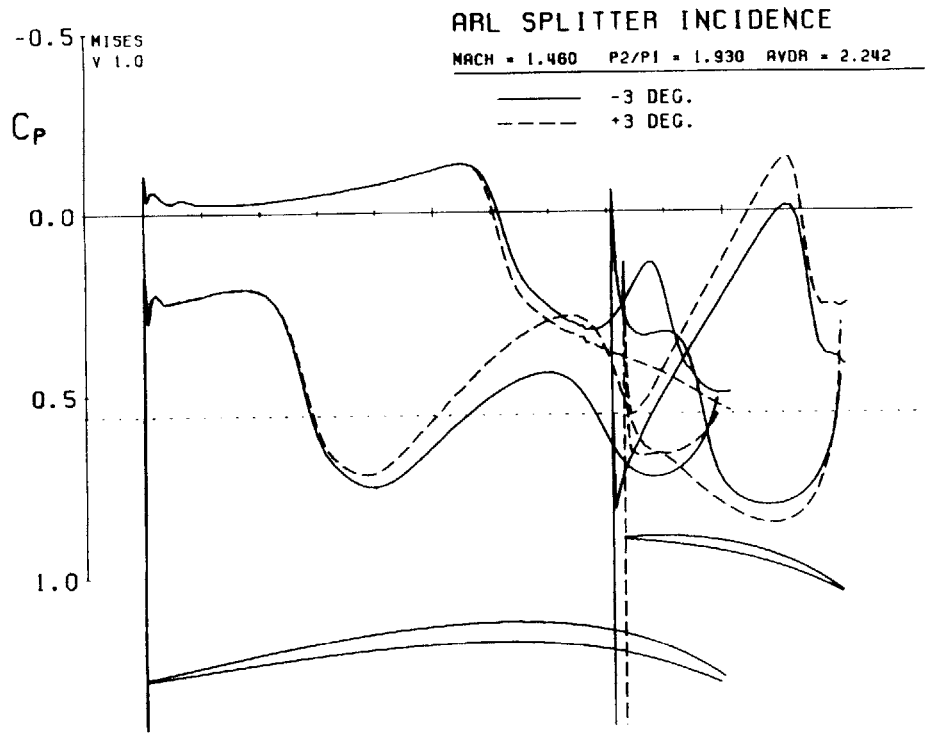

Figure 5.8: Surface pressures for ARL cascade at $\pm 3°$ splitter incidence

5.6.2 Short Chord Splitter Vane

The results for splitter position and rotation imply a strong interaction between main blade and splitter loading. Since the effect of the splitter is to cancel main blade loading in the overlap region, a shortened splitter was investigated as a means to increase loading on the main blade. The splitter was shortened to 70% of its chord with the same relative camber and trailing edge at the nominal (50%) position. The relative thickness was increased to maintain the same blockage as the original splitter. The pressure distributions for the original splitter and shortened splitter are compared in Figures 5.9 and 5.10. The shortened splitter gave basically the same performance as the original splitter — a slight decrease in turning for a slight decrease in loss (probably due to the reduced skin friction).

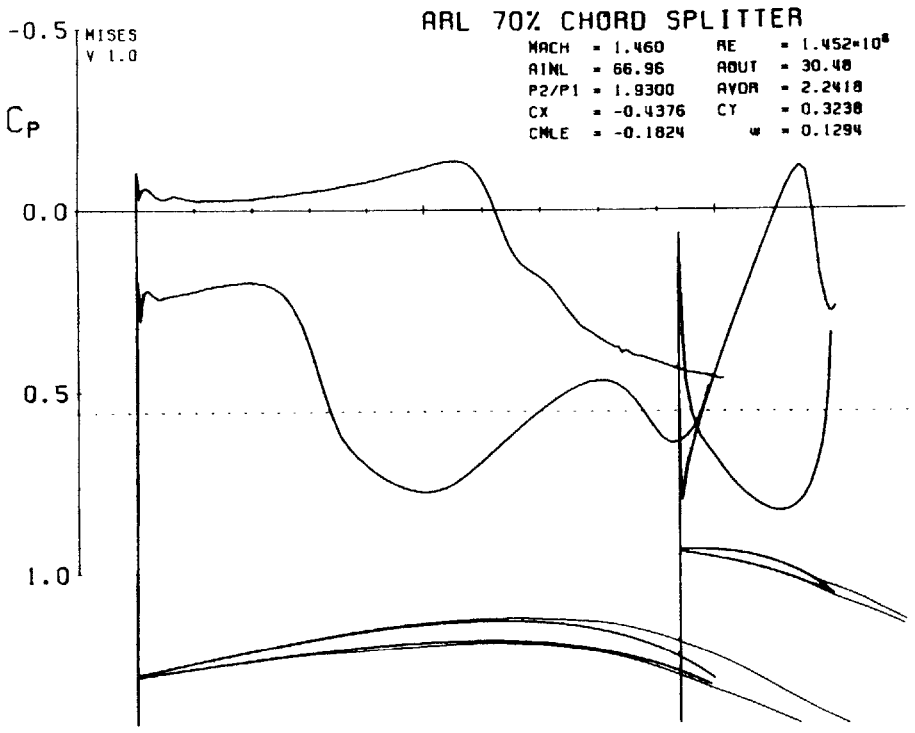

Figure 5.9: Surface pressures for shortened chord splitter at $p_2/p_1 = 1.93$

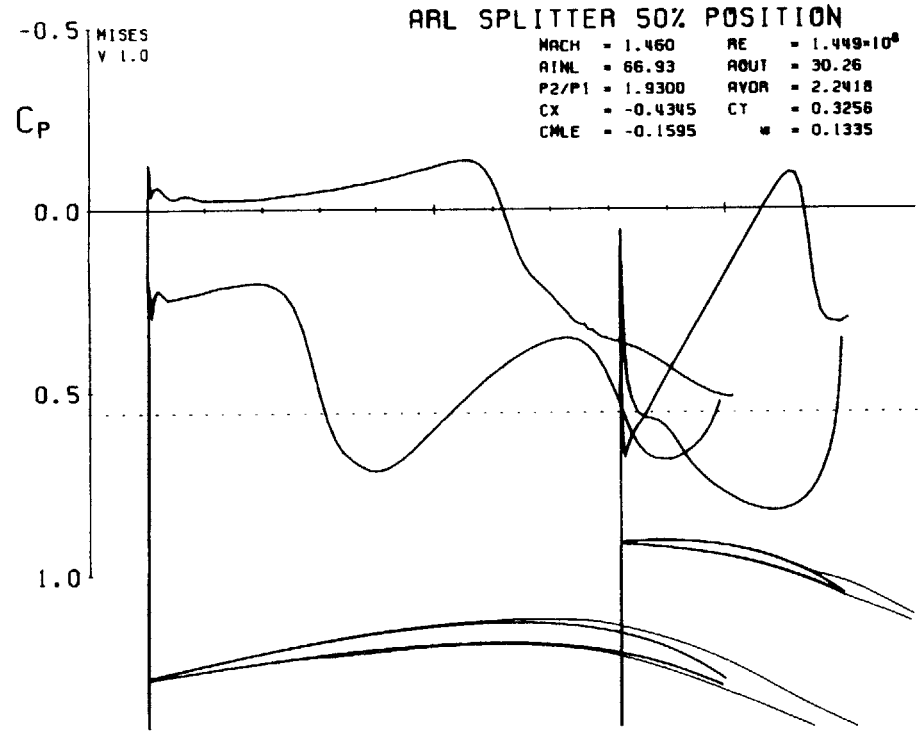

Figure 5.10: Surface pressures for original splitter at $p_2/p_1 = 1.93$

5.6.3 Splitter Vane Axial Position

Another means to reduce the interaction between the main blade and splitter is to stagger them axially by moving the whole splitter blade downstream. The original splitter vane was used, moved and rotated along a slight arc to maintain a position midway between the extended camber lines of the main blades. Since a strong effect on turning was found for the downstream positions, a higher static pressure ratio $p_2/p_1 = 2.03$ was used. Table 5.3 summarizes the effects of splitter axial movement, showing a large increase in turning ($+4°$) for a slight increase in loss levels. The higher turning

Axial TE Position	ω	β_2	vane incidence
1.00 (nominal)	0.1294	29.19°	0.0°
1.10	0.1274	28.66°	3.5°
1.15	0.1321	27.44°	5.2°
1.20	0.1347	25.18°	7.0°

Table 5.3: Effect of splitter axial position, $p_2/p_1 = 2.03$, 109% AVDR.

available at the most-downstream position increased the pressure ratio obtainable before unstarting from $p_2/p_1 = 2.06$ for the nominal position to $p_2/p_1 = 2.23$. The increased turning results from higher main blade loading, as shown in Figure 5.12. For comparison, Figure 5.11 shows the pressure distribution on the original cascade at $p_2/p_1 = 2.03$. Attempts to increase the turning further by redesigning the splitter for higher loading were unsuccessful – increased forward loading on the splitter simply reduced loading on the main blade at the expense of loss.

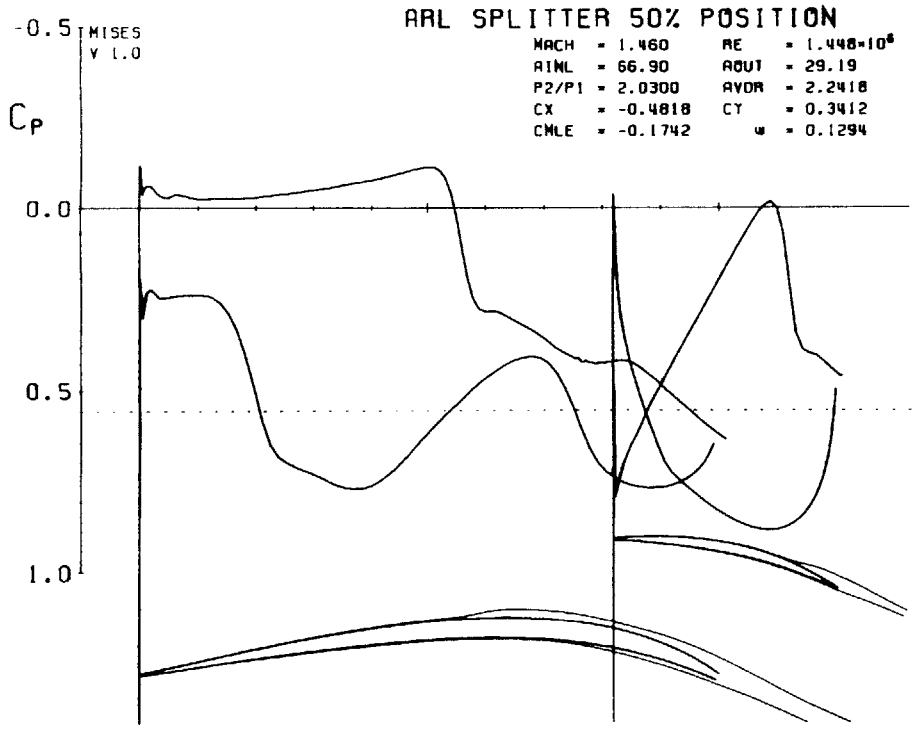

Figure 5.11: Surface pressures for ARL cascade at $p_2/p_1 = 2.03$

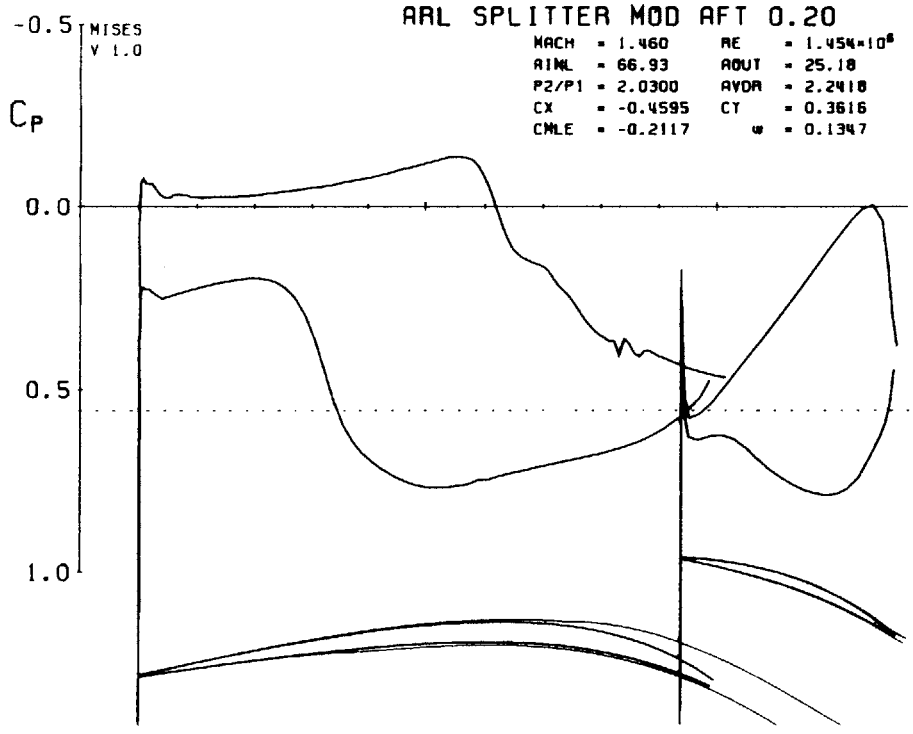

Figure 5.12: Surface pressures for ARL cascade with splitter moved +0.20 downstream

5.6.4 Tandem Splitter Vane

The high turning from the aft-most splitter position indicates that a different approach to splitter design may be required. The appropriate model for splitter design, if axial displacement is possible, may be to treat the splitter as the aft element of a multi-element airfoil. Multi-element airfoils achieve high lift without flow separation on the main element by reducing the trailing edge pressure with the suction from a smaller aft element. The second element can then be used to recover the flow to the trailing edge pressure because its boundary layer is thin.

A tandem configuration was defined using the 70% chord splitter moved aft by 0.35 and up by 0.35 toward the main blade pressure surface, and rotated by 13° to increase incidence to match the main blade camber. The tandem blading is compared to the original ARL splitter (dashed lines) in Figure 5.13. Some care was required to generate the grid for this configuration as a result of the proximity and overlap of the blades. Like the previous case, the tandem splitter was run at a higher static pressure ratio $p_2/p_1 = 2.23$ as a result of its higher turning.

The effect of the tandem configuration was surprisingly large – resulting in both dramatically increased turning (+12°) *and* a 15% reduction in loss. The improvement in turning is due to a higher main blade loading, as shown in Figure 5.14. Mach contours for this case are shown in Figure 5.15. The separated wake from the main blade 'bursts' as it encounters the pressure rise downstream of the splitter, apparently without any significant loss penalty. The pressure ratio at the unstart point was raised to $p_2/p_1 = 2.35$. Redesign changes made to the splitter to minimize the shock at the trailing edge resulted in surprisingly small, hard-won improvements to the loss and turning. Again, increased forward loading on the splitter acted to decrease aft loading on the main blade and reduce turning.

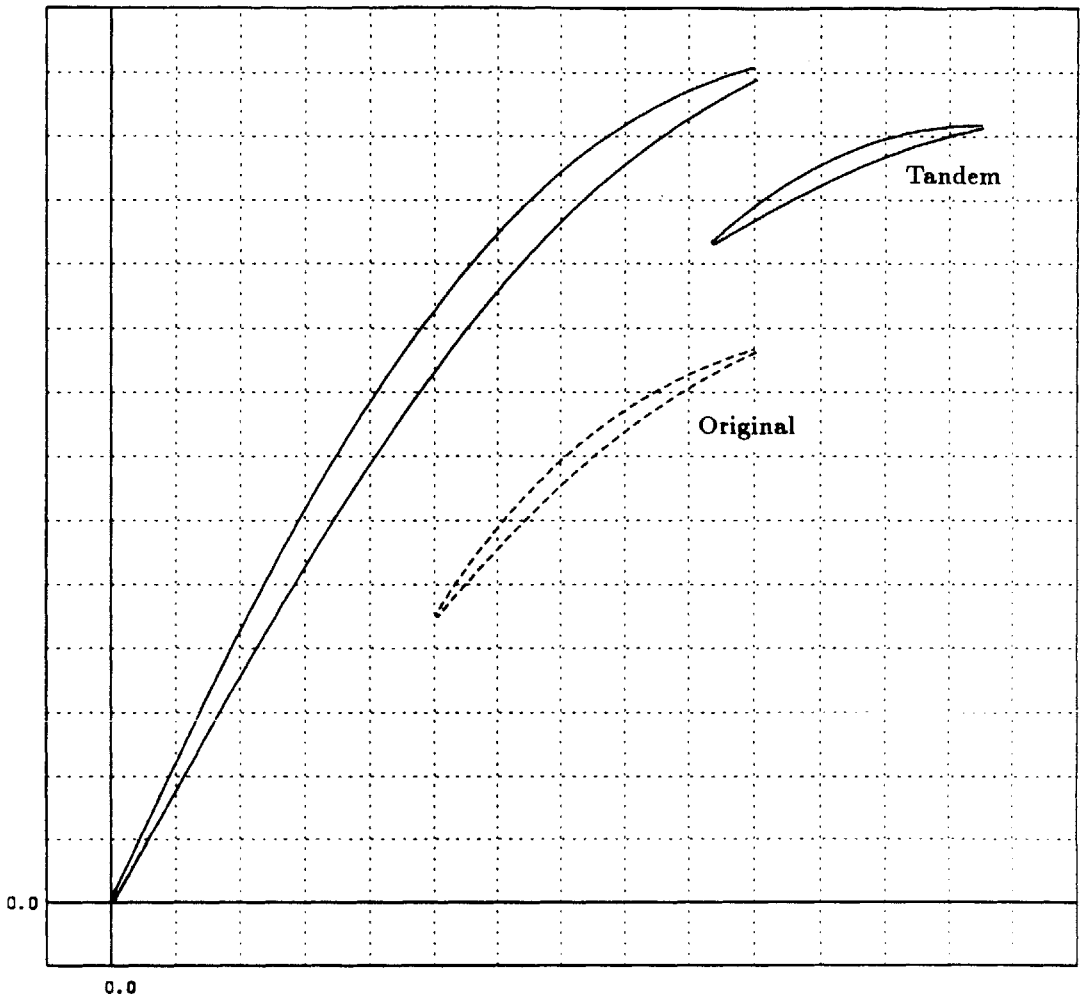

Figure 5.13: Tandem configuration with 70% chord splitter vane.

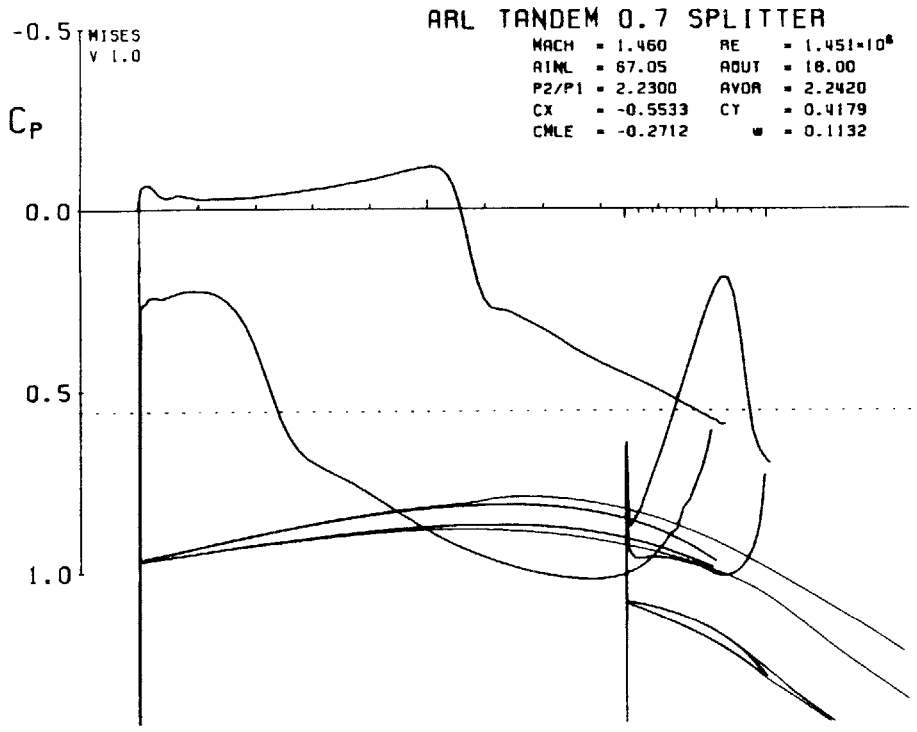

Figure 5.14: Surface pressures for 70% chord tandem splitter, 109% AVDR.

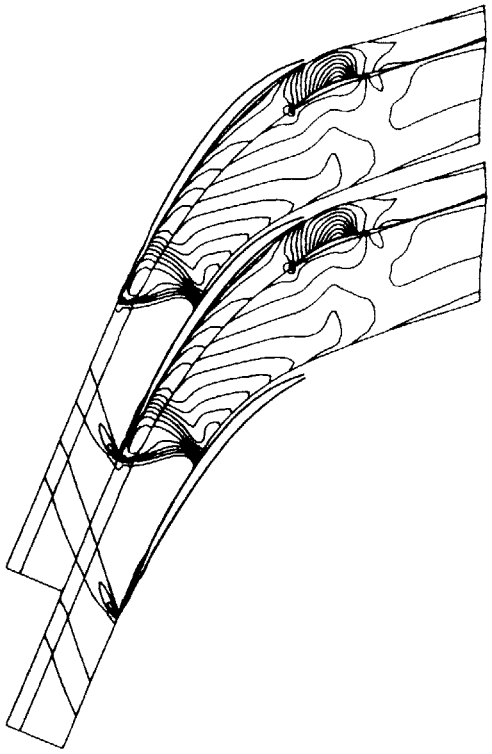

Figure 5.15: Mach contours for 70% chord tandem splitter

Chapter 6
Conclusions and Recommendations

This thesis has described the development of MISES, a new computational method for application to cascade analysis and design. This work extends the fully coupled viscous/inviscid ISES method for turbomachinery application. Quasi-three-dimensional effects for streamtube width and radius, as well as for rotational effects have been incorporated so that the method is applicable to blade-to-blade design of axial stator and rotor stages.

MISES uses a zonal approach to solve the coupled Euler and integral boundary layer equations. An intrinsic streamline grid is used, resulting in considerable simplification of the inviscid equations. The large non-linear system of equations is solved with a full Newton-Raphson method using a specialized direct solver. This allows the addition of extra unknowns and constraints that enforce specified design conditions. The modal design capability makes possible well-conditioned redesign of blades with areas of flow separation.

The flow solver was generalized to treat cascades with splitter vanes. A new grid topology using an offset-periodic inlet grid was introduced for supersonic cascades to circumvent problems with grid skew. The new grid also has the benefit of improving resolution of shock waves. Loss can be calculated from exit conditions or from a uniform mixed-out state. Loss sensitivities to cascade parameters such as Mach number, exit angle or exit pressure may also be calculated as a 'free' byproduct of the Newton solver. These sensitivities can be used to guide design optimization. The method is attractive for design applications due to its speed and robustness. Solutions are obtained in 6-30 Newton cycles — a matter of 1-20 minutes on a fast workstation.

6.1 Test Cases

Results were presented to validate the new capabilities of the method on subsonic, transonic and supersonic cascades. The results for the UTRC subsonic cascade showed excellent correlation of loss with experimental data. The DFVLR test case verified the quasi-3D capabilities with comparisons of surface presssures and loss for a blade at several AVDR and for transonic and supersonic Mach numbers. This case suffered from poorly specified conditions for supersonic inlet conditions, making comparisons difficult. The results showed that the streamtube width effects were accurately modeled and losses generally compared well with test data.

The ARL case proved to be the most difficult test of the quasi-3D capability as the result of its sensitivity to streamtube contraction and viscous blockage. Discrepancies between computational results and experimental data are undoubtedly due to three-dimensional effects from sidewall boundary layers. It is naive to assume that, in presence of such strongly separated flow, the upstream boundary layer bleed eliminated sidewall boundary layer effects. The sidewall boundary layers must be comparable in thickness to the blade boundary layers, hence the upper and lower passages will show radically different degrees of blockage. This violates the basic assumptions for the quasi-3D flow, making detailed comparison to test data questionable.

6.2 Splitter Vane Optimization

The analytical results for the ARL cascade indicate that the splitter circumferential position has almost no effect on loss or turning. This surprising result was reinforced when major redesign changes were made to the splitter vane and main blade to reduce loss. After significant geometric changes were made to both blades to optimize the surface pressure distributions, the performance was almost unchanged from the original cascade.

The general effect of the splitter is to reduce the loading of the main blade in the

overlap region. With the splitter vane located within the main passage the net loading and loss appear to be independent of the distribution of loading between the vane and the main blade. When the vane is moved aft, significant re-loading of the main blade occurs and turning is increased. The best position for the splitter vane appears to be in a tandem arrangement similar to the aft element in a multi-element airfoil. This configuration resulted in $+12^{\circ}$ of turning and a 15% reduction in loss.

6.3 Recommendations for Further Work

There are several extensions that should be considered for this work:

- Validation of MISES rotational capability using analytical test cases or high quality experimental data.
- Redesign to reduce loss using sensitivity information also reduced turning. A more automated design strategy should allow the designer to fix important design parameters such as exit angle. Such constraints can be easily implemented with the framework for the current method.
- The entrainment of the bow shock wake into the boundary layers is not fully represented in the present viscous/inviscid method. Although it is currently not clear how significant this effect is, a model for mixing within the near-wall streamtubes could be implemented.
- The linearization of the Jacobian entries using the chain rule is laborious and error-prone. The possibility of developing Newton methods using finite differences to calculate Jacobian entries should not be overlooked [20]. These approximate schemes could be effectively used to experiment with different approaches or to check analytic derivatives for errors.

6.4 Characteristics of Ill-posed Boundary Conditions

As discussed briefly in Chapter 2, it is possible to specify combinations of boundary conditions that are inconsistent with respect to the flow physics. With experience it is possible to recognize such ill-posed conditions by the characteristic behavior of the Newton solver. Figure 6.1 is presented as a guide to aid in recognizing these conditions. Good Luck!

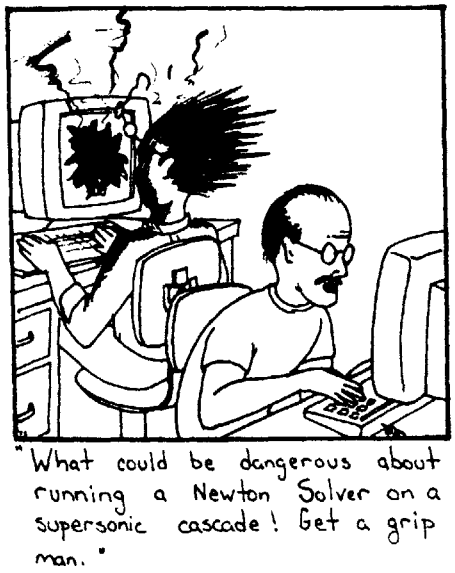

Figure 6.1: Characteristic behavior for ill-posed boundary conditions.

Appendix A
Development of Quasi-3D Euler Method

The development of the quasi-3D inviscid equations is an extension of the work by Giles [15] and Drela [9] on the ISES code. This chapter derives the quasi-3D formulation for the inviscid solver, and draws on the material in these references.

A.1 Coordinate System

The three-dimensional flow problem is approximated as a quasi-3D blade-to-blade flow defined on axisymmetric stream surfaces. The basic geometry of the problem is illustrated in Figure 2.2. Axisymmetric stream surfaces are defined in terms of the radius $r(z)$ and streamtube thickness $b(z)$, where z is the axial coordinate, see Figure 2.3. The axisymmetric stream surface radius and thickness distribution can be obtained by a meridional through-flow method.

The blade-to-blade flow is solved in a local m', θ stream surface coordinate system with stream surface radius and thickness. The new coordinate m' is defined as the arc-length in the $r - z$ plane, normalized by r.

$$m' = \int \frac{dm}{r} = \int \frac{\sqrt{(dr)^2 + (dz)^2}}{r}$$

Note that m', θ is a conformal mapping of the surface of revolution to a plane, preserving angles and shapes, and that both m' and θ are dimensionless and defined in radians. Since m' is an integral quantity it can be referenced to any convenient point, such as the leading edge. The relationship between m' and z is unique so that r and b may be defined $r = r(m')$ and $b = b(m')$.

In the following treatment m', θ will be replaced by x, y for convenience, except

where noted. The coordinates of a point (x, y) in the dimensionless system transforms to (rx, ry) in the physical system. The distance between two points A and B in the physical system is approximated for $|r_A - r_B| \ll r_A + r_B$ by

$$|\vec{AB}| \approx \frac{r_A + r_B}{2} |(x_B - x_A)\hat{\imath} + (y_B - y_A)\hat{\jmath}|$$

where $\hat{\imath}$ and $\hat{\jmath}$ are the unit vectors in the m' and the θ directions.

A.2 Euler Equations

As discussed in Chapter 2 the inviscid flow is solved using the steady-state Euler equations in a blade-relative coordinate system rotating with angular velocity $\vec{\Omega}$. The finite volume form was derived for conservation of mass, momentum and energy (equations 2.2 through 2.4).

The discrete equations approximate the integral form of the Euler equations on an intrinsic, or streamline, grid which evolves with the solution. The computational domain is made up of conservation cells defined on a set of streamtubes that make up the problem domain. The continuity and energy equations become simple algebraic statements of constant mass flow

$$\delta \dot{m} = 0$$

and constant rothalpy for each streamtube.

$$\delta \mathbf{I} = 0$$

The momentum equation

$$\oint_{\partial V} \rho(\vec{\mathbf{q}} \cdot \hat{\mathbf{n}})\vec{\mathbf{q}} + p\hat{\mathbf{n}}\, dA \;=\; -\oint_{V} \rho\vec{\mathbf{f}}\, dV \qquad \text{with } \vec{\mathbf{f}} = \vec{\Omega} \times \left(\vec{\Omega} \times \vec{r}\right) + 2\vec{\Omega} \times \vec{\mathbf{q}}$$

is also simplified since the conservation cells are defined such that only one pair of opposing faces has mass flux across them, the other faces are streamline faces and contribute only pressure terms. This has the effect that velocity and density are only required on the two streamwise faces, simplifying the system greatly.

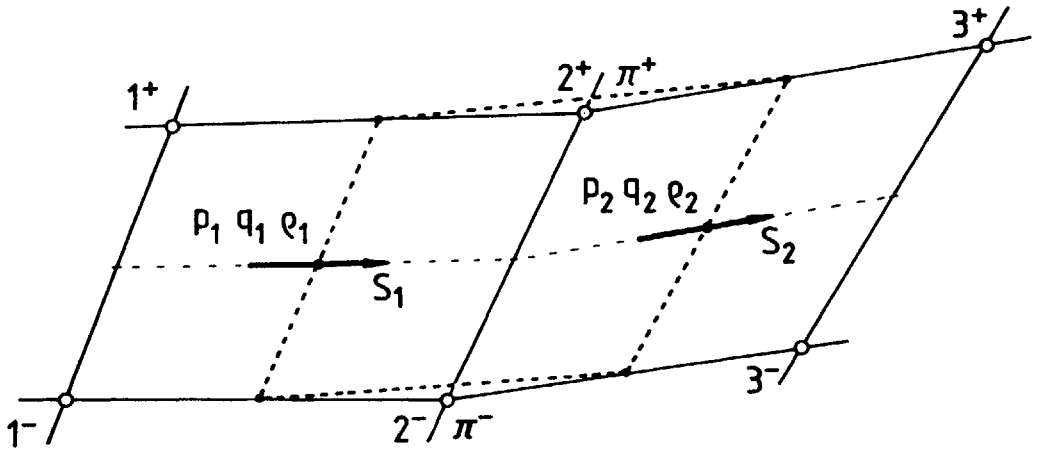

Figure A.1: Conservation cell on nodal grid

A.3 Conservation Cell

The flow equations are solved on an intrinsic grid that aligns in one of its directions with the streamline direction. Figure A.1 shows a view in the x, y (m', θ) plane the basic arrangement of a streamtube conservation cell superimposed on its defining six grid nodes. The lines of upper + and lower − grid nodes define streamwise faces of grid which have no mass flux across them, while the lines connecting the corresponding pairs of upper and lower nodes define the quasi-normals to the grid. Another view of conservation cell is shown in Figure A.2 illustrating the directed face area vectors, consisting of streamwise vectors B^+ and B^- defined between midpoints of contiguous streamline segments and pseudo-normal area vectors A_1 and A_2 defined midway between pairs of quasi-normal grid lines.

The faces of the quasi-3D conservation cell are illustrated in Figure A.3, where the edge vectors $\vec{A}$ and $\vec{B}$ define face areas of the six-sided conservation volume. The edge faces of the conservation cell are denoted by 1 and 2 for the streamtube inlet and outlet faces and + and − for the upper and lower streamline faces. The quasi-3D cell adds new faces on the inner and outer stream surfaces of revolution, denoted by $()_\mathbf{i}$ on the inner face and $()_\mathbf{o}$ on the outer face. Note that the areas of faces A_1, A_2, B^+ and B^- are functions of $b(x)$ and these faces lie between the inner and outer stream surfaces whose dimensional coordinates are functions of $r(x)$.

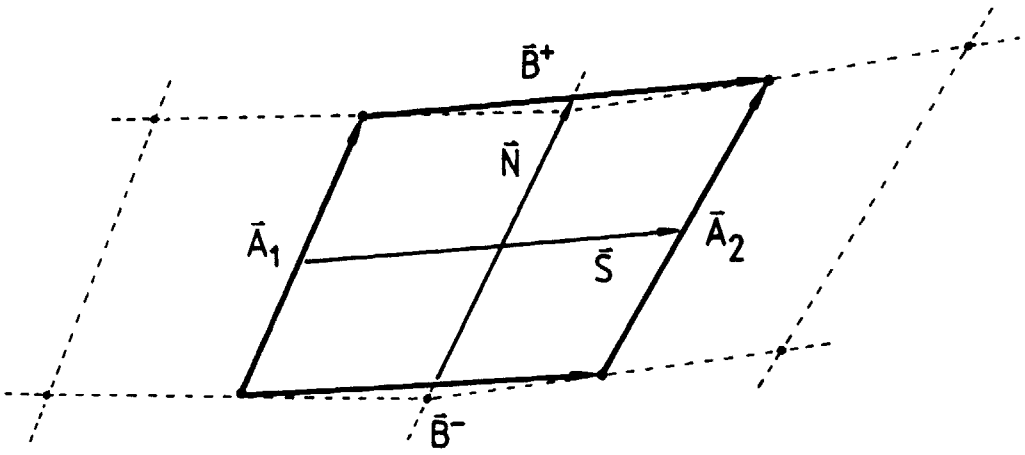

Figure A.2: Conservation cell and edge vectors

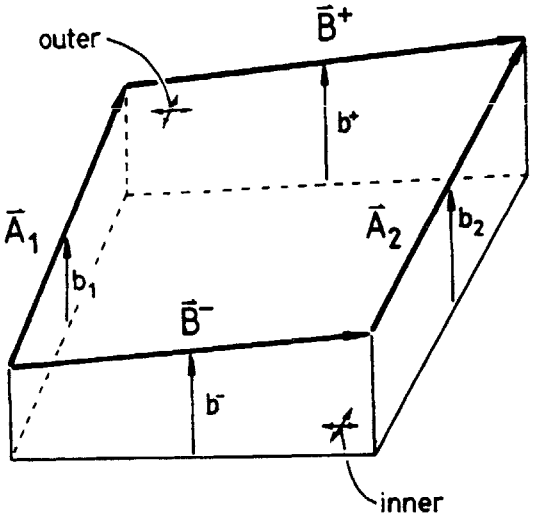

Figure A.3: Conservation cell

The face areas are defined as vectors in the $x-y$ plane

$$A_{x_1} = r_1 b_1 \frac{x_1^+ + x_2^+ - x_1^- - x_2^-}{2} \qquad A_{y_1} = r_1 b_1 \frac{y_1^+ + y_2^+ - y_1^- - y_2^-}{2}$$

$$A_{x_2} = r_2 b_2 \frac{x_2^+ + x_3^+ - x_2^- - x_3^-}{2} \qquad A_{y_2} = r_2 b_2 \frac{y_2^+ + y_3^+ - y_2^- - y_3^-}{2}$$

$$B_x^+ = r^+ b^+ \frac{x_3^+ - x_1^+}{2} \qquad B_y^+ = r^+ b^+ \frac{y_3^+ - y_1^+}{2}$$

$$B_x^- = r^- b^- \frac{x_3^- - x_1^-}{2} \qquad B_y^- = r^- b^- \frac{y_3^- - y_1^-}{2} \tag{A.1}$$

where the face radii and streamtube thicknesses are given by

$$r_1 = r\left(\frac{x_1^+ + x_2^+ + x_1^- + x_2^-}{2}\right) \qquad b_1 = b\left(\frac{x_1^+ + x_2^+ + x_1^- + x_2^-}{2}\right)$$

$$r_2 = r\left(\frac{x_2^+ + x_3^+ + x_2^- + x_3^-}{2}\right) \qquad b_2 = b\left(\frac{x_2^+ + x_3^+ + x_2^- + x_3^-}{2}\right)$$

$$r^+ = r\left(\frac{x_1^+ + x_3^+}{2}\right) \qquad b^+ = b\left(\frac{x_1^+ + x_3^+}{2}\right)$$

$$r^- = r\left(\frac{x_1^- + x_3^-}{2}\right) \qquad b^- = b\left(\frac{x_1^- + x_3^-}{2}\right) \tag{A.2}$$

It is useful to define a streamwise area vector $\vec{S}$ and a quasi-normal area vector $\vec{N}$ from the averages of the A and B vectors

$$\vec{S} = \frac{\vec{B}^- + \vec{B}^+}{2} \qquad \vec{N} = \frac{\vec{A}_1 + \vec{A}_2}{2} \tag{A.3}$$

The grid nodes are defined to lie on streamlines, so that the velocity vectors at the center of the 1 and 2 faces are defined lie on a line midway between the upper and lower streamlines. The velocity on the midpoint of the left cell face (at point 1) is $\vec{q}_1 = q_1 \hat{s}_1$, with the density and pressure at that point ρ_1 and p_1. The $\hat{s}_1$ vector is defined

$$s_{x_1} = \frac{x_2^+ + x_2^- - x_1^+ - x_1^-}{2} \qquad s_{y_1} = \frac{y_2^+ + y_2^- - y_1^+ - y_1^-}{2}$$

$$s_1 = \sqrt{s_{x_1}^2 + s_{y_1}^2} \qquad \hat{s}_1 = \frac{s_{x_1}}{s_1}\hat{\imath} + \frac{s_{y_1}}{s_1}\hat{\jmath} \tag{A.4}$$

Similarly the flow quantities on the right cell face 2) are $\vec{q}_2 = q_2 \hat{s}_2$, ρ_2 and p_2, where the $\hat{s}_2$ vector is defined

$$s_{x_2} = \frac{x_3^+ + x_3^- - x_2^+ - x_2^-}{2} \qquad s_{y_2} = \frac{y_3^+ + y_3^- - y_2^+ - y_2^-}{2}$$

$$s_2 = \sqrt{s_{x_2}^2 + s_{y_2}^2} \qquad \hat{s}_2 = \frac{s_{x_2}}{s_2}\hat{\imath} + \frac{s_{y_2}}{s_2}\hat{\jmath} \tag{A.5}$$

The streamtube cross-section area is the area normal to the the $\vec{s}$ face velocity vector. The normal areas in and out of the conservation cell are

$$A_{n_1} = |\hat{s}_1 \times \vec{A}_1| \qquad A_{n_2} = |\hat{s}_2 \times \vec{A}_2| \tag{A.6}$$

To obtain the area contributed by the inner and outer stream surface faces consider the normal area vector of the inner face i as $\vec{a_i} = a_i \hat{n}_i$, similarly for the outer face $\vec{a_o}$ and the four edge faces. The normal area vectors of the faces of the the closed conservation cell must sum to zero, by simple geometric identity. This defines the net normal area vector of the inner and outer faces to be

$$\vec{a}_i + \vec{a}_o = -(\vec{a}_1 + \vec{a}_1 + \vec{a}^+ + \vec{a}^-) \tag{A.7}$$

The normal area vectors of the faces are expressed in terms of the face area vectors as

$$\vec{a}_1 = (-A_{y_1}\hat{\imath},\ A_{x_1}\hat{\jmath}) \qquad \vec{a}_2 = (A_{y_2}\hat{\imath},\ -A_{x_2}\hat{\jmath})$$

$$\vec{a}^+ = (-B_y^+\hat{\imath},\ B_x^+\hat{\jmath}) \qquad \vec{a}^- = (B_y^-\hat{\imath},\ -B_x^-\hat{\jmath}) \tag{A.8}$$

The volume of the conservation cell is

$$\Delta V = \frac{|\vec{S} \times \vec{N}|}{b} \tag{A.9}$$

where b is the cell average streamtube thickness.

A.4 Continuity Equation

The mass equation is simplified by use of the streamline grid to be a statement of constant mass flow everywhere along a stream tube. For each cell, therefore

$$\dot{m} = \rho_1\, q_1\, A_{n_1} = \rho_2\, q_2\, A_{n_2} \tag{A.10}$$

The mass flow in each streamtube is set from the inlet conditions and inlet node positions defining the streamtube normal area.

A.5 Momentum Equation

The momentum equation for the conservation cell is composed of pressure terms, mass flux terms and source terms due to rotation (Coriolis and centrifugal forces).

$$-\vec{F}_{flux} - \vec{F}_{press} = \vec{F}_{coriolis} + \vec{F}_{cent} \tag{A.11}$$

The discrete equations for x and y momentum are resolved into a local streamwise, or S-momentum equation and a quasi-normal, or N-momentum equation by

$$\text{S-momentum} \longrightarrow \vec{S} \cdot \sum \vec{F}$$

$$\text{N-momentum} \longrightarrow \vec{N} \cdot \sum \vec{F}$$

A.5.1 Pressure Terms

The pressures on the inner and outer faces are assumed to both take the average value of the pressures on the four edge faces

$$p_{\mathbf{i}} = p_{\mathbf{o}} = \frac{p_1 + p_2 + \Pi^+ + \Pi^-}{4}$$

In this case the sum of the pressure forces acting on the cell faces is

$$\begin{aligned} -\vec{F}_{press} &= p_1\vec{a}_1 + p_2\vec{a}_2 + \Pi^+\vec{a}^+ + \Pi^-\vec{a}^- \\ &\quad - \frac{1}{4}\left(p_1 + p_2 + \Pi^+ + \Pi^-\right)\left(\vec{a}_1 + \vec{a}_2 + \vec{a}^+ + \vec{a}^-\right) \end{aligned}$$

After tedious manipulation this becomes

$$\begin{aligned} -\vec{F}_{press} &= \frac{(p_1 - p_2)}{2}\left(\vec{a}_1 - \vec{a}_2\right) + \frac{(\Pi^+ - \Pi^-)}{2}\left(\vec{a}^+ - \vec{a}^-\right) \\ &\quad + \frac{(p_1 + p_2 - \Pi^+ - \Pi^-)}{4}\left(\vec{a}_1 + \vec{a}_2 - \vec{a}^+ - \vec{a}^-\right) \end{aligned} \tag{A.12}$$

The combined pressure term has special significance and is denoted by

$$P_{corr} = \frac{\Pi^+ + \Pi^- - p_1 - p_2}{2} \tag{A.13}$$

which will approach zero in the limit as the grid is refined, where the averages of the pressures on opposite face pairs will be equal. Unfortunately, Equation A.13 is transparent to an odd-even grid mode. To prevent grid sawtooth instabilities another form for P_{corr} is used, based on the isentropic pressure-area ratio

$$P_{corr} = k \frac{\gamma p M^2}{2} \frac{|\vec{s_1^-} \times \vec{s_2^-}| - |\vec{s_1^+} \times \vec{s_2^+}|}{|\vec{S} \times \vec{N}|} \tag{A.14}$$

$$\text{where } p = \frac{p_1 + p_2}{2} \quad \text{and} \quad M^2 = \frac{M_1^2 + M_2^2}{2}$$

The constant k is used to set the relative magnitude of the P_{corr} term and typically has a value 0.1.

The x and y components of the pressure forces, using the area normal vectors in A.8 and the definitions A.3, are

$$\begin{aligned} -F_{x_{press}} &= -(p_1 - p_2) N_y - (\Pi^+ - \Pi^-) S_y \\ &\quad - P_{corr} \left(\frac{-A_{y_1} + A_{y_2} + B_y^+ - B_y^-}{2} \right) \\ -F_{y_{press}} &= (p_1 - p_2) N_x + (\Pi^+ - \Pi^-) S_x \\ &\quad + P_{corr} \left(\frac{-A_{x_1} + A_{x_2} + B_x^+ - B_x^-}{2} \right) \end{aligned} \tag{A.15}$$

The S and N components of the pressure terms are formed by taking the dot product of A.15 with the $\vec{S}$ and $\vec{N}$ vectors.

$$\begin{aligned} -\vec{S} \cdot \vec{F}_{press} &= -(p_1 - p_2) |\vec{S} \times \vec{N}| \\ &\quad - P_{corr} \frac{|\vec{S} \times (-\vec{A}_1 + \vec{A}_2 + \vec{B}^+ - \vec{B}^-)|}{2} \\ -\vec{N} \cdot \vec{F}_{press} &= -(\Pi^- - \Pi^+) |\vec{S} \times \vec{N}| \\ &\quad - P_{corr} \frac{|\vec{N} \times (-\vec{A}_1 + \vec{A}_2 + \vec{B}^+ - \vec{B}^-)|}{2} \end{aligned} \tag{A.16}$$

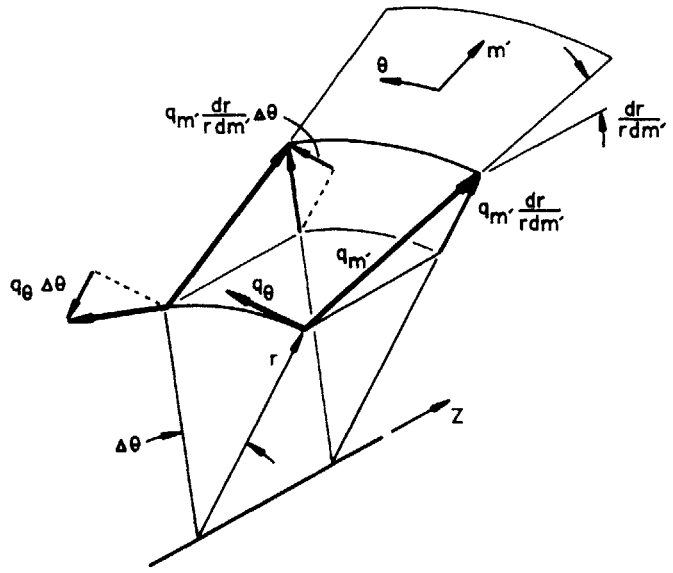

Figure A.4: Flux terms from circumferential displacement of velocity vectors

A.5.2 Flux Terms

The mass flux terms are given by the net momentum flux through cell faces 1 and 2. Additional terms are required for the quasi-3D cell because the x, y coordinates are defined on a surface of revolution and the unit vectors of the local system change direction with circumferential coordinate y (or θ). For the following discussion the $m' - \theta$ terminology will be used in place of x, y for clarity with regard to angles on the curved stream surface.

The basic statement for the mass flux forces is

$$-F_{flux} = \dot{m}\left(\Delta(q_{m'}\hat{e}_{m'}) + \Delta(q_\theta \hat{e}_\theta)\right) \qquad \text{where } \Delta() = ()_2 - ()_1 \qquad \text{(A.17)}$$

where $\dot{m} = \rho q A$ is the mass flux in the streamtube and $e_{m'}$ and e_θ are unit vectors on the stream surface. Additional terms arise for the $\Delta()$ expressions due to the change in directions of the unit vectors with a displacement $\Delta\theta$ in the circumferential direction. Figure A.4 illustrates the basic geometry, where a vector $(q_{m'}, q_\theta)$ defined on a stream surface tilted by $dr/(rdm')$ from the axial direction is displaced by $\Delta\theta$ in the circumferential direction.

The $\Delta q_{m'}$... term in A.17 expands to

$$\begin{aligned}\Delta(q_{m'}\hat{e}_{m'}) &= \Delta q_{m'}\hat{e}_{m'} + q_{m'}(\hat{e}_{m'_2} - \hat{e}_{m'_1}) \\ &= \Delta q_{m'}\hat{e}_{m'} + q_{m'}\Delta\theta\frac{dr}{rdm'}\hat{e}_\theta \end{aligned} \tag{A.18}$$

where the $\hat{e}_\theta$ term is due to the radial component of $q_{m'}$ on the tilted stream surface, $q_{m'}dr/(rdm')$, which is rotated by a change of direction $\Delta\theta$, producing a component normal to the $\hat{e}_{m'}$ vector at the original position.

The Δq_θ... term in A.17 expands to

$$\begin{aligned}\Delta(q_\theta\hat{e}_\theta) &= \Delta q_\theta\hat{e}_\theta + q_\theta(\hat{e}_{\theta_2} - \hat{e}_{\theta_1}) \\ &= \Delta q_\theta\hat{e}_\theta - q_\theta\Delta\theta\frac{dr}{rdm'}\hat{e}_{m'} \end{aligned} \tag{A.19}$$

where the $\hat{e}_{m'}$ term is due to rotation of q_θ by a change of direction $\Delta\theta$, producing a radial component $-q_\theta\Delta\theta$ that has a component along the tilted stream surface in the $\hat{e}_{m'}$ direction.

The force due to the mass flux is then

$$-\vec{F}_{flux} = m\left((\Delta(q_{m'} - q_\theta\Delta\theta\frac{dr}{rdm'})\hat{e}_{m'} + (\Delta(q_\theta + q_{m'}\Delta\theta\frac{dr}{rdm'})\hat{e}_\theta\right) \tag{A.20}$$

Continuity for the cell requires that $q_{m'}\Delta\theta = q_\theta\Delta m'$.

The $\hat{e}_\theta$ term becomes

$$\begin{aligned}\Delta q_\theta + q_{m'}\Delta\theta\frac{dr}{rdm'} &\simeq \Delta q_\theta + q_\theta\Delta m'\frac{\Delta r}{r\Delta m'} \\ &= \frac{\Delta(rq_\theta)}{r} \end{aligned} \tag{A.21}$$

The $\hat{e}_{m'}$ term gives

$$\begin{aligned}\Delta q_{m'} + q_\theta\Delta\theta\frac{dr}{rdm'} &= \Delta q_{m'} + q_\theta\Delta m'\frac{\Delta r}{r\Delta m'} \\ &= \frac{\Delta(rq_{m'})}{r} - \frac{\Delta r q_{m'}}{r} - q_\theta\Delta\theta\frac{dr}{rdm'} \\ &= \frac{\Delta(rq_{m'})}{r} - (\frac{\Delta r}{r\Delta m'}q_{m'}\Delta m' + q_\theta\Delta\theta\frac{dr}{rdm'}) \\ &\simeq \frac{\Delta(rq_{m'})}{r} - (q_{m'}\Delta m' + q_\theta\Delta\theta)\frac{dr}{rdm'}\end{aligned}$$

Using $\vec{q} = q_{m'}\hat{e}_{m'} + q_\theta \hat{e}_\theta$ and $\Delta s = r\sqrt{\Delta m'^2 + \Delta\theta^2}$ the last term can be simplified

$$\Delta q_{m'} + q_\theta \Delta\theta \frac{dr}{r dm'} = \frac{\Delta(r q_{m'})}{r} - q\frac{\Delta s}{r}\frac{dr}{r dm'} \tag{A.22}$$

Now, returning to the use of x, y to represent the stream surface coordinates m', θ, we have the forces due to the momentum flux.

The x and y components of the flux forces are

$$\begin{aligned} -F_{x_{flux}} &= \frac{2\dot{m}}{r_1 + r_2}\left(-r_1 q_1 \hat{s}_{x_1} + r_2 q_2 \hat{s}_{x_2} - \frac{q_1 \hat{s}_1 \cdot \vec{S} + q_2 \hat{s}_2 \cdot \vec{S}}{2\,b}\frac{dr}{r dx}\right) \\ -F_{y_{flux}} &= \frac{2\dot{m}}{r_1 + r_2}\left(-r_1 q_1 \hat{s}_{y_1} + r_2 q_2 \hat{s}_{y_2}\right) \end{aligned} \tag{A.23}$$

The S and N components of the momentum flux terms are formed by taking the dot product of A.23 with $\vec{S}$ and $\vec{N}$.

$$\begin{aligned} -\vec{N}\cdot\vec{F}_{flux} &= \\ &\frac{2\dot{m}}{r_1 + r_2}\left[-r_1 q_1(\hat{s}_1 \cdot \vec{N}) + r_2 q_2(\hat{s}_2 \cdot \vec{N}) - \frac{r^+ - r^-}{2}\left(q_1 \hat{s}_1 \cdot \vec{S} + q_2 \hat{s}_2 \cdot \vec{S}\right)\right] \\ -\vec{S}\cdot\vec{F}_{flux} &= \dot{m}\left(-q_1(\hat{s}_1 \cdot \vec{S}) + q_2(\hat{s}_2 \cdot \vec{S})\right) \end{aligned} \tag{A.24}$$

Where one of the the approximate identities for $dr/(r dx)$

$$\frac{dr}{r dx} \simeq \frac{r_2 - r_1}{S_x/b} \quad \text{and} \quad \frac{dr}{r dx} \simeq \frac{r^+ - r^-}{N_x/b} \tag{A.25}$$

has been used to simplify the N-momentum component.

A.5.3 Rotational Forces

The use of a blade-relative coordinate system brings additional acceleration terms into the momentum equation. The coordinate system is rotating at angular velocity Ω leading to Coriolis forces and centrifugal forces on the fluid in the cell.

Coriolis Forces

The Coriolis force per unit volume in a rotating fluid is

$$\frac{\vec{F}_{coriolis}}{\Delta V} = -2\rho\left(\vec{\Omega} \times \vec{q}\right)$$

Since the velocity is defined in the $\vec{S}$ direction the force on a computational cell purely in the $\vec{N}$ direction.

$$\begin{aligned}
\vec{N} \cdot \vec{F}_{coriolis} &= -2\rho\left(\vec{\Omega} \times \vec{q}\right) \cdot \vec{N}\ \Delta V \\
&= -2\rho q\vec{\Omega} \cdot \left(\hat{s} \times \vec{N}\right)\ \Delta V \\
&\quad \text{using}\ \ A_n = |\hat{s} \times \vec{N}|\ \ \text{and}\ \ \dot{m} = \rho q A_n \\
&= -2\dot{m}\Omega\frac{dr}{r dx}\ \Delta V
\end{aligned}$$

This can be simplified using approximate identities for $dr/(rdx)$ in A.25 and the definition of ΔV to be

$$\vec{N} \cdot \vec{F}_{coriolis} = -2\dot{m}\Omega\left(N_y(r_2 - r_1) - S_y(r^+ - r^-)\right) \qquad \text{(A.26)}$$

Centrifugal Forces

The centrifugal force per unit volume in a rotating fluid is $\rho\Omega^2 r$ in the radial direction. This has a component in the x direction due to the inclination of the stream surface by $dr/(rdx)$ from the axial direction. The x component of the centrifugal force on a cell is

$$F_{x_{cent}} = \rho\,\Omega^2 r\frac{dr}{r dx}\Delta V \qquad \text{(A.27)}$$

where $\rho = \frac{1}{2}(\rho_1 + \rho_2)$, the average cell density.

The streamwise and normal centrifugal forces on a cell are

$$\begin{aligned}
\vec{S} \cdot \vec{F}_{cent} &= \rho\,\Omega^2 r S_x\frac{dr}{r dx}\Delta V \\
&= \frac{\rho\,\Omega^2}{2}\left(r_2^2 - r_1^2\right)|\vec{S} \times \vec{N}| \qquad \text{using A.25}
\end{aligned}$$

$$\vec{N} \cdot \vec{F}_{cent} = \rho \Omega^2 r N_x \frac{dr}{r dx} \Delta V$$

$$= \frac{\rho \Omega^2}{2} \left(r^{+2} - r^{-2} \right) |\vec{S} \times \vec{N}| \qquad \text{using A.25} \qquad \text{(A.28)}$$

A.5.4 S and N Momentum Equations

In the preceeding sections, the x and y components of the cell forces were used to define momentum components in both a "streamwise" or S-momentum equation and a "normal" or N-momentum equation. Collecting terms from Equations A.16, A.24, A.26 and A.28 and dividing through by $|\vec{S} \times \vec{N}|$ we obtain the **S-momentum** equation

$$\frac{\rho \Omega^2}{2} \left(r_2^2 - r_1^2 \right) =$$

$$\dot{m} \left(-q_1 f_1 + q_2 f_2 \right)$$

$$- (p_1 - p_2) - \frac{P_{corr}}{2} \frac{|\vec{S} \times (-\vec{A}_1 + \vec{A}_2 + \vec{B}^+ - \vec{B}^-)|}{|\vec{S} \times \vec{N}|} \qquad \text{(A.29)}$$

where the new terms are defined

$$f_1 = \frac{\hat{s}_1 \cdot \vec{S}}{|\vec{S} \times \vec{N}|} \qquad f_2 = \frac{\hat{s}_2 \cdot \vec{S}}{|\vec{S} \times \vec{N}|} \qquad \text{(A.30)}$$

The **N-momentum** equation is similarly defined as

$$\frac{\rho \Omega^2}{2} \left(r^{+2} - r^{-2} \right) - 2\dot{m}\Omega \frac{\left(N_y (r_2 - r_1) - S_y (r^+ - r^-) \right)}{|\vec{S} \times \vec{N}|} =$$

$$\frac{2\dot{m}}{r_1 + r_2} \left[-r_1 q_1 g_1 + r_2 q_2 g_2 - \frac{r^+ - r^-}{2} (q_1 f_1 + q_2 f_2) \right]$$

$$- (\Pi^- - \Pi^+) - \frac{P_{corr}}{2} \frac{|\vec{N} \times (-\vec{A}_1 + \vec{A}_2 + \vec{B}^+ - \vec{B}^-)|}{|\vec{S} \times \vec{N}|} \qquad \text{(A.31)}$$

with new terms

$$g_1 = \frac{\hat{s}_1 \cdot \vec{N}}{|\vec{S} \times \vec{N}|} \qquad g_2 = \frac{\hat{s}_2 \cdot \vec{N}}{|\vec{S} \times \vec{N}|} \qquad \text{(A.32)}$$

A.5.5 Upwinding Scheme

The S and N momentum equations are modified in supersonic zones by the use of artificial dissipation in the form of a bulk viscosity term, defined as in Drela's thesis [9], by upwinding the speeds q_1 and q_2 in A.29 and A.31. This scheme has been extended to include an optional second-order dissipation term that can significantly reduce spurious total pressure losses due to added dissipation. The basis for this idea comes from Giles' second-order dissipation scheme in [15] but has been applied to the bulk viscosity dissipation model. The form of the upwinded speed is

$$\tilde{q}_i \;=\; q_i - \lambda_i(q_i - q_{i-1}) + \mu_i(q_{i-1} - q_{i-2}) \qquad \text{(A.33)}$$

The upwinded speed thus depends on the speed at cell face i and one or two upstream speeds, depending on whether second-order dissipation is used.

The definition for the first-order upwinding coefficient, λ is

$$\lambda_i = \mu_{con} \max\left(0,\ \frac{M^2 - M_c^2}{\gamma M^2}\right) \qquad \text{where } M^2 = \max(M_i^2, M_{i-1}^2) \qquad \text{(A.34)}$$

where μ_{con} is a scaling factor for dissipation (normally 1.0) and M_{crit} is a threshold slightly less than unity (typically 0.9).

The second order upwinding coefficient is set such that $\mu = \lambda$, producing second-order dissipation when the grid nodes are equally spaced. This does not produce enough dissipation in strong gradients (shocks) and μ is reduced by a factor proportional to velocity gradient, preferentially for decelerating flow to minimize spurious loss in accelerations. The use of second order dissipation complicates the numerical form of the equations by introducing dependence on the *two* previous cell face speeds, rather than simply the previous speed. This will add terms to the matrix, increasing the solution cost slightly. In practice, the use of the second order dissipation has been limited to transonic Mach numbers. For supersonic inlet Mach numbers the second order scheme appears to have some unsolved stability problems.

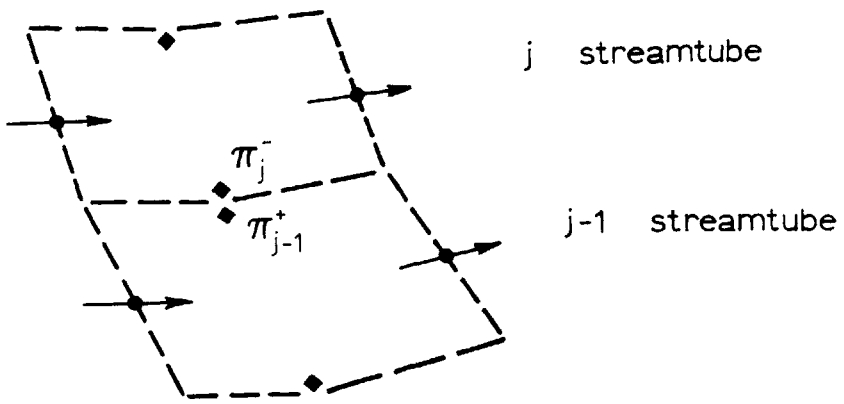

Figure A.5: Pressures on neighboring streamtubes

A.5.6 Reduced N-Momentum Equation

The S-momentum equation A.29, using the upwinded speeds $\tilde{q}_1$ and $\tilde{q}_2$, depends only on the geometry, upwinded speed, density, pressure at faces 1 and 2, and P_{corr}. Unfortunately the N-momentum equation, A.31, contains additional pressure terms Π^+ and Π^- on the streamline faces. These can be eliminated to reduce the number of unknowns and form the **reduced N-momentum** equation that depends only on P_{corr} and the geometry, upwinded speed, density and pressure at faces 1 and 2. This is done in the same manner as in Drela's thesis, where the N-momentum equation A.31 can be written in the form

$$\Pi^+ - \Pi^- \;=\; (\cdots)$$

The P_{corr} equation, A.13, can be written in the form

$$\Pi^+ + \Pi^- \;=\; p_1 + p_2 + 2\,P_{corr}$$

The sum and difference of these two equations define equations for Π_j^+ and for Π_j^- on streamtube j.

Since the Π pressures on matching edges of neighboring streamtubes correspond, as shown in Figure A.5, the Π variables can be eliminated by taking the difference of the Π^+ equation for cell i on streamline $j-1$ and the Π^- equation for cell i on streamline j. The resulting equation effectively couples each pair of streamtubes through the corresponding

pressures on the streamline faces, which never explicitly appear as unknowns but whose difference will approach zero as the solution converges. It is interesting to observe that the Newton system solves the steady state equations by balancing the streamwise momentum equation and by driving the streamtube coupling pressure difference, $\Pi_j^- - \Pi_{j-1}^+$, to zero.

A.6 Energy Equation

The energy equation in the blade-relative coordinate system rotating with angular velocity Ω is a statement of constant *rothalpy* along the streamtube,

$$\mathbf{I} = \mathbf{I}_1 = \mathbf{I}_2 \qquad \text{where } \mathbf{I} = h + \frac{q^2}{2} - \frac{(\Omega r)^2}{2} \tag{A.35}$$

with q as the speed in the blade relative frame and h as the static enthalpy of the fluid. This statement implies that the reference rothalpy is the stagnation enthalpy at $r = 0$. The following definitions are used for quantities in the rotating system.

The static enthalpy on the stream surface at radius r is

$$h = \mathbf{I} - \frac{q^2}{2} + \frac{(\Omega r)^2}{2} \tag{A.36}$$

The stagnation enthalpy at radius r is

$$h_0 = \mathbf{I} + \frac{(\Omega r)^2}{2} \tag{A.37}$$

The pressure is derived from the definition of enthalpy $h = \frac{\gamma}{\gamma-1}\frac{p}{\rho}$, so that

$$p = \frac{\gamma - 1}{\gamma}\rho\left(\mathbf{I} - \frac{q^2}{2} + \frac{(\Omega r)^2}{2}\right) \tag{A.38}$$

The Mach number is defined using $a^2 = \frac{\gamma p}{\rho}$, which gives

$$M^2 = \frac{q^2}{a^2} = \frac{q^2}{(\gamma - 1)\left(\mathbf{I} - \frac{q^2}{2} + \frac{(\Omega r)^2}{2}\right)} \tag{A.39}$$

Finally, the temperature ratio is defined as

$$\frac{T_0}{T} = \frac{\mathbf{I}}{h} = \frac{\mathbf{I}}{\mathbf{I} - \frac{q^2}{2} + \frac{(\Omega r)^2}{2}} \tag{A.40}$$

The usual definitions for stagnation quantities can be obtained from A.40, but the radius must be considered in defining reference quantities. For example, the stagnation density at $r = 0$ in terms of the density at r with velocity q is

$$\rho_0 = \rho \left(\frac{\mathbf{I}}{\mathbf{I} - \frac{q^2}{2} + \frac{(\Omega r)^2}{2}} \right)^{\frac{1}{\gamma - 1}} \tag{A.41}$$

A.7 Linearization of Equations

Since the flow equations and boundary conditions are non-linear a Newton-Raphson procedure is used to solve the resulting numerical system. The S-momentum equation and reduced N-momentum equation are linearized in terms of perturbations to the cell geometry $x, y^{\pm}_{1,2,3}$ and cell face velocity q, density ρ and pressure p in the same manner as in the two ISES theses [15, 9]. The principal differences from their procedure stem from additional terms due to dr/dx and db/dx. This set of unknowns are systematically reduced using the chain rule until the momentum equations are expressed solely in terms of the cell face density changes $\delta\rho$ and normal movement of the streamline nodes δn. The details of this process are exhaustive and, in the interests of brevity, are best left for a perusal of the Fortran coding.

Several additional global variables are also required for perturbations to mass flow, inlet and exit angles, inlet characteristic, leading edge position, exit pressure and design variables. These are used to implement boundary conditions for analysis and design applications.

Appendix B
Development of Quasi-3D Boundary Layer

The integral boundary layer method developed for ISES is modified to include effects for streamtube thickness, radius, and rotation. These effects have been included without drastically altering the framework of the basic method, as reviewed below. The details of Drela's derivation of the closure relations are not repeated as they are unchanged and can be best obtained from his thesis [9] and subsequent papers [13].

B.1 Background - 2D Boundary Layer

This section presents the basic relations from Drela's 2D integral boundary layer method. The boundary layer development is defined by two principal equations, the classic von Kármán integral momentum equation

$$\frac{1}{\theta}\frac{d\theta}{ds} = \frac{1}{\theta}\frac{C_f}{2} - \left(H + 2 - M_e^2\right)\frac{1}{u_e}\frac{du_e}{ds} \tag{B.1}$$

and the integral kinetic energy equation, obtained by integrating the differential momentum equation multiplied by u.

$$\frac{1}{\theta^*}\frac{d\theta^*}{ds} = \frac{1}{\theta^*}2C_D - \left(\frac{2H^{**}}{H^*} + 3 - M_e^2\right)\frac{1}{u_e}\frac{du_e}{ds} \tag{B.2}$$

where s is the arc-length along the boundary, u_e is the edge velocity and M_e is the edge Mach number. The shape parameters H, H^* and H^{**} are defined as

$$H = \frac{\delta^*}{\theta} \qquad H^* = \frac{\theta^*}{\theta} \qquad H^{**} = \frac{\delta^{**}}{\theta} \tag{B.3}$$

expressed using the integral thicknesses

$$\delta^* = \int_0^\infty \left(1 - \frac{\rho u}{\rho_e u_e}\right) dy \qquad \theta = \int_0^\infty \left(1 - \frac{u}{u_e}\right)\frac{\rho u}{\rho_e u_e} dy \tag{B.4}$$

$$\delta^{**} = \int_0^\infty \left(1 - \frac{\rho}{\rho_e}\right)\frac{u}{u_e}dy \qquad \theta^* = \int_0^\infty \left(1 - \left(\frac{u}{u_e}\right)^2\right)\frac{\rho u}{\rho_e u_e}dy \tag{B.5}$$

where η is the wall normal coordinate and ρ_e and u_e are flow quantities at the edge of the EIF. The skin friction coefficient C_f and dissipation coefficient C_D are defined by

$$C_f = \frac{2}{\rho_e u_e^2}\tau_w \qquad C_D = \frac{1}{\rho_e u_e^3}\int_0^\infty \tau\frac{\partial u}{\partial y}dy \tag{B.6}$$

The kinetic energy equation B.2 is not directly used, instead it is combined with the momentum equation to give the so-called shape parameter equation

$$\frac{1}{H^*}\frac{dH^*}{ds} = \frac{1}{\theta}\left(\frac{2C_D}{H^*} - \frac{C_f}{2}\right) - \left(\frac{2H^{**}}{H^*} + 1 - H\right)\frac{1}{u_e}\frac{du_e}{ds} \tag{B.7}$$

In the boundary layer solution the momentum equation and the shape parameter equation are augmented by a third equation, depending on boundary layer type.

Laminar A disturbance amplification equation is used to determine transition location. The amplification equation is an envelope method, based on correlations from maximum spatial amplification growth rates from the Orr-Sommerfeld equation.

Turbulent A dissipation lag equation is used to model upstream history effects. The lag equation is similar to Green's lag equation [10].

Laminar closure relations, derived using Falkner-Skan profiles, provide correlations between shape factors, skin friction and dissipation. Similarly for turbulent flow, Swafford's profiles were used to derive relations for turbulent closure.

The three equations characterize the development of the boundary at any streamwise station and are discretized along with the Euler outer flow and solved by Newton's method. Since the inviscid outer flow and the boundary layer are solved simultaneously, separated flows and transitional separation bubbles can be modeled.

B.2 Quasi-3D Boundary Layer

The quasi-3D equations are derived in the same manner as the 2D equations, integrating the differential form of the momentum equation but including the effects of streamtube thickness b, radius r and rotation Ω. The momentum equation becomes

$$\begin{aligned}\frac{1}{\theta}\frac{d\theta}{ds} &= \frac{1}{\theta}\frac{C_f}{2} - \left(H + 2 - M_e^2\right)\frac{1}{u_e}\frac{du_e}{ds} \\ &\quad - \frac{1}{b}\frac{db}{ds} + \left(H_\rho - M_e^2\right)\left(\frac{\Omega r}{u_e}\right)^2 \frac{1}{r}\frac{dr}{ds}\end{aligned} \tag{B.8}$$

and the shape parameter equation is

$$\begin{aligned}\frac{1}{H^*}\frac{dH^*}{ds} &= \frac{1}{\theta}\left(\frac{2C_D}{H^*} - \frac{C_f}{2}\right) - \left(\frac{2H^{**}}{H^*} + 1 - H\right)\frac{1}{u_e}\frac{du_e}{ds} \\ &\quad - \left(H_\rho - \frac{2H^{**}}{H^*}\right)\left(\frac{\Omega r}{u_e}\right)^2 \frac{1}{r}\frac{dr}{ds}\end{aligned} \tag{B.9}$$

The integral thicknesses used in the shape parameters for B.9 and B.10 are defined as in B.4 and B.5 but $r dy$ is used in place of dy as the integration variable increment normal to the wall. Similarly for the definition of the dissipation coefficient C_D. The new shape parameter that appears is $H_\rho = \delta_\rho/\theta$, where the density thickness δ_ρ is given by

$$\delta_\rho = \int \left(1 - \frac{\rho}{\rho_e}\right) r\, dy \tag{B.10}$$

The shape parameter H_ρ is defined by Green [10] as a function of kinematic shape factor and Mach number

$$H_\rho \simeq (0.185 H_k + 0.15)\, M_e^2 \tag{B.11}$$

where H_k is the kinematic shape factor correlated to H and M_e^2 by Whitfield [21] as

$$H_k = \frac{\int_0^\infty \left(1 - \frac{u}{u_e}\right) d\eta}{\int_0^\infty \left(1 - \frac{u}{u_e}\right)\frac{u}{u_e} d\eta} = \frac{H - 0.290\, M_e^2}{1 + 0.113\, M_e^2} \tag{B.12}$$

and used by Drela in his most of his closure relations to account for compressible effects.

The additional effects of stream surface radius, streamtube convergence and rotation are included in the right-hand sides of equations B.9 and B.10. The streamtube convergence has a relatively strong effect on the boundary layer as a result of the new term

db/ds in the integral momentum equation. Rotational effects have a relatively small influence, but affect both the momentum equation and the shape parameter equation.

The amplification equation and the dissipation lag equation are fortunately unaffected by r, b and Ω terms. Additionally, the laminar and turbulent closure relations for shape parameters, skin friction and dissipation were used unchanged from Drela's derivation [9], although the current implementation of the boundary layer differs somewhat from that in his thesis as a result of later work [13] that addressed the effects of thick blade trailing edges. Wall quantities for the boundary layer, such as ρ_{0e}, M_e, T_e/T_0 are defined using rothalpy **I** rather than enthalpy.

B.2.1 Inviscid/Viscous Coupling

The coupling between the boundary layer and the displacement surface is altered slightly for the quasi-3D treatment. The boundary layer is calculated in dimensional quantities for the integral thicknesses using the dimensional surface length and velocity. The presence of the boundary layer modifies the solid wall boundary condition by displacing the stagnation streamline outward from the blade by the boundary layer thickness. The surface streamline is displaced Δn_i in the non-dimensional $m' - \theta$ coordinates of the blade by

$$\Delta n_i = \frac{\delta_i^*}{r_i} \tag{B.13}$$

Appendix C
Cascade Loss Calculation

As discussed in Chapter 2, losses through a cascade result from inviscid shock losses and viscous dissipation in the blade boundary layers. This is manifested as a reduction of the stagnation pressure from the equivalent isentropic value at the outlet, assuming adiabatic flow. The loss coefficient ω, is defined as the loss in stagnation pressure in the exit flow non-dimensionalized by the inlet dynamic pressure.

$$\omega = \frac{p_{0_{2_{isen}}} - \bar{p}_{0_2}}{p_{0_1} - p_1} \tag{C.1}$$

where $p_{0_{2_{isen}}}$ is the isentropic (lossless) exit stagnation pressure and $\bar{p}_{0_2}$ is the mass-averaged exit stagnation pressure. The isentropic stagnation pressure evaluated at the exit is

$$p_{0_{isen}} = \frac{\gamma - 1}{\gamma} h_0 \rho_{0_{ref}} \left(\frac{h_0}{\mathbf{I}}\right)^{\frac{1}{\gamma-1}} \qquad \text{where } h_0 = \mathbf{I} + \frac{(\Omega r)^2}{2} \tag{C.2}$$

The mass-averaged total pressure is defined by integrating total pressure with respect to mass flow at the exit.

$$\omega = \frac{p_{0_{2_{isen}}} - \int_0^{\dot{m}} p_{0_2} \frac{d\dot{m}}{\dot{m}}}{p_{0_1} - p_1} \tag{C.3}$$

The integration variable here is $d\dot{m} = \rho u\, b\, dy$, the incremental mass flux at the outlet, with b as the streamtube width. This definition is used for losses in rotors as well as stators.

In MISES a zonal approach is used to solve the viscous flow indirectly. An equivalent inviscid flow, EIF, is postulated with a displacement surface to represent the viscous layer. The EIF is defined such that it is locally irrotational and contains all the mass flow, while the viscous effects are modeled by the mass flow defect. As a result, the inviscid and viscous loss contributions must be calculated over their respective domains - inviscid shock losses are given by the streamtubes defining the EIF, while viscous losses

are calculated as a defect contribution from the wake boundary layer at the cascade exit where the flow has, at least partially, mixed out. This calculation takes the form of C.1 with $\bar{p}_{0_2}$ defined by the two contributions at the exit plane

$$\bar{p}_{0_2} = \left[\int_0^{\dot{m}} p_0 \frac{d\dot{m}}{\dot{m}}\right]_{EIF} - \left[\int_0^{\dot{m}} (p_{0_e} - p_0) \frac{d\dot{m}}{\dot{m}}\right]_{BL} \tag{C.4}$$

C.1 Inviscid Loss Calculation

Inviscid losses are defined directly by the integral in C.3. The total pressure in the EIF is related to the local density and stagnation enthalpy by,

$$p_0 = \frac{\gamma - 1}{\gamma} \rho_0 \, h_0 \tag{C.5}$$

The inviscid losses are given by,

$$\omega_{invis} = \frac{\int_0^{\dot{m}} \frac{\gamma - 1}{\gamma} \, h_0 \, (\rho_{0_{isen}} - \rho_{0_2}) \frac{d\dot{m}}{\dot{m}}}{p_{0_1} - p_1} \tag{C.6}$$

where the stagnation density evaluated at the exit, using the stagnation enthalpy $h_0 = \mathrm{I} + \frac{(\Omega r)^2}{2}$ and local density and velocity, is

$$\rho_{0_2} = \rho_2 \left(1 - \frac{q_2^2}{2 \, h_0}\right)^{-\frac{1}{\gamma - 1}} \tag{C.7}$$

The isentropic stagnation density evaluated at the exit is

$$\rho_{0_{isen}} = \rho_{0_{ref}} \left(\frac{h_0}{\mathrm{I}}\right)^{\frac{1}{\gamma - 1}} \tag{C.8}$$

C.2 Viscous Loss Calculation

The viscous losses should ideally be evaluated far downstream where the flow has mixed out to a uniform condition. As an approximation to the fully mixed out condition the loss can be evaluated at the exit boundary where the wake boundary layer is reasonably well developed. Downstream, the wake shape factor $H \rightarrow 1$, implying that the velocity defect $\delta u = u_e - u$ is small. This will certainly be a good approximation for unseparated

flows and will be less valid as the extent of flow separation increases to the point where the wake cannot fully develop in the cascade exit length.

The total pressure in the boundary layer depends on p, u and h_0.

$$p_0 = p \left(1 - \frac{u^2}{2\ h_0}\right)^{-\frac{\gamma}{\gamma-1}} \tag{C.9}$$

It is assumed that h_0 is constant in the boundary layer, limiting this treatment to adiabatic flows. In the boundary layer $p = p_e$, so that C.9 can be linearized for small perturbations from the edge conditions (ρ_e, u_e) to give an expression for the total pressure defect,

$$\delta p_0 = \frac{\gamma}{\gamma - 1}\ p_e \left(1 - \frac{u_e^2}{2\ h_0}\right)^{\frac{1-2\gamma}{\gamma-1}} \frac{u_e}{h_0}\ \delta u \tag{C.10}$$

which reduces to,

$$\delta p_0 = \frac{p_{0_e}}{p_e} \rho_e u_e \delta u \tag{C.11}$$

The total pressure defect is integrated with respect to mass flux across the boundary layer to give,

$$\int_0^{\dot{m}} \delta p_0 d\dot{m} = \frac{p_{0_e}}{p_e} \rho_e u_e\ b \int_0^{y_{pitch}} \rho u (u_e - u)\, r\, dy \tag{C.12}$$

where r and b are the streamtube radius and width at the exit plane. The last integral is recognized as simply $\rho_e u_e^2\ \theta$ from B.4 so that the mass-averaged loss in the viscous layer is,

$$\omega_{visc} = \frac{\int \delta p_0 \frac{d\dot{m}}{\dot{m}}}{p_{0_1} - p_1} = \frac{\frac{p_{0_e}}{p_e} \frac{\rho_e u_e}{\dot{m}}\ b\ \rho_e u_e^2\, \theta}{p_{0_1} - p_1} \tag{C.13}$$

where θ is defined by the integral BL and ρ_e, u_e is defined by the EIF.

The viscous loss calculation assumes near-unity wake shape factors. The sensitivity of the loss to the outlet length and exit shape factor is shown in Table C.1. The outlet length is measured from the blade trailing edge to the exit plane and is non-dimensionalized by blade chord. The test case was the DFVLR cascade at $M = 0.82$, $R_n = 1.4 \times 10^6$ with no flow separation. The calculated loss levels are not particularly sensitive to the exit length, and hence degree of mixing, even very close to the trailing edge for wake shape factors of almost 1.7.

Table C.1: Loss as a function of outlet length

Outlet length	ω	ω_{invis}	ω_{visc}	H_{exit}
0.25	0.0310	0.00720	0.0239	1.677
0.50	0.0309	0.00715	0.0238	1.196
1.00	0.0310	0.00717	0.0238	1.055
2.00	0.0309	0.00714	0.0238	1.027

C.3 Loss at Uniform Exit Condition

The combined inviscid and viscous losses have been calculated by mass-averaging at the exit plane of the computational domain. The following conservation scheme can be used to extrapolate the mass-averaged flow quantities to a hypothetical fully mixed out flow downstream.

The mass flow, total momentum components and enthalpy are known at the mass-averaging plane, referred to using $()_2$ subscripts. Conditions at the fully mixed condition are denoted by $()_3$. Conservation of mass, momentum and energy at the two planes give

$$\begin{aligned}
\rho_3 q_{x_3} \tilde{s}_3 b_3 &= \rho_2 \bar{q}_{x_2} \tilde{s}_2 b_2 - \dot{m} \\
\dot{m} q_{y_3} &= \dot{m} \bar{q}_{y_2} \\
\dot{m} q_{x_3} + p_3 \tilde{s}_3 b_3 &= \dot{m} \bar{q}_{x_2} + \bar{p}_2 \tilde{s}_2 b_2 \\
\frac{\gamma}{\gamma - 1} \frac{p_3}{\rho_3} + \frac{q_3^2}{2} &= \frac{\gamma}{\gamma - 1} \frac{\bar{p}_2}{\bar{\rho}_2} + \frac{\bar{q}_2^2}{2} = h_0
\end{aligned} \tag{C.14}$$

where $\tilde{s} = r\, y_{pitch}$ is the physical cascade pitch at r and b is the streamtube width. The fixed quantities are $\dot{m}$ and h_0, which are constant at all stations, and the radius r_3 and width b_3 at the mixed-out plane. The mass-averaged quantities $\bar{q}_2$ and $\bar{p}_2$, and the exit angle β_2 are known from the flow calculation. The mass-averaged velocity is given from the momentum integral over the inviscid outer flow and a momentum defect integral over the boundary layer at the exit.

$$\bar{q}_2 = \int_0^{\dot{m}} u \frac{d\dot{m}}{\dot{m}}$$

$$
\begin{aligned}
&= \left[\int_0^{\dot{m}} u \frac{d\dot{m}}{\dot{m}}\right]_{EIF} - \frac{b}{\dot{m}}\left[\int_0^{y_{pitch}} \rho u(u_e - u)\, r\, dy\right]_{BL} \\
&= \left[\int_0^{\dot{m}} u \frac{d\dot{m}}{\dot{m}}\right]_{EIF} - \frac{\rho_e u_e^2 b\, \theta}{\dot{m}}
\end{aligned} \tag{C.15}
$$

A simple mass-averaging in the EIF suffices for defining $\bar{p}_2$. The exit angle β_2 is given by a global unknown, either specified or part of the solution. The x and y components of $\bar{q}_2$ are defined using the exit angle β_2. This system defines four equations in four unknowns, so the solution is straightforward.

$$
\begin{aligned}
q_{y_3} &= \bar{q}_{y_2} \\
\rho_3 &= \frac{\dot{m}}{\tilde{s}_3\, b_3 q_{x3}} \\
p_3 &= \frac{p_2\, \tilde{s}_2\, b_2 + \dot{m}\,(\bar{q}_{x_2} - q_{x_3})}{\tilde{s}_3\, b_3} \\
\beta_3 &= \arctan \frac{q_{y_3}}{q_{x_3}}
\end{aligned} \tag{C.16}
$$

where q_{x_3} is defined by the solution to the quadratic

$$
q_{x_3}^2 \left[\frac{\gamma + 1}{2\,(1 - \gamma)}\right] + q_{x_3}\left[\frac{\gamma}{\gamma - 1}\frac{\dot{m}\bar{q}_{x_2} + \bar{p}_2 \tilde{s}_2\, b_2}{\dot{m}}\right] + \frac{\bar{q}_{y_2}^2}{2} - h_0 = 0 \tag{C.17}
$$

The loss in the mixed-out flow is defined using the mixed out total pressure

$$
p_{0_3} = p_3 \left(\frac{h_0}{h_0 - \frac{q_3^2}{2}}\right)^{\frac{\gamma}{\gamma - 1}} \tag{C.18}
$$

in place of $\bar{p}_{0_2}$ in the loss equation C.1. The loss defined using this approach normally differs only slightly from the mass-averaged result.

C.4 Loss Sensitivity Calculation

One of the useful byproducts of using a Newton solution procedure is the Jacobian matrix **J** that is generated and inverted for each Newton step. The Jacobian defines the sensitivity of the solution with respect to the grid, density and global unknowns. This information can also be used to to calculate the sensitivity of any flow dependent quantity, such as the loss coefficient $\omega = f(n, \rho)$, to the global variables. The global variables can include the global parameters such as inlet angle or Mach number, exit pressure or geometric design modes that perturb all, or part of, the blade surface. This opens the door to a host of interesting possibilities for design optimization.

The linear system for the Newton procedure has the form

$$\left[\begin{array}{c|c} \mathbf{J}' & \mathbf{h} \\ \hline \mathbf{G}_{n,\rho} & \mathbf{G}_g \end{array}\right] \left\{\begin{array}{c} \delta\mathbf{n} \\ \delta\boldsymbol{\rho} \\ \hline \delta\mathbf{g} \end{array}\right\} = \left\{\begin{array}{c} -\mathbf{R}' \\ \hline -\mathbf{R}_g \end{array}\right\} \tag{C.19}$$

where the unknown vector contains the Euler flow field unknowns $\delta\mathbf{n}$, $\delta\boldsymbol{\rho}$, and the global unknowns $\delta\mathbf{g}$. The Jacobian matrix **J** is composed of flow equation rows $(\mathbf{J}' + \mathbf{h})$ and global equation rows $(\mathbf{G}_{n,\rho} + \mathbf{G}_g)$. The vector $\mathbf{R}'$ is the residual for the flow equations, $\mathbf{R}_g$ is the residual for the global constraint equations.

The flow equations are tightly banded with respect to the flow variables but not with respect to the global variables. This linear system is most efficiently solved by rearranging the columns corresponding to the global variables to the right-hand side to get

$$\left[\begin{array}{c} \mathbf{J}' \end{array}\right] \left\{\begin{array}{c} \delta\mathbf{n} \\ \delta\boldsymbol{\rho} \end{array}\right\} = \left\{-\mathbf{R}'\right\} + \delta g_1 \left\{-\mathbf{h}_1\right\} \cdots + \delta g_m \left\{-\mathbf{h}_m\right\} \tag{C.20}$$

where the right-hand side consists the flow variable residuals, $\mathbf{R}'$, and the **h** global variable columns. The global equations define a second, much smaller system

$$\mathbf{G}_{n,\rho} \left\{\begin{array}{c} \delta\mathbf{n} \\ \delta\boldsymbol{\rho} \end{array}\right\} + \mathbf{G}_g \delta\mathbf{g} = -\mathbf{R}_g \tag{C.21}$$

The system of flow equations C.20 is solved by elimination to obtain a partially-determined solution.

$$\begin{Bmatrix} \delta \mathbf{n} \\ \\ \delta \rho \end{Bmatrix} = \begin{Bmatrix} \delta \tilde{\mathbf{n}} \\ \\ \delta \tilde{\rho} \end{Bmatrix} + \delta g_1 \begin{Bmatrix} \tilde{\mathbf{h}}_1 \\ \\ \end{Bmatrix} \cdots + \delta g_m \begin{Bmatrix} \tilde{\mathbf{h}}_m \\ \\ \end{Bmatrix} \tag{C.22}$$

where the vectors $\delta \tilde{\mathbf{n}}$ and $\delta \tilde{\rho}$ are the flow solution without the effect of the global variables and $\tilde{\mathbf{h}}_k$ are the vectors of sensitivities of flow variables to the global unknowns.

$$\tilde{\mathbf{h}}_k = \begin{Bmatrix} \frac{\partial n}{\partial g_k} \\ \\ \frac{\partial \rho}{\partial g_k} \end{Bmatrix} \tag{C.23}$$

The solution is obtained by solving the small global system C.21 using the partially determined solution $\delta \tilde{\mathbf{n}}$ and $\delta \tilde{\rho}$.

$$\left[\mathbf{G}_{n,\rho} \left(\tilde{\mathbf{h}}_1 \cdots \tilde{\mathbf{h}}_m \right) + \mathbf{G}_g \right] \delta \mathbf{g} = -\mathbf{R}_g - \mathbf{G}_{n,\rho} \begin{Bmatrix} \delta \tilde{\mathbf{n}} \\ \delta \tilde{\rho} \end{Bmatrix} \tag{C.24}$$

The flow unknowns $\delta \mathbf{n}$ and $\delta \rho$ are determined from the partial solution using the global variables $\delta \mathbf{g}$ and the $\tilde{\mathbf{h}}$ vectors.

The components of the $\tilde{\mathbf{h}}$ vectors can be used to calculate the sensitivity of the loss coefficient $\omega(n, \rho)$ to a global variable change. The sensitivity is obtained by linearizing the loss w.r.t. the flow unknowns, generating the vectors $\partial \omega / \partial \rho_i$ and $\partial \omega / \partial n_i$. The sensitivity to the global unknowns is given by

$$\frac{\partial \omega}{\partial g_k} = \sum_i \frac{\partial \omega}{\partial n_i} \frac{\partial n_i}{\partial g_k} + \sum_i \frac{\partial \omega}{\partial \rho_i} \frac{\partial \rho_i}{\partial g_k} \tag{C.25}$$

Note that the sensitivity of any flow dependent quantity, such as mass flow or turning, could also be linearized in this manner.

Unfortunately the global unknowns are not, in general, orthogonal with respect to one another so that the effect of a perturbation in a single global variable on the set of global unknowns must be accounted for. Using the small global matrix system C.24, each global variable δg_j is in turn perturbed by replacing its regular constraint equation with $\delta g_j = 1$. The right hand sides of the remaining rows are cleared and the global system is solved for the resulting vector of perturbations to the global unknowns δg_k.

This is the response of the global unknowns to a single unit global variable change δg_j. The linearized loss sensitivity to a global variable change is defined by the inner product

$$\frac{\delta \omega}{\delta g_j} = \sum_j \frac{\partial \omega}{\partial g_k} \frac{\delta g_k}{\delta g_j} \tag{C.26}$$

This procedure is repeated for each desired sensitivity.

The linearized loss sensitivity strictly only applies in the vicinity of the point at which it was generated, so that some caution must be used in interpreting this information for design changes using the modal redesign feature. Experience shows that the sensitivity can be used as a guide to a steepest descent optimization, provided sufficiently small changes are introduced. The sensitivity information is only valid near convergence of the Newton system so that the best strategy is to introduce a modest change, guided by the calculated optimization direction, and run for several Newton cycles and reevaluate. One of the difficulties associated with this design strategy is that it tends to lead to "point optimizations" rather than robust designs.

Appendix D
Matrices and Linear System Solution

The theory and numerical implementation of the quasi-3D flow solver has been described in previous chapters and appendices. This appendix includes details of the Jacobian matrices generated by the Newton system and the approach used for solving the linear system. Modifications to the basic scheme for multiple blades and offset-periodic grids are discussed.

D.1 Newton System

As introduced in chapter 3 the inviscid flow is solved with the steady-state Euler equations discretized on a streamline grid, see Figure D.1. A Newton-Raphson solution

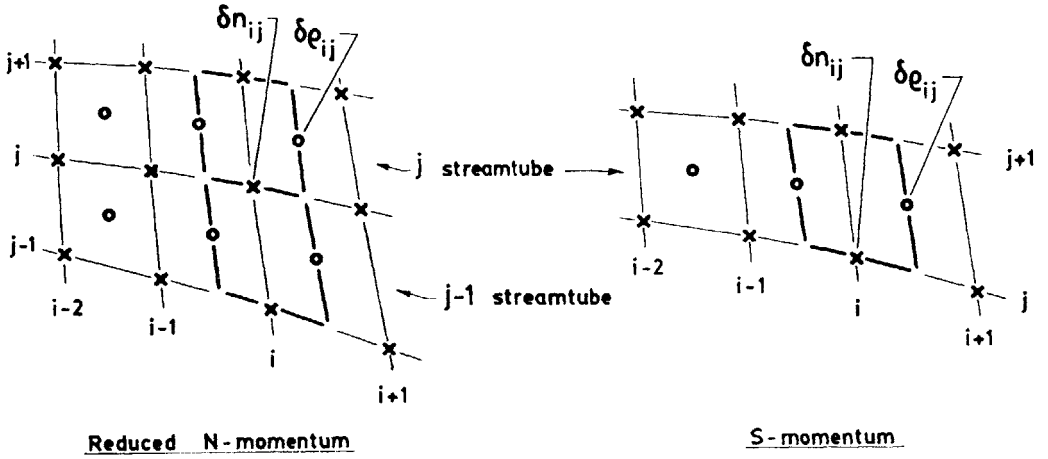

Figure D.1: Newton variables for discrete Euler equations.

technique is used to iteratively solve the resulting non-linear equations. As a result of the streamline approach, only streamwise convection terms are present, effectively

reducing the system of equations to a streamwise, or S-momentum equation at conservation cell centers in each streamtube and a normal momentum (reduced N-momentum) equation at nodes on each streamline. The Jacobian system is constructed by taking variations of these equations with respect to each of flow and geometric variables. These variations are compactly expressed in terms of one unknown Newton variable for each equation, a perturbation to the streamtube cell density $\delta\rho$ and a perturbation to the streamline normal node displacement δn, see Figure D.1.

A streamline grid is defined with streamwise index i and quasi-normal index j and is made up of (I nodes on each streamline) $\times J$ streamlines. The application of the discrete equations defines $I \times (J-1)$ S-momentum equations and $I \times J$ reduced N-momentum equations, which are efficiently arranged as I block rows of (2J-1) equations in each block. The $i = 1$ and $i = I$ block rows are used to apply the inlet and exit boundary conditions. Within each block, the $j = 1$ and $j = J$ rows are used apply periodicity conditions to the top and bottom streamlines.

The domain of dependence 'molecule' for the equations and variables on interior streamlines is shown in Figure D.2. The equations span four streamwise (i) nodes and

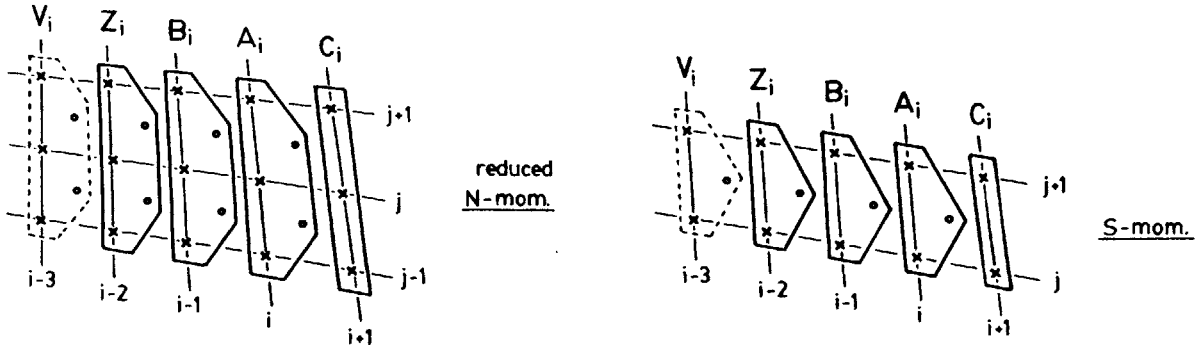

Figure D.2: Domain of dependence for S-momentum and N-momentum equations.

one streamtube for the S-mom. equation, two streamtubes for the N-mom. equation. The $\bar{\bar{\mathbf{Z}}}_i$ block dependence from nodes at $i-2$ results solely from the influence of the

upstream Mach number in the artificial dissipation and the influence of u_e in the BL equations. An additional $\bar{\bar{\mathbf{V}}}_i$ block, similar to the $\bar{\bar{\mathbf{Z}}}_i$ block but defined at node line $i-3$, is added if second-order dissipation is used.

Additional unknowns are often required that do not fit within the compact block structure of the interior equations. These global variables and associated global equations are specially treated in the solution process.

D.1.1 Jacobian Matrix

At each Newton iteration a linear system must be solved for the changes in density and streamline node displacement. The basic form of the block matrix system is

$$
\begin{bmatrix}
\bar{\bar{\mathbf{A}}}_1 & \bar{\bar{\mathbf{C}}}_1 & & & & & & & & & \bar{\bar{\mathbf{H}}}_1 \\
\bar{\bar{\mathbf{B}}}_2 & \bar{\bar{\mathbf{A}}}_2 & \bar{\bar{\mathbf{C}}}_2 & & & & & & & & \bar{\bar{\mathbf{H}}}_2 \\
\bar{\bar{\mathbf{Z}}}_3 & \bar{\bar{\mathbf{B}}}_3 & \bar{\bar{\mathbf{A}}}_3 & \bar{\bar{\mathbf{C}}}_3 & & & & & & & \bar{\bar{\mathbf{H}}}_3 \\
\bar{\bar{\mathbf{V}}}_4 & \bar{\bar{\mathbf{Z}}}_4 & \bar{\bar{\mathbf{B}}}_4 & \bar{\bar{\mathbf{A}}}_4 & \bar{\bar{\mathbf{C}}}_4 & & & & & & \bar{\bar{\mathbf{H}}}_4 \\
 & \cdot & \cdot & \cdot & \cdot & \cdot & & & & & \cdot \\
 & & \bar{\bar{\mathbf{V}}}_i & \bar{\bar{\mathbf{Z}}}_i & \bar{\bar{\mathbf{B}}}_i & \bar{\bar{\mathbf{A}}}_i & \bar{\bar{\mathbf{C}}}_i & & & & \bar{\bar{\mathbf{H}}}_i \\
 & & & \cdot & \cdot & \cdot & \cdot & \cdot & & & \cdot \\
 & & & & \bar{\bar{\mathbf{V}}} & \bar{\bar{\mathbf{Z}}} & \bar{\bar{\mathbf{B}}} & \bar{\bar{\mathbf{A}}} & \bar{\bar{\mathbf{C}}} & & \bar{\bar{\mathbf{H}}} \\
 & & & & & \bar{\bar{\mathbf{V}}} & \bar{\bar{\mathbf{Z}}} & \bar{\bar{\mathbf{B}}} & \bar{\bar{\mathbf{A}}} & \bar{\bar{\mathbf{C}}} & \bar{\bar{\mathbf{H}}} \\
 & & & & & & \bar{\bar{\mathbf{V}}}_I & \bar{\bar{\mathbf{Z}}}_I & \bar{\bar{\mathbf{B}}}_I & \bar{\bar{\mathbf{A}}}_I & \bar{\bar{\mathbf{H}}}_I \\
-- & -- & -- & -- & -- & -- & -- & -- & -- & -- & -- \\
\bar{\bar{\mathbf{G}}}_1 & \bar{\bar{\mathbf{G}}}_2 & \bar{\bar{\mathbf{G}}}_3 & \cdot & \bar{\bar{\mathbf{G}}}_i & \cdot & \cdot & \cdot & \cdot & \bar{\bar{\mathbf{G}}}_I & \bar{\bar{\mathbf{G}}}_g
\end{bmatrix}
\times
\begin{bmatrix} \bar{\delta}_1 \\ \bar{\delta}_2 \\ \bar{\delta}_3 \\ \bar{\delta}_4 \\ \cdot \\ \bar{\delta}_i \\ \cdot \\ \bar{\delta} \\ \bar{\delta} \\ \bar{\delta}_I \\ -- \\ \bar{\delta}_g \end{bmatrix}
=
\begin{bmatrix} -\bar{\mathbf{R}}_1 \\ -\bar{\mathbf{R}}_2 \\ -\bar{\mathbf{R}}_3 \\ -\bar{\mathbf{R}}_4 \\ \cdot \\ -\bar{\mathbf{R}}_i \\ \cdot \\ -\bar{\mathbf{R}} \\ -\bar{\mathbf{R}} \\ -\bar{\mathbf{R}}_I \\ -- \\ -\bar{\mathbf{R}}_g \end{bmatrix}
\qquad \text{(D.1)}
$$

The linear system is arranged in I blocks of dimension 2J-1, where each block has an unknown vector $\bar{\delta}_i = (\delta n_{i,1\to J},\ \delta\rho_{i,1\to J-1})$. $\bar{\mathbf{R}}_i$ is the Newton residual for the S-mom. and N-mom. equations. The vector of global unknowns, $\bar{\delta}_g$, is associated with the global equations, made up of $\bar{\bar{\mathbf{G}}}_i$ entries for the $\delta\rho$ and δn unknowns, and $\bar{\bar{\mathbf{G}}}_g$ entries for the global unknowns. The $\bar{\bar{\mathbf{H}}}_i$ blocks represent the effect of the global unknowns on the S-mom. and N-mom. equations.

D.1.2 Block Structure

The component blocks for the interior equations in D.1 are shown in Figures D.3 and D.4. Periodic conditions for pressure and geometry are enforced by the first and last rows in

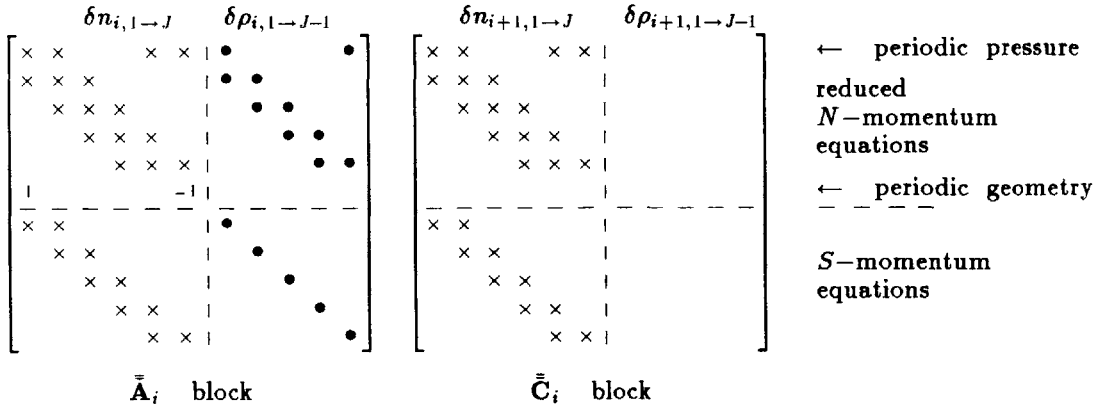

Figure D.3: Structure of $\bar{\bar{A}}_i$ and $\bar{\bar{C}}_i$ blocks.

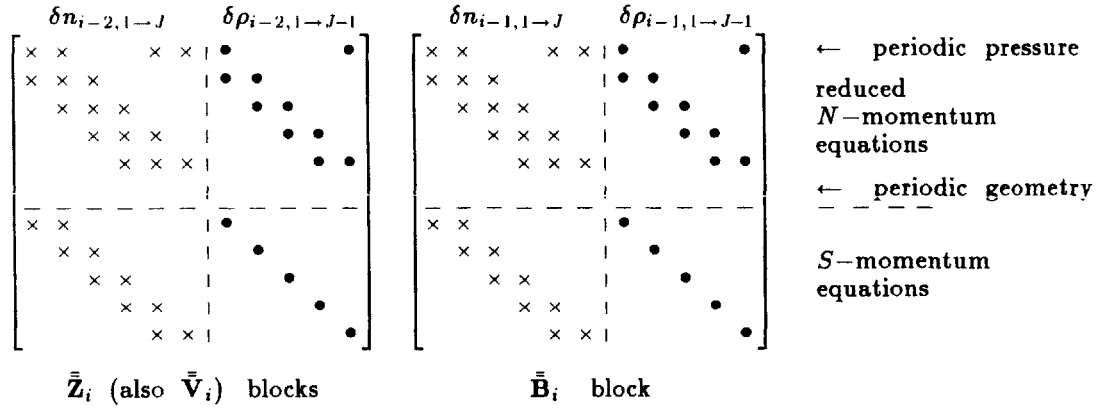

Figure D.4: Structure of $\bar{\bar{Z}}_i$ and $\bar{\bar{B}}_i$ blocks.

the upper sub-block corresponding to δn unknowns. Geometric continuity is imposed by the identity condition in the $\bar{\bar{A}}_i$ block only. Note that the periodic pressure condition introduces two node displacement entries and one density entry for the corresponding periodic streamline (i.e. streamline 1 is coupled to streamline J, involving streamtubes 1 and J-1). The geometric continuity condition introduces only one 'off diagonal' entry. For a solid surface BC, such as over a blade surface, the periodic pressure and geometric

rows are cleared and are replaced by 1 on the diagonal.

The blocks corresponding to the inlet conditions are defined in Figure D.5. At the

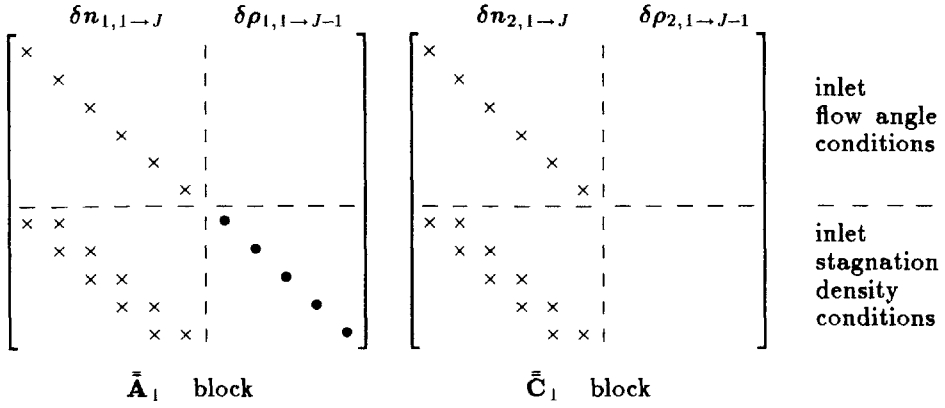

Figure D.5: Structure of inlet blocks.

inlet, only the $\bar{\bar{\mathbf{A}}}_1$ and $\bar{\bar{\mathbf{C}}}_1$ blocks are present. These implement linearized slope or inlet characteristic conditions in the upper sub-blocks and linearized stagnation density conditions in the lower sub-blocks.

The blocks for the last line of grid nodes at $i = I$ implement the exit conditions and are defined in Figure D.6. At the exit, only blocks $\bar{\bar{\mathbf{V}}}_I$ through $\bar{\bar{\mathbf{A}}}_I$ are present.

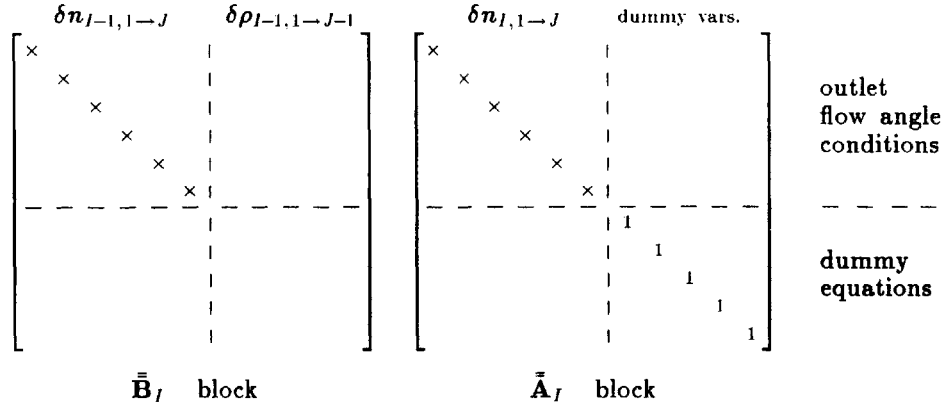

Figure D.6: Structure of exit blocks.

The upper sub-blocks implement the linearized exit slope boundary conditions. Density variables are not defined at $i = I$ so the lower sub-blocks contain dummy equations.

D.1.3 Matrix Blocks with Boundary Layer

For viscous flows each surface boundary layer is represented using integral boundary layer equations which are solved simultaneously with the inviscid outer flow. The details of the boundary layer discretization are best covered in Reference [9]. Modifications to the ISES methodology for quasi-3D flow are discussed in Appendix B.

The boundary layer adds three equations and three unknowns to the Newton system for every node on each surface streamline. The new unknowns correspond to $\delta C_\tau^{1/2}$, $\delta\theta$ and $\delta(\delta^*)$ for the wall streamline. The boundary layer solution is driven by the edge velocity and density, defined in terms of the unknowns for the streamtube at the wall. The domain of dependence 'molecule' for the viscous variables is shown in Figure D.7.

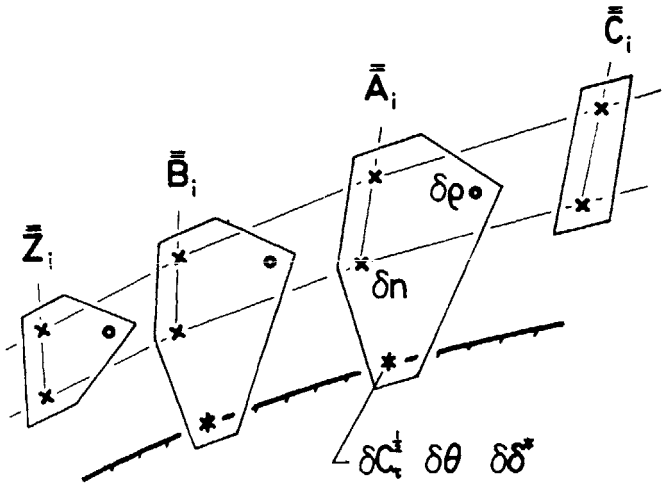

Figure D.7: Domain of dependence of boundary layer unknowns, from Drela.

An $\bar{\bar{\mathbf{A}}}_i$ block with boundary layer coupling conditions takes the form

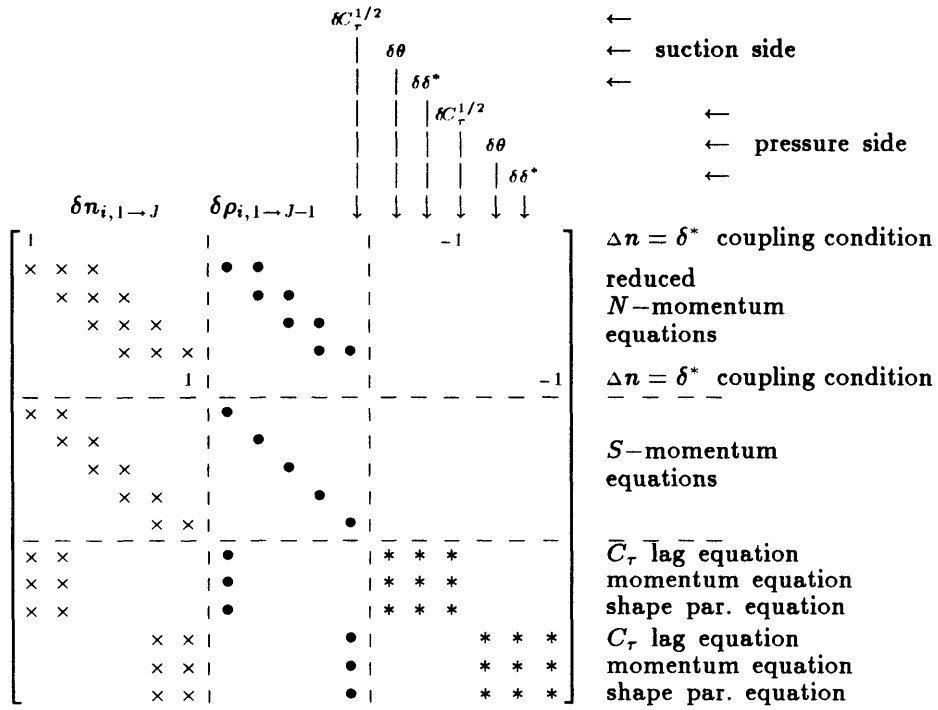

On the periodic inlet streamline, where no boundary layer is present, the boundary layer entries are cleared and the diagonal entries set to one.

Wake boundary layers are handled somewhat differently – the upper and lower surface boundary layer unknowns are merged at the trailing edge and the wake is treated as a single boundary layer. Dummy equations are used as placeholders in the unused BL rows. The pressure and geometric continuity conditions, from D.3, are imposed with the geometric continuity condition modified to include the wake thickness between the periodic streamlines.

D.2 Solution of Linear System

The linear system D.1 is solved by treating it as two linear problems, a banded block system and a smaller, full linear system for global unknowns. The original system can be rewritten as

$$\begin{bmatrix}
\bar{\bar{\mathbf{A}}}_1 & \bar{\bar{\mathbf{C}}}_1 & & & & & & & \\
\bar{\bar{\mathbf{B}}}_2 & \bar{\bar{\mathbf{A}}}_2 & \bar{\bar{\mathbf{C}}}_2 & & & & & & \\
\bar{\bar{\mathbf{Z}}}_3 & \bar{\bar{\mathbf{B}}}_3 & \bar{\bar{\mathbf{A}}}_3 & \bar{\bar{\mathbf{C}}}_3 & & & & & \\
\bar{\bar{\mathbf{V}}}_4 & \bar{\bar{\mathbf{Z}}}_4 & \bar{\bar{\mathbf{B}}}_4 & \bar{\bar{\mathbf{A}}}_4 & \bar{\bar{\mathbf{C}}}_4 & & & & \\
 & \cdot & \cdot & \cdot & \cdot & \cdot & & & \\
 & & \bar{\bar{\mathbf{V}}}_i & \bar{\bar{\mathbf{Z}}}_i & \bar{\bar{\mathbf{B}}}_i & \bar{\bar{\mathbf{A}}}_i & \bar{\bar{\mathbf{C}}}_i & & \\
 & & & \cdot & \cdot & \cdot & \cdot & \cdot & \\
 & & & & \bar{\bar{\mathbf{V}}} & \bar{\bar{\mathbf{Z}}} & \bar{\bar{\mathbf{B}}} & \bar{\bar{\mathbf{A}}} & \bar{\bar{\mathbf{C}}} \\
 & & & & & \bar{\bar{\mathbf{V}}} & \bar{\bar{\mathbf{Z}}} & \bar{\bar{\mathbf{B}}} & \bar{\bar{\mathbf{A}}} \\
 & & & & & & \bar{\bar{\mathbf{V}}}_I & \bar{\bar{\mathbf{Z}}}_I & \bar{\bar{\mathbf{B}}}_I & \bar{\bar{\mathbf{A}}}_I
\end{bmatrix} \times \begin{bmatrix} \bar{\boldsymbol{\delta}}_1 \\ \bar{\boldsymbol{\delta}}_2 \\ \bar{\boldsymbol{\delta}}_3 \\ \bar{\boldsymbol{\delta}}_4 \\ \cdot \\ \bar{\boldsymbol{\delta}}_i \\ \cdot \\ \bar{\boldsymbol{\delta}} \\ \bar{\boldsymbol{\delta}} \\ \bar{\boldsymbol{\delta}}_I \end{bmatrix} = \begin{bmatrix} -\bar{\mathbf{R}}_1 \\ -\bar{\mathbf{R}}_2 \\ -\bar{\mathbf{R}}_3 \\ -\bar{\mathbf{R}}_4 \\ \cdot \\ -\bar{\mathbf{R}}_i \\ \cdot \\ -\bar{\mathbf{R}} \\ -\bar{\mathbf{R}} \\ -\bar{\mathbf{R}}_I \end{bmatrix} - \begin{bmatrix} \bar{\bar{\mathbf{H}}}_1 \\ \bar{\bar{\mathbf{H}}}_2 \\ \bar{\bar{\mathbf{H}}}_3 \\ \bar{\bar{\mathbf{H}}}_4 \\ \cdot \\ \bar{\bar{\mathbf{H}}}_i \\ \cdot \\ \bar{\bar{\mathbf{H}}} \\ \bar{\bar{\mathbf{H}}} \\ \bar{\bar{\mathbf{H}}}_I \end{bmatrix} \bar{\boldsymbol{\delta}}_g \qquad \text{(D.2)}$$

$$\bar{\bar{\mathbf{G}}}_1\bar{\boldsymbol{\delta}}_1 + \cdots + \bar{\bar{\mathbf{G}}}_i\bar{\boldsymbol{\delta}}_i + \cdots + \bar{\bar{\mathbf{G}}}_I\bar{\boldsymbol{\delta}}_I + \bar{\bar{\mathbf{G}}}_g\bar{\boldsymbol{\delta}}_g = -\bar{\mathbf{R}}_g \qquad \text{(D.3)}$$

where D.2 can be efficiently solved using a specialized block Gauss elimination algorithm, as described in Giles [15]. The banded system is solved for both the right-hand side residual vector $\bar{\mathbf{R}}$ and the additional right-hand columns of global influences on flow equations, $\bar{\bar{\mathbf{H}}}$. The resulting partially-determined solution is given by the vectors $\tilde{\boldsymbol{\delta}}$ and $\tilde{\mathbf{h}}$ such that the complete solution will be

$$\bar{\boldsymbol{\delta}}_i = \tilde{\boldsymbol{\delta}}_i - \tilde{\mathbf{h}}_i\bar{\delta}_g \qquad \text{(D.4)}$$

when $\bar{\delta}_g$ is determined. The small linear system is obtained by substituting D.4 into the global equation D.3. This gives a linear system in the global variables, typically of order 2 or 3 but up to ~ 12 for modal design applications.

$$[\,\bar{\bar{\mathbf{G}}}_g - \sum_i \bar{\bar{\mathbf{G}}}_i\tilde{\mathbf{h}}_i\,]\,\bar{\delta}_g = -\bar{\mathbf{R}}_g - \sum_i \bar{\bar{\mathbf{G}}}_i\tilde{\boldsymbol{\delta}}_i \qquad \text{(D.5)}$$

Substitution of $\bar{\delta}_g$ into D.4 gives the fully-determined solution.

D.2.1 Solution Method for Choked Flow

The banded matrix system in D.2 becomes increasingly ill-conditioned as the flow in the passage becomes choked, requiring modifications to the boundary conditions and solution procedure. As shown by Giles [15], the well-posed boundary condition for choked flow specifies the gradient of inlet stagnation density (which is equivalent to specifying the inlet vorticity) and the exit pressure. One of the remaining inlet boundary conditions must be dropped — either the mass flow or the inlet stagnation density. Since mass flow has been implicitly written into the momentum equations the inlet boundary condition on stagnation density is dropped.

The discrete form for the new inlet condition specifies the gradient of inlet stagnation density, usually set to zero. This is implemented by simply subtracting the inlet stagnation density conditions, equation 3.4, of neighboring streamtubes, i.e.

$$\rho_{0_{1,j}} - \rho_{0_{1,j+1}} = 0 \tag{D.6}$$

This produces $J-1$ inlet density equations, the missing equation consists of a mass-averaged exit pressure condition

$$\sum_{j=1}^{J-1} \frac{\dot{m}_j}{\dot{m}} p_{I-1,j} - p_{exit} = 0 \tag{D.7}$$

To maintain the banded structure of the matrix this equation must be moved to the $I-1$ block. A space is cleared in the $I-1$ block by shifting one of the S-momentum equations, at $j = j_{shift}$, up into the preceding block row, see Figure D.8. The corresponding equation in the $I-2$ row is shifted up into the $I-3$ row, etc. until the slot in the $I=1$ block is filled. Observing the $\bar{\bar{\mathbf{A}}}$ and $\bar{\bar{\mathbf{C}}}$ blocks in Figure D.3, note that only three new entries in the shifted row fall outside the existing diagonal block structure in $\bar{\bar{\mathbf{V}}} \rightarrow \bar{\bar{\mathbf{C}}}$. These entries are treated by the solver essentially as three extra right-hand sides, incurring a 10% penalty in solution cost.

Unfortunately the choked solution determines the inlet stagnation density for a given mass flow and exit pressure, rather than the mass flow for a given inlet stagnation density and exit pressure. To re-normalize the inlet stagnation density to the reference value

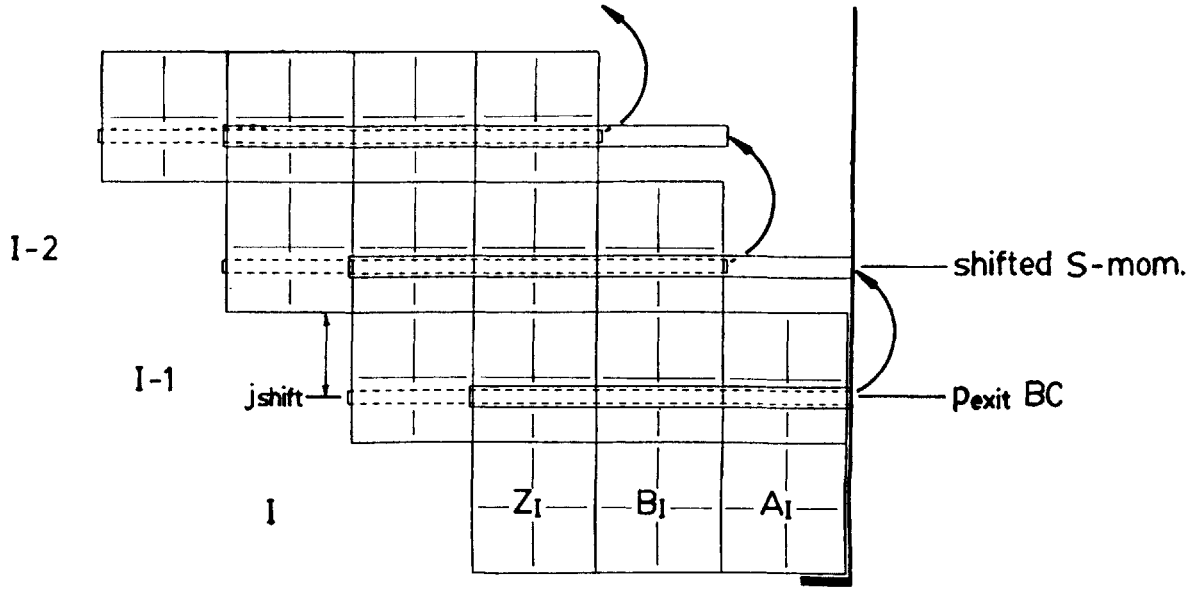

Figure D.8: Shifting of S-momentum equation rows for choked solver.

a DOF for mass flow is added to the system, constrained by an equation to drive the mass-averaged inlet stagnation density to the reference value.

$$\sum_{j=1}^{J-1} \frac{\dot{m}_j}{\dot{m}} \rho_{0_{i,j}} - \rho_{0_{ref}} = 0 \tag{D.8}$$

D.3 Multiple Blades

The application to multiple blades adds additional complexity, but no profound changes to the basic system. The effect of adding one or more additional blades is handled by treating the grid as a single large grid domain with embedded stagnation streamlines, which in effect separate it into N passages, where N is the total number of blades. Each stagnation streamline corresponds to two streamlines that define a *null streamtube* and whose points are co-located up to the leading edge of the blade, see Figure D.9.

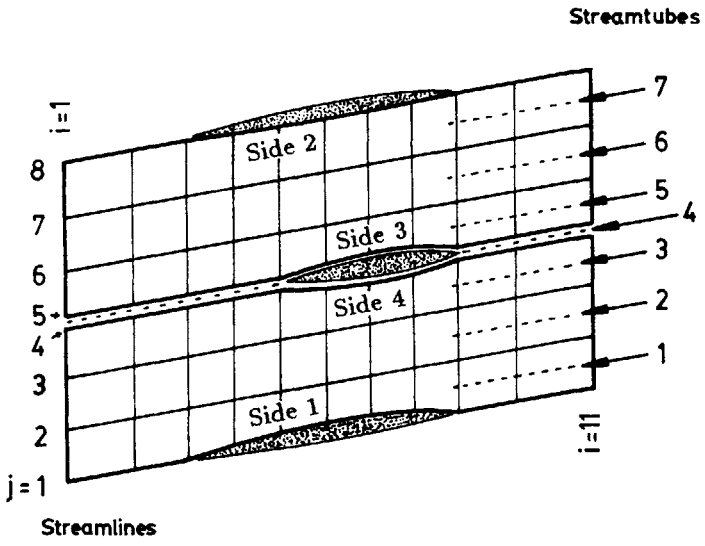

Figure D.9: Layout of streamtubes and streamlines in multiple blade grid

The basic arrangement of nodes, streamlines, equations and variables is unchanged, except that dummy equations replace the flow equations defining the densities in each null streamtube. Additional periodicity conditions must be enforced for pressure and geometric continuity across the collapsed streamtube. The domain of dependence 'molecule' for the equations and variables across the null streamtube is shown in Figure D.10. The S-momentum equation operates on a single streamtube and is unchanged. Note that the N-mom. equation spans *three* streamtubes in j.

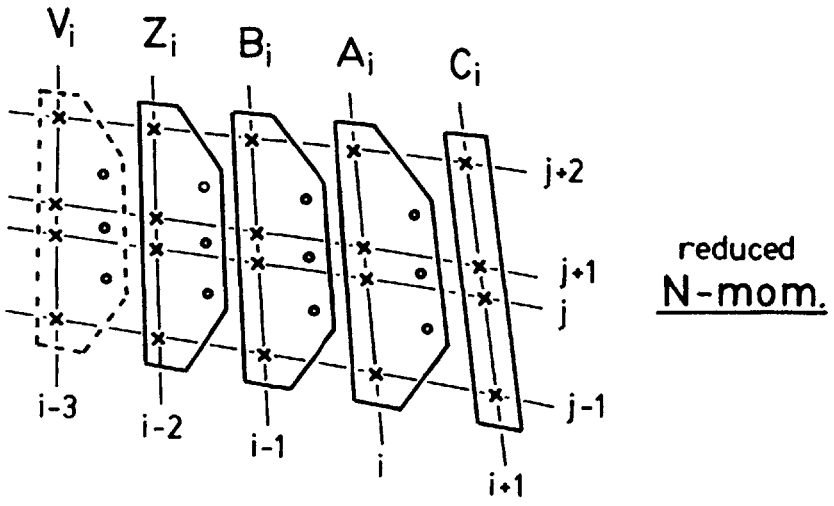

Figure D.10: Domain of dependence for reduced N-momentum equation across stagnation streamline.

D.3.1 Block Structure for Multiple blades

The basic structure for the Jacobian matrix blocks is modified to establish periodic conditions and dummy equations for the interior stagnation streamlines. The new structure for the $\bar{\bar{\mathbf{A}}}_i$ matrix block is

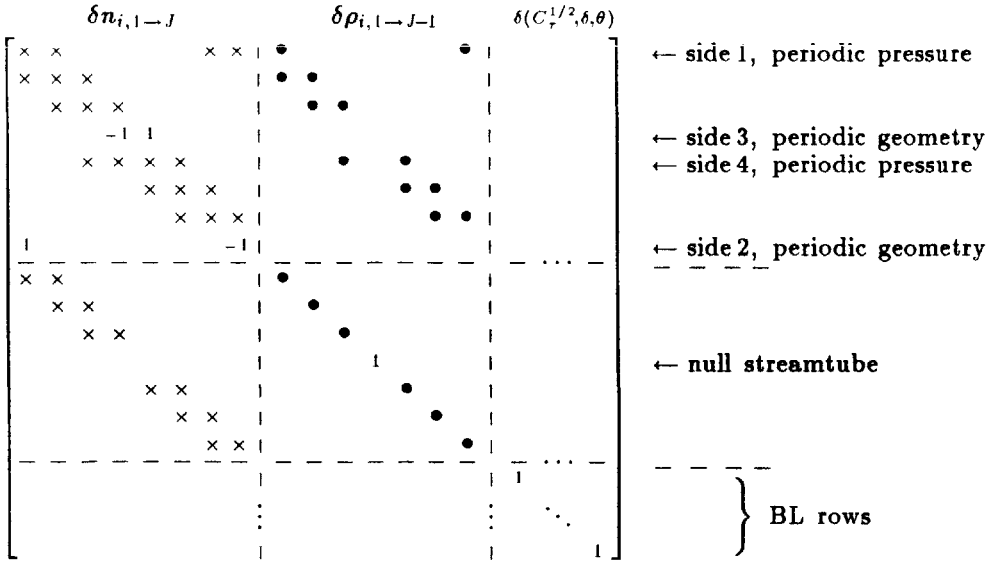

This block structure corresponds to the grid in Figure D.9 where streamtube 4 is the null streamtube, nestled around the intermediate blade. Note that this is a $\bar{\bar{\mathbf{A}}}_i$ block

for a station without boundary layers. Matrix blocks $\bar{\bar{\mathbf{V}}}_i$ through $\bar{\bar{\mathbf{C}}}_i$ are defined analogously, without the geometric continuity conditions. The periodic pressure condition for the intermediate blade is effectively the same as that used for the $j = 1$ and $j = J$ streamlines, but it applies across the null streamtube.

The modified $\bar{\bar{\mathbf{A}}}_i$ block with boundary layer coupling on both blades takes the form

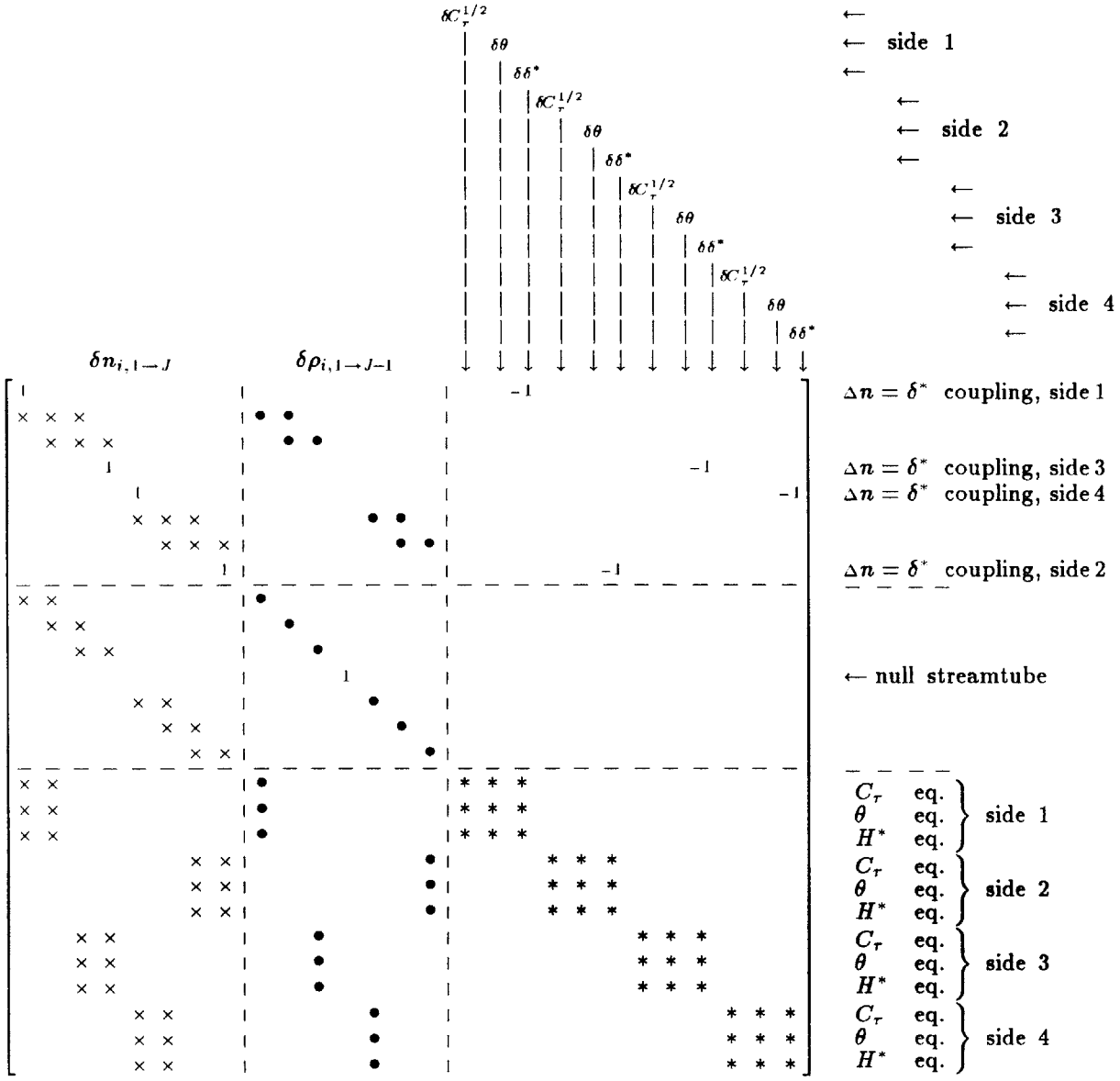

A case with N blades uses 6N boundary layer equations, increasing size of the block matrix. This increases the solution cost – a two blade solution is approximately 40% more work than a single blade case (for $J = 20$ streamlines).

D.3.2 Multiple Blade Choked Flow Solution

The choked flow solution procedure is modified for multiple blades by independently treating each passage. A shifted stream tube and p_{exit} condition D.7 are used for each passage. A mass flow or differential mass flow DOF is added for each passage and constrained by inlet stagnation density conditions D.8. The Kutta condition for the intermediate blade, usually constraining the differential mass flow, must be dropped as an explicit constraint and applied *implicitly* in the banded matrix by equating the upper and lower Π pressures at the trailing edge.

D.4 Offset-Periodic Matrix

A special grid topology using an offset-periodic inlet grid was introduced in Chapter 3 to reduce grid skew problems for supersonic Mach numbers. The inlet portion of the grid was constructed with quasi-normal lines roughly normal to the inflow, resulting in a 'stairstep' inlet boundary, see Figure D.11. Periodic conditions must now be enforced on matching points on the $j = 1$ and $j = J$ streamlines which are offset in streamwise index by a factor, i_{off} (note that $i_{off} = 6$ in the figure). The application of periodic pressure and geometry conditions leads to three pressure terms and one geometry term moving to off-diagonal blocks offset by i_{off}.

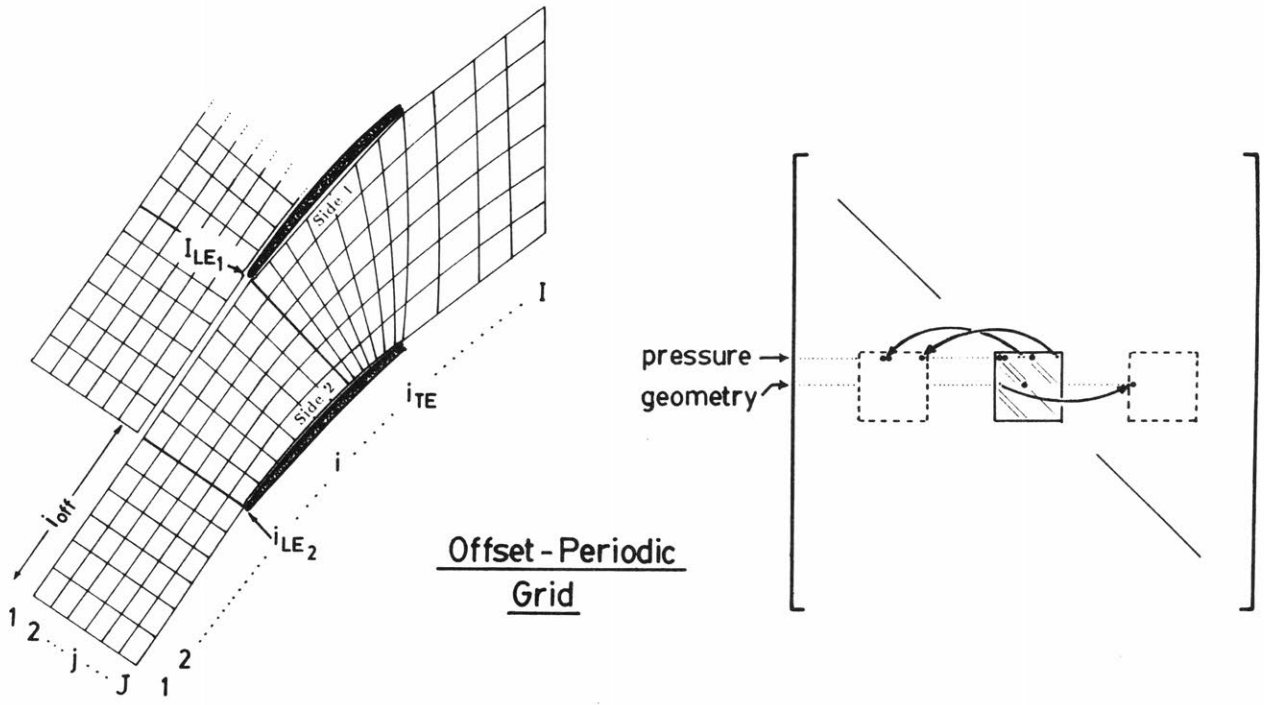

Figure D.11: Offset-periodic inlet geometry and indexing.

The block structure of the matrix for an offset-periodic grid has the form

$$
\begin{bmatrix}
\bar{\bar{\mathbf{A}}}_1 & \bar{\bar{\mathbf{C}}}_1 & & & & & & \bar{\bar{\mathbf{U}}}'_1 & & & & & & & & \\
\bar{\bar{\mathbf{B}}}_2 & \bar{\bar{\mathbf{A}}}_2 & \bar{\bar{\mathbf{C}}}_2 & & & & & & \bar{\bar{\mathbf{U}}}'_2 & & & & & & & \\
\bar{\bar{\mathbf{Z}}}_3 & \bar{\bar{\mathbf{B}}}_3 & \bar{\bar{\mathbf{A}}}_3 & \bar{\bar{\mathbf{C}}}_3 & & & & & & \cdot & & & & & & \\
\bar{\bar{\mathbf{V}}}_4 & \bar{\bar{\mathbf{Z}}}_4 & \bar{\bar{\mathbf{B}}}_4 & \bar{\bar{\mathbf{A}}}_4 & \bar{\bar{\mathbf{C}}}_4 & & & & & & \cdot & & & & & \\
 & \bar{\bar{\mathbf{V}}}_5 & \bar{\bar{\mathbf{Z}}}_5 & \bar{\bar{\mathbf{B}}}_5 & \bar{\bar{\mathbf{A}}}_5 & \bar{\bar{\mathbf{C}}}_5 & & & & & & \cdot & & & & \\
 & & \bar{\bar{\mathbf{V}}}_6 & \bar{\bar{\mathbf{Z}}}_6 & \bar{\bar{\mathbf{B}}}_6 & \bar{\bar{\mathbf{A}}}_6 & \bar{\bar{\mathbf{C}}}_6 & & & & & & \bar{\bar{\mathbf{U}}}'_6 & & & \\
 & & & \bar{\bar{\mathbf{V}}}_7 & \bar{\bar{\mathbf{Z}}}_7 & \bar{\bar{\mathbf{B}}}_7 & \bar{\bar{\mathbf{A}}}_7 & \bar{\bar{\mathbf{C}}}_7 & & & & & & & & \\
 & & & & \bar{\bar{\mathbf{V}}}_8 & \bar{\bar{\mathbf{Z}}}_8 & \bar{\bar{\mathbf{B}}}_8 & \bar{\bar{\mathbf{A}}}_8 & \bar{\bar{\mathbf{C}}}_8 & & & & & & & \\
\bar{\bar{\mathbf{B}}}'_9 & \bar{\bar{\mathbf{A}}}'_9 & \bar{\bar{\mathbf{C}}}'_9 & & & \bar{\bar{\mathbf{V}}}_9 & \bar{\bar{\mathbf{Z}}}_9 & \bar{\bar{\mathbf{B}}}_9 & \bar{\bar{\mathbf{A}}}_9 & \bar{\bar{\mathbf{C}}}_9 & & & & & & \\
\bar{\bar{\mathbf{Z}}}'_{10} & \bar{\bar{\mathbf{B}}}'_{10} & \bar{\bar{\mathbf{A}}}'_{10} & \bar{\bar{\mathbf{C}}}'_{10} & & & \bar{\bar{\mathbf{V}}}_{10} & \bar{\bar{\mathbf{Z}}}_{10} & \bar{\bar{\mathbf{B}}}_{10} & \bar{\bar{\mathbf{A}}}_{10} & \bar{\bar{\mathbf{C}}}_{10} & & & & & \\
\bar{\bar{\mathbf{V}}}'_{11} & \bar{\bar{\mathbf{Z}}}'_{11} & \bar{\bar{\mathbf{B}}}'_{11} & \bar{\bar{\mathbf{A}}}'_{11} & \bar{\bar{\mathbf{C}}}'_{11} & & & \bar{\bar{\mathbf{V}}}_{11} & \bar{\bar{\mathbf{Z}}}_{11} & \bar{\bar{\mathbf{B}}}_{11} & \bar{\bar{\mathbf{A}}}_{11} & \bar{\bar{\mathbf{C}}}_{11} & & & & \\
 & \cdot & \cdot & \cdot & \cdot & \cdot & & & \cdot & \cdot & \cdot & \cdot & \cdot & & & \\
 & & \bar{\bar{\mathbf{V}}}'_i & \bar{\bar{\mathbf{Z}}}'_i & \bar{\bar{\mathbf{B}}}'_i & \bar{\bar{\mathbf{A}}}'_i & \bar{\bar{\mathbf{C}}}'_i & & & \bar{\bar{\mathbf{V}}}_i & \bar{\bar{\mathbf{Z}}}_i & \bar{\bar{\mathbf{B}}}_i & \bar{\bar{\mathbf{A}}}_i & \bar{\bar{\mathbf{C}}}_i & & \\
 & & & & & & & & & & \cdot & \cdot & \cdot & \cdot & \cdot & \\
 & & & & & & & & & & & \bar{\bar{\mathbf{V}}} & \bar{\bar{\mathbf{Z}}} & \bar{\bar{\mathbf{B}}} & \bar{\bar{\mathbf{A}}} & \bar{\bar{\mathbf{C}}} \\
 & & & & & & & & & & & & \bar{\bar{\mathbf{V}}}_I & \bar{\bar{\mathbf{Z}}}_I & \bar{\bar{\mathbf{B}}}_I & \bar{\bar{\mathbf{A}}}_I
\end{bmatrix}
\times
\begin{bmatrix} \bar{\delta}_1 \\ \bar{\delta}_2 \\ \cdot \\ \cdot \\ \cdot \\ \bar{\delta}_6 \\ \cdot \\ \cdot \\ \cdot \\ \cdot \\ \cdot \\ \cdot \\ \cdot \\ \bar{\delta}_i \\ \cdot \\ \bar{\delta} \\ \bar{\delta}_I \end{bmatrix}
=
\begin{bmatrix} -\bar{\mathbf{R}}_1 \\ -\bar{\mathbf{R}}_2 \\ \cdot \\ \cdot \\ \cdot \\ -\bar{\mathbf{R}}_6 \\ \cdot \\ \cdot \\ \cdot \\ \cdot \\ \cdot \\ \cdot \\ \cdot \\ -\bar{\mathbf{R}}_i \\ \cdot \\ -\bar{\mathbf{R}} \\ -\bar{\mathbf{R}}_I \end{bmatrix}
$$

The offset for the matrix above corresponds to the inlet grid in Figure D.11. The global equation rows and global column vectors on the right-hand side are not shown but have the same form as D.2. The shifting affects only the first part of the matrix, up to the leading edge of the main blade, where the offset stops (at $i = 7$ in the figure). The remainder of the grid, including the exit, uses regular unshifted periodic conditions.

The offset-periodic pressure and geometry terms define two new matrix blocks, both extremely sparse. The three pressure terms have been shifted left by i_{off} into the lower triangle and form the $\bar{\bar{\mathbf{V}}}'_i$ through $\bar{\bar{\mathbf{C}}}'_i$ blocks, each corresponding to terms shifted out of one of the principal blocks near the diagonal. The geometric periodicity term has been shifted right by i_{off} into the upper triangle. This shifting configuration entails the least 'fill-in' during the elimination process.

D.4.1 Offset Block Structure

The blocks $\bar{\bar{\mathbf{V}}}'_i$ through $\bar{\bar{\mathbf{C}}}'_i$ in the matrix lower triangle contain the shifted pressure periodicity terms. These are shown on the left side of Figure D.12. The blocks $\bar{\bar{\mathbf{V}}}_i$ through $\bar{\bar{\mathbf{C}}}_i$ near the diagonal are modified as well – all the terms corresponding to those in the offset blocks are cleared. The $\bar{\bar{\mathbf{C}}}'_i$ block differs slightly because it contains no $\delta\rho$ terms. The block $\bar{\bar{\mathbf{U}}}'_i$, consisting of a single non-zero term for the geometry

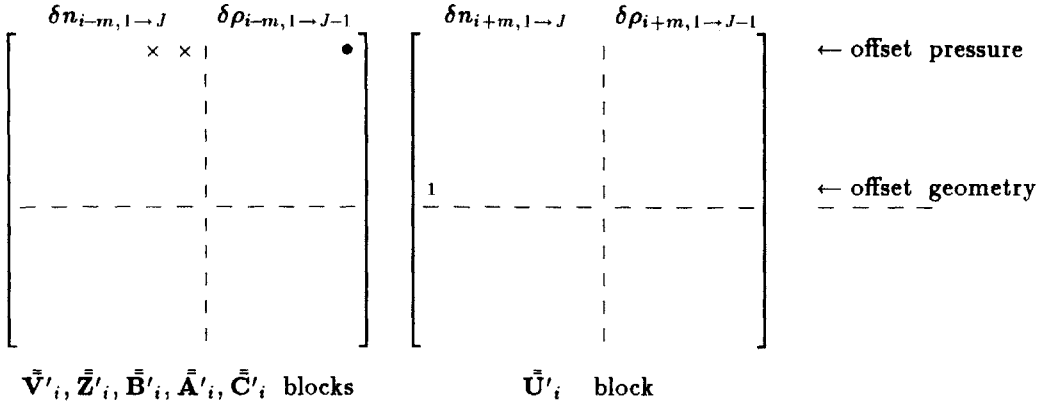

Figure D.12: Structure of lower and upper triangle blocks for offset-periodic matrix

matching, is shifted into the upper triangle of the matrix, This block is shown in the right side of Figure D.12. The corresponding term from $\bar{\bar{\mathbf{A}}}_i$ is cleared.

D.4.2 Offset Matrix Solution

The offset-periodic matrix is solved using a modification of the block Gauss-elimination solver from ISES [15]. The elimination process itself is straight-forward, but becomes quite complex, particularly in the offset region, due to the need for data structures to minimize storage of the upper triangular terms. The lower triangle blocks $\bar{\bar{\mathbf{V}}}' \rightarrow \bar{\bar{\mathbf{C}}}'$ and $\bar{\bar{\mathbf{V}}} \rightarrow \bar{\bar{\mathbf{B}}}$ are eliminated using the *factored* upper triangle blocks $\bar{\bar{\mathbf{C}}}''$ and $\bar{\bar{\mathbf{U}}}''$. The factored entries for $\bar{\bar{\mathbf{U}}}''$ are stored in an array of column vectors whose columns fill during the elimination, from the original block $\bar{\bar{\mathbf{U}}}'_i$ down to the $\bar{\bar{\mathbf{C}}}_{i+i_{off}}$ block. The general form of

the factored matrix with upper triangle offset columns is

$$\begin{bmatrix}
\bar{\bar{\mathbf{I}}} & \bar{\bar{\mathbf{C}}}_1'' & & & \bar{\bar{\mathbf{U}}}_1'' & & & & & \\
& \bar{\bar{\mathbf{I}}} & \bar{\bar{\mathbf{C}}}_2'' & & \Downarrow & \bar{\bar{\mathbf{U}}}_2'' & & & & \\
& & \ddots & \ddots & \Downarrow & \Downarrow & \ddots & & & \\
& & & \bar{\bar{\mathbf{I}}} & \bar{\bar{\mathbf{C}}}_7'' & \Downarrow & \ddots & \bar{\bar{\mathbf{U}}}_6'' & & \\
& & & & \ddots & \ddots & \ddots & \Downarrow & & \\
& & & & & \bar{\bar{\mathbf{I}}} & \bar{\bar{\mathbf{C}}}_i'' & \Downarrow & & \\
& & & & & & \ddots & \ddots & & \\
& & & & & & & \bar{\bar{\mathbf{I}}} & \bar{\bar{\mathbf{C}}}'' & \\
& & & & & & & & \bar{\bar{\mathbf{I}}} & \bar{\bar{\mathbf{C}}}'' \\
& & & & & & & & & \bar{\bar{\mathbf{I}}}
\end{bmatrix} \times \begin{bmatrix} \bar{\boldsymbol{\delta}}_1 \\ \bar{\boldsymbol{\delta}}_2 \\ \vdots \\ \bar{\boldsymbol{\delta}}_7 \\ \vdots \\ \bar{\boldsymbol{\delta}}_i \\ \vdots \\ \bar{\boldsymbol{\delta}} \\ \bar{\boldsymbol{\delta}} \\ \bar{\boldsymbol{\delta}}_l \end{bmatrix} = \begin{bmatrix} \tilde{\boldsymbol{\delta}}_1 \\ \tilde{\boldsymbol{\delta}}_2 \\ \vdots \\ \tilde{\boldsymbol{\delta}}_7 \\ \vdots \\ \tilde{\boldsymbol{\delta}}_i \\ \vdots \\ \tilde{\boldsymbol{\delta}} \\ \tilde{\boldsymbol{\delta}} \\ \tilde{\boldsymbol{\delta}}_l \end{bmatrix} - \begin{bmatrix} \tilde{\mathbf{h}}_1 \\ \tilde{\mathbf{h}}_2 \\ \vdots \\ \tilde{\mathbf{h}}_7 \\ \vdots \\ \tilde{\mathbf{h}}_i \\ \vdots \\ \tilde{\mathbf{h}} \\ \tilde{\mathbf{h}} \\ \tilde{\mathbf{h}}_l \end{bmatrix} \bar{\boldsymbol{\Delta}}_g \quad \text{(D.9)}$$

The extra cost associated with the offset solver depends on the total number of offset blocks, each of which adds a portion of the computational cost of an extra right-hand side (~3% per RHS). The fraction of the extra cost compared to a RHS is dependent on the relative size of the offset region. In practice, an offset solution is 2-3 times slower than a comparably sized standard solution.

Bibliography

[1] M. B. Giles and M. Drela. Two-dimensional transonic aerodynamic design method. *AIAA Journal*, 25(9), Sep 1987.

[2] R. L. Holtman, G. D. Huffman, and R. B. McClure. Test of a supersonic compressor cascade, (vol. i). ARL Report 72-0170, Air Force Wright Aeronautical Laboratories, December 1972.

[3] R. L. Holtman, R. B. McClure, and G. T. Sinnet. Test of a supersonic compressor cascade with with splitter vanes. ARL Report 73-0142, Air Force Wright Aeronautical Laboratories, December 1973.

[4] A. J. Wennerstrom and G. R. Frost. Design of a rotor incorporating splitter vanes for a high pressure ratio supersonic axial compressor stage. ARL Report 74-0110, Air Force Wright Aeronautical Laboratories, August 1974.

[5] R. E. Riffel and S. Fleeter. The effect of splitter vane circumferential location on the aerodynamic performance of a supersonic compressor cascade. AFAPL Technical Report TR-77-20, Air Force Wright Aeronautical Laboratories, April 1977.

[6] P. R. Dodge. Transonic two-dimensional flow analysis of compressor cascade with splitter vanes. AFAPL Technical Report TR-75-110, Air Force Wright Aeronautical Laboratories, 1975.

[7] P. R. Dodge and L. S. Lieber. Transonic 3-D flow analysis of compressor cascade with splitter vanes. AFAPL Technical Report TR-78-23, Air Force Wright Aeronautical Laboratories, May 1978.

[8] M. Drela. *Two-Dimensional Transonic Aerodynamic Design and Analysis Using the Euler Equations.* PhD thesis, MIT, Dec 1985. Also, MIT Gas Turbine & Plasma Dynamics Laboratory Report No. 187, Feb 1986.

[9] R. C. Lock and B. R. Williams. Viscous-inviscid interactions in external aerodynamics. *Progress in Aerospace Sciences*, 24:51–171, 1987.

[10] J. E. Green, D. J. Weeks, and J. W. F. Brooman. Prediction of turbulent boundary layers and wakes in compressible flow by a lag-entrainment method. R & M Report 3791, Aeronautical Research Council, HMSO, London, 1977.

[11] H. W. Liepmann and A. Roshko. *Elements of Gasdynamics.* Wiley, New York, 1957.

[12] M. Drela and M. B. Giles. Viscous-inviscid analysis of transonic and low Reynolds number airfoils. *AIAA Journal*, 25(10), Oct 1987.

[13] M. Drela. An integral boundary layer formulation for blunt trailing edges. AIAA-89-2200, Aug 1989.

[14] R.A. Shapiro. *An Adaptive Finite Element Solution Algorithm for the Euler Equations.* PhD thesis, MIT, April 1988. Also, MIT Computational Fluid Dynamics Laboratory Report CFDL-TR-88-7, May 1988.

[15] M.B. Giles. *Newton Solution of Steady Two-Dimensional Transonic Flow.* PhD thesis, MIT, Jun 1985. Also, MIT Gas Turbine & Plasma Dynamics Laboratory Report No. 186, Oct 1985.

[16] D. E. Hobbs, J. H. Wagner, J. F. Dannenhoffer, and R. P. Dring. Supercritical Airfoil Technology Program, Wake Experiments and Modeling for Fore and Aft-Loaded Compressor Cascades. Final Report FR-13514, Pratt & Whitney Aircraft Group, UTC, September 1980.

[17] H. A. Schreiber and H. Starken. Experimental investigation of a transonic compressor rotor blade section. *Journal of Engineering for Gas Turbines and Power, Transactions of the ASME*, 106(83-GT-209):288–294, April 1984.

[18] H. Starken and H. A. Schreiber. Test case E/CA-4 low supersonic compressor cascade MCA. In *Test Cases for Computation of Internal Flows in Aero Engine Components*, number AR-275 in AGARD Report, pages 81–94. AGARD Propulsion and Energetics Panel, July 1990.

[19] M.G. Turner. *Design and Analysis of Internal Flowfields Using a Two Stream Function Formulation.* PhD thesis, MIT, January 1990. Also, MIT Gas Turbine & Plasma Dynamics Laboratory Report No. 201, January 1990.

[20] D. L. Whitfield. Analytical description of the complete turbulent boundary layer velocity profile. AIAA-78-1158, 1978.